Characterization of Novel Fabry Pérot Filter Arrays for Nanospectrometers in Medical Applications

Hong Hanh Mai

Dissertation

Eingereicht zur Erlangung des akademischen Grades eines
Doktor der Ingenieurwissenschaften (Dr.-Ing.)
im Fachbereich Elektrotechnik/Informatik
der Universität Kassel

Gutachter: Prof. Dr. rer.nat. H. Hillmer
Prof. Dr. -Ing. J. Börcsök
Prof. Dr. -Ing. A. Bangert
Prof. Dr. -Ing. P. Lehmann

Kassel, July 2012

To my parents

Erklärung

Hiermit versichere ich, dass ich die vorliegende Arbeit selbstständig und ohne unerlaubte Hilfe angefertigt und andere als die in der Dissertationen gegebenen Hilfsmittel nicht benutzt habe. Alle Stellen, die wörtlich oder sinngemäß aus veröffentlichten oder unveröffentlichten Schriften entnommen sind, habe ich als solche kenntlich gemacht. Kein Teil dieser Arbeit ist in einem anderen Promotions- oder Habilitationsverfahren verwendet worden.

Kassel, July 2012

Tag der mündlichen Prüfung: 23.10.2012

Acknowledgements

It is impossible to mention all the people who have helped me during the last three years at INA and I apologize in advance for not being able to acknowledge everyone.

Fristly, I would like to thank my supervisor, Prof. Dr. Hartmut Hillmer for offering me a great opportunity to work at INA. His support, guidance and encouragement from the beginning to the f nal level, motivated and enabled me to develop an understanding of the subject. It is a blessing to work for a man with vision and I was very fortunate in this regard. I also thank Prof. Dr. J. Börcsök for co-supervising my thesis and the other examiners Prof. Dr.-Ing. Axel Bangert, Prof. Dr.-Ing. Peter Lehmann.

I would like to thank Goettlieb Daimler und Carl Benz foundation for the financial support in my first two years.

I am also grateful to Dr. W. Köcher, Mr. C.Sandhagen from OPN and all the members of Nanospectrometer groups. Everybody deserves a lot of credit for your outstanding works in fabricating static and tunable Fabry Pérot filter array based Nanospectrometers. Without your work, I cannot finish my thesis.

I would like to acknowledge fruitful discussions with Dr. Thomas Kusserow, Dr. Volker Viereck, Mr. Carsten Woidt. Thank you very much for spending a lot of time to review, critique this work and give me valuable advices.

I would also like to thank Mr. Dietmar Gutermuth, Mr. Jens Krumpholz for your outstanding technical assistance and for designing and machining numerous parts for my experimental setups.

My grateful acknowledgments go out to all the members of INA. From the moment I started studying as a PhD student at INA, Uni Kassel, I always felt the support of the institute in all my endeavors. Institute’s assistance, f nancial and otherwise, gave me the welcome security and peace of mind to concentrate on the research. I would also like to thank all my friends at INA who had to put up with me all these years: Ricardo Zamora, Waleed Al-Esayi, Mohamed Abdel-Awwad, Basoene Briggs, Onny Setyawati, Basim Khudhair, Ferdinand Messow, Jyoti Shrestha, Markus Engenhorst, Wei Chung Ang, Xiaolin Wang, Alla Albrecht…. I really appreciate your friendship.

My thankfulness also goes to all the wonderful people who made me feel at home in this country: especially Mrs. Nhu Thao Dang Pham. Thank you for your love and cooking.

Last but not the least I would like to express my deep and sincere gratitude to my parents and my brother for their unconditional support, their endless encouragement and most importantly their love in all the past years.

TABLE OF CONTENTS

1 INTRODUCTION 1

2 THEORETICAL BASICS 5

2.1 Foundations of the Fabry Pérot filter arrays 5
2.1.1 The Fabry Pérot filter and its characteristic optical parameters 5
2.1.1.1 Distributed Bragg Reflectors 5
2.1.1.2 Fabry Pérot filters 9
2.1.1.3 Characteristic optical parameters of Fabry Pérot filters 11
2.1.2 State of the Art: Fabry Pérot Filter based Nanospectrometers 12
2.1.3 3D NanoImprint technology 13
2.1.4 Static Fabry Pérot filter arrays 15
2.1.5 Basics of micromachined tunable FP Filters 17
2.1.5.1 Ideal static tuning function 17
2.1.5.2 Tunable Fabry Pérot filter arrays 20
2.1.5.3 A simple elastic capacitor model of a micromachined tunable FP filter 22
DC actuation.. 26
AC actuation.. 27

2.2 Optical characterization methodology 29
2.2.1 llumination systems for optical spectroscopy 30
2.2.1.1 Halogen lamp as illumination system 30
2.2.1.2 Supercontinuum white light laser as illumination system 31
2.2.2 Collimation and magnification systems for optical spectroscopy 34
2.2.2.1 Objective lenses for optical spectroscopy 35
2.2.2.2 Optical microscopes and condensers for optical spectroscopy 38
2.2.3 Methodology of spectral analysis and recording 40
2.2.3.1 Grating monochromator for spectral dispersion 41
2.2.3.2 Grating spectrometer for spectral dispersion 42
2.2.3.3 Optical spectrum analyzers for spectral dispersion based on grating monochromators 43
2.2.4 Basics of white light interferometry to visualize micromachined displacements 45

3 PREVIOUS OPTICAL SETUP DESIGNS TO CHARACTERIZE OPTICAL PROPERTIES OF FABRY PÉROT FILTER ARRAYS 48

3.1 Lamdba 900 spectrophotometer 48

3.2 Optical bench setup 50

3.3 The fiber based setup 51

3.4 Compact microscope spectrometer setup 53
3.4.1 Construction details of the compact microscope spectrometer setup 53
3.4.1.1 The illumination system of the setup 54
3.4.1.2 The collimation and magnification system and the sample stage of the setup 54
3.4.1.3 The data recording and analysis system of the setup 56
3.4.2 Working principle of the compact microscope spectrometer setup 58
3.4.2.1 Working principle of the setup in reflection measurement 58
3.4.2.2 Working principle of the setup in transmission measurement 59
3.4.3 General spectral features in calibrating setups and correcting spectra 61
3.4.4 The calibration procedure of the setup 62

4 GEOMETRIC AND COMPOSITIONAL DETAILS OF THE SAMPLES STUDIED 65

4.1 Geometric and compositional details of unstructured Fabry Pérot filters 65

4.2 Geometric and compositional details of static Fabry Pérot filters 65

4.3 Geometric and compositional details of tunable Fabry Pérot filters 66

5 EXPERIMENTAL RESULTS USING THE COMPACT MICROSCOPE SPECTROMETER SETUP FOR CHARACTERIZATION OF FABRY PÉROT FILTER ARRAYS 69

5.1 Optical characterization of laterally unstructured Fabry Pérot filters 69

5.2 Optical characterization of static Fabry Pérot filter arrays 72

5.3 Optical characterization of micromachined tunable Fabry Pérot filter arrays 74

5.4 Comparison of micromachined optical tuning of Fabry Pérot filter arrays under DC and AC actuation 79
5.4.1 DC Actuation 80
5.4.2 AC actuation 82
5.4.3 Model for the dynamics of trapping and reemission of charges in dielectrics 90

6 DESIGN, IMPLEMENTATION AND APPLICATIONS OF THE FREE BEAM BROAD BAND CONFOCAL SETUP 97

6.1 Construction details of the free beam broad band confocal setup 98

6.1.1 The illumination system of the setup 98

6.1.2 The collimation and magnification system of the setup 98

6.1.3 The data recording and analysis system of the setup 100

6.1.4 The sample stage and the imaging system of the setup 101

6.2 Working principle of the free beam broad band confocal setup 104

6.2.1 Working principle of the setup in transmission and reflection measurement 104

6.2.2 The calibration and alignment procedure of the setup 106

6.2.1 Optimum location of the filter sample relative to the optical main path of the setup 108

6.3 Experimental results using the free beam broad band confocal setup 109

6.3.1 Optical characterization of unstructured Fabry Pérot filters 109

6.3.2 Optical characterization of static Fabry Pérot filter arrays 110

6.3.3 Optical characterization of micromachined tunable Fabry Pérot filter arrays 112

7 CONCLUSION 114

BIBLIOGRAPHY I

LIST OF TABLES VIII

LIST OF FIGURES IX

TABLE OF ABBREVIATIONS AND CHEMICAL FORMULA XIV

TABLE OF USED SYMBOLS AND PHYSICAL PARAMETERS XVI

LIST OF PUBLICATIONS XVIII

1 Introduction

Throughout the last years, the interest in optical sensing systems has rapidly increased due to their great potential in chemical, medical, industrial process controls, automatic identification and smart personal environments [1-3]. Regarding the medical field, some smart sensor arrays are able to diagnose diseases and detect characteristic biomarkers in a transcutaneous, non-invasive and user-friendly way [4, 5] based on the complex interaction of light propagation and absorption by human skin tissues [6-8]. However, to fulfill the rapidly increasing requirements in applications, the optical sensors need to be significantly miniaturized, cheaper, allowing redundancy, and short measurement time. Furthermore, they need to have the potential to be integrated into networked sensing systems, and should enable self-learning features as well as to reveal invisibility in smart personal environments.

Concerning about the light interaction with human skin, spectral distribution which is measured in terms of reflection and transmission is of most importance for medical applications and is relatively complicated to measure. Therefore, an appropriate spectrometer is one of the key factors to take the advantage of this phenomenon. However, producing miniaturized and low-cost spectrometers of high precision are still a big challenge due to the strongly decreasing optical resolution when just shrinking the size of the traditional monochromator based spectrometers [9].

To combine a small size and a high resolution Correia et al. [10] and Wang et al. [11] established a new approach: combining a Fabry Pérot (FP) filter array with a detector array which can act as a microspectrometer. Each detector corresponds to one individual filter to detect a very narrow band of wavelengths (filter lines) transmitted through the filter. An array of FP filters is used in which each filter selects a different spectral filter line. The spectral position of each band of wavelength is defined by each individual cavity height of the filter. These groups presented the methods to fabricate 16 and 128 FP filters, respectively, based on 16 and 128 different cavity heights. The arrays were developed with filter sizes which are limited only by the dimensions of the individual detectors in the array [10-14]. In both works, however, these structures were fabricated by multiple processing steps to obtain the required various cavity heights [10-16]. These processes are obviously not cost efficient for industrial fabrication if a large number of different wavelength is envisaged.

To reduce the cost, while maintaining the outstanding advantages of the FP filter structure, a novel methodology of fabricating the miniaturized FP filters using NanoImprint

technology is developed and introduced at INA [17-24]. Compared to the state-of-the-art technology [10-14], the multiple cavity fabrication steps are replaced by one single step, using high vertical resolution 3D NanoImprint technology. Since NanoImprint technology is involved, the researchers at INA introduced it as *nanospectrometer* [17-24].

NanoImprint technology can be used for patterning deformable materials e.g. polymers. Most of the scientific community considers that the modern NanoImprint technology was invented in 1995 by Stephen Y. Chou and his group. Soon after this invention, many variations and implementations for NanoImprint technology were developed and widely spread to applications in electronics, optics, photonics and biology [25-29]. However, nearly all of the researches in NanoImprint technology concentrate mainly on the improvement of the lateral resolution, thus, reporting on 2D NanoImprint [25, 28].

In order to satisfy the requirement of precisely performing multiple arbitrary cavity heights of the nanospectrometer, the development of 3D NanoImprint technology with high vertical resolution is demanded. By applying 3D NanoImprint technology during the fabrication process of FP f lter arrays, the implemented nanospectrometers become promising candidates to satisfy the above mentioned challenging requirements in optical sensing systems. They are very small, low cost, light weight and of high spectral performance. Besides, they have a great potential to be integrated into existing mobile devices as well as to networked sensing systems, thus, enabling smart personal environments.

Due to the small lateral dimensions of a single FP filter, the filter arrays can contain thousands of individual FP filters. The functionality of the FP f lters and the arrays has to be verif ed. Therefore, a high quality characterization of the optical properties and tuning behaviors is demanded to provide an important feedback for the fabrication processes and to optimize the f nal f lter quality.

The goal of this thesis is to investigate the optical properties and tuning behaviors of FP filter arrays for nanospectrometers by installing, utilizing and designing characterization setups with high spectral quality. Based on the specific spectral and geometric properties of the FP filters, most of the required factors of the characterization setups are defined. For instance, based on the broad spectral range of applications of the fabricated filter arrays, the characterization is focused on the visible and near infrared (NIR) region. Due to the micro structure of the filter membranes, the requirement of precisely detecting signals from such small dimensions is also addressed. Moreover, a minimum inspection time for each f lter, a fast “step and repeat”modus are further desirable factors which need to be treated with some caution in the setups.

In order to obtain the above mentioned goals, two characterization setups for spectral transmission and reflection measurements in the visible and NIR range were installed, designed and implemented. The setups are *the compact microscope spectrometer setup* and *the free beam broad band confocal setup*. Both of them can provide adequate spectral and spatial accuracy, high measurement speed and the ability of measuring microstructure dimensions.

This thesis contains of seven chapters:

Chapter 2 presents the foundation that helps the reader to understand, to follow the argumentation and the experimental results obtained from this thesis. It begins with an introduction to FP filter and its important characteristic optical parameters. It familiarizes the readers with the idea of FP filter based Nanospectrometers which are fabricated by 3D NanoImprint technology. A basis of static FP filter arrays and micromachined tunable FP filter arrays as well as a theory of tuning behaviors of tunable FP filters when applying an external voltage DC or AC are also presented in this chapter. Afterwards, the chapter provides the knowledge of optical characterization methodology for the FP filter arrays. Principles of some essential components and devices which are commonly implemented in an optical characterization setup are also described. Finally, it ends with the fundamental basis of white light interferometry to visualize micromachined displacements.

Chapter 3 introduces three existing old characterization setups (the Lambda 900 spectrophotometers, the optical bench setup and the fiber based setup) which are commonly utilized to investigate optical and tuning behaviors of the FP filter arrays. It also addresses their advantages and disadvantages which are needed to be overcome by new characterization setups. Afterwards, the chapter describes the construction details and the working principle of the compact microscope spectrometer setup. A precise alignment and calibration of the setup which are the critical issues to obtain the reliable results is also presented in this chapter.

Chapter 4 presents the geometric and compositional details of the samples including static and tunable FP filters which are studied in this work.

Chapter 5 describes the experimental results using the compact microscope spectrometer setup while characterizing the optical properties and tuning behaviors of static and tunable FP filter arrays. The accuracy of the setup is evaluated by comparing the spectra obtained from the setup with that of the existing old setups mentioned in chapter 3. The tuning behaviors of the tunable FP filters are investigated by the implementation of two kinds of experimental conditions concerning constant or temporally oscillating bias voltages: DC or AC actuation.

Chapter 6 presents the design, implementation and application of the free beam broad band confocal setup which can operate in both the visible and NIR range. It describes the design of the optical measurement system as well as the mechanical construction that serves as a frame structure for the setup and defines the importance of precise calibration and alignment of the implemented optical components. Some experimental results obtained from the setup are also presented in this chapter.

Chapter 7 concludes the results of this thesis and includes suggestions for the future optimization of the setups.

2 Theoretical basics

The goal of this work is to characterize the optical properties and tuning behaviors of static and tunable FP filter array for Nanospectrometers by using and implementing measurement setups with high spatial spectral accuracy. This chapter provides the fundamentals for the readers to understand the basis concept of this work. Firstly, a brief introduction to the basic knowledge of FP filter and its important characteristic optical parameters such as Full Width at Half Maximum ($FWHM$), Resolving power ($\mathfrak{R}$), Free Spectral Range (FSR) and Finess ($\mathcal{F}$) is given. A basis of static FP filter arrays and micromachined tunable FP filter arrays fabricated by 3D NanoImprint technology as well as a theory of tuning behaviors of tunable FP filters are also introduced in this chapter. Afterwards the basic knowledge of optical characterization methodologies for the FP filter arrays and the working principles of the crucial elements and devices which are commonly used to investigate optical properties and tuning behaviors are finally presented.

2.1 Foundations of the Fabry Pérot filter arrays

2.1.1 The Fabry Pérot filter and its characteristic optical parameters

A FP filter is an interferometer type and a special type of a thin film optical filter. Based on the phenomenon of multi beam interferences it can transmit a certain band of wavelength and reflect wavelengths outside of that band. A standard FP filter consists of two parallel, highly reflective mirrors and a cavity formed between them. In this work, Distributed Bragg Reflectors (DBRs) are implemented as the highly reflective mirrors which are one of the key components of a FP filter. The discussion in this section will be started with DBRs then the theory of FP filter. Its characteristic optical parameters will be introduced in the following subsections.

2.1.1.1 Distributed Bragg Reflectors

DBRs are composed by a stack of layers with alternately high and low refractive index. In the design of FP filters, the DBRs are commonly used as high quality reflective mirrors due to their high reflectance and low absorption compared to metal mirrors. A well designed DBR can provide extremely high reflectance over a wide range in the optical spectrum, which is later called the stopband.

In order to understand the working mechanism of the DBRs, the propagation of light within periodic multiple layers of the DBRs is taken into account. If an incident light beam of a discrete wavelength λ is illuminated on to alternating high and low refractive index layers of a DBR; it is partly reflected and partly transmitted at each layer interface. Reflected light beams then recombine and interfere with each other as demonstrated in Fig. 2.1. According to wave optics, constructive interference occurs if the relative phase shift among the beams is:

$$\Delta\varphi = m \cdot 2\pi \qquad \textbf{2.1}$$

Destructive interference, in contrast, occurs as the relative phase shift is:

$$\Delta\varphi = (2m + 1) \cdot \pi \qquad \textbf{2.2}$$

where m is an integer. The same phenomenon is applied for transmitted light beams.

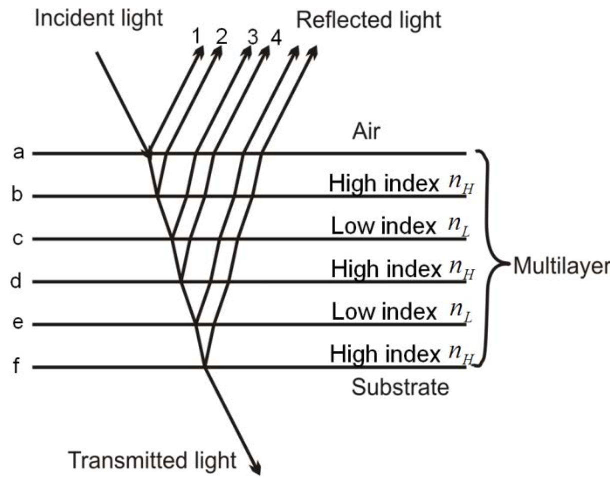

Fig. 2.1. Reflection and transmission of incident light on many alternating high and low refractive index layers.

In a DBR the optical height of each thin film layer is chosen to be a $\lambda/4$ layer. Furthermore, an odd number of $\lambda/4$ layers is chosen in total. Passing one of these $\lambda/4$ layers the beam experiences a phase shift of $\pi/2$. If light is travelling in a medium of low refractive index and it is reflected at a boundary to a higher refractive index layer it experiences a phase shift of π in case of vertical incidence. Considering the selection of beams 1, 2, 3, 4 etc. depicted in Fig. 2.1 and the two different phase shift types mentioned above we are able to obtain constructive interference in reflection and are able to fulfill Eq. 2.1. The total phases of the beams 1, 2, 3, 4 etc. depicted in Fig. 2.1 are indicated as δ_1, δ_2, δ_3, δ_4 etc. The phases of all reflected light beams 1, 2, 3, 4 etc. after they passed the boundary **a** are additionally written in the following formula:

$$\begin{aligned}
\delta_1 &= \delta_0 + \pi \\
\delta_2 &= \delta_0 + \pi/2 + \pi/2 = \delta_0 + \pi \\
\delta_3 &= \delta_0 + \pi + \pi + \pi = \delta_0 + 3\pi \\
\delta_4 &= \delta_0 + 3\pi/2 + 3\pi/2 = \delta_0 + 3\pi
\end{aligned} \quad \textbf{2.3}$$

Note, that a phase shift of π occurs at the boundaries **a, c, e**... where light reflects at a medium of a higher refractive index medium, as mentioned already above.

Equation 2.3 demonstrates that all the reflected beams are in phase with the incident beam, and the relative phase shift among all reflected light $\Delta\varphi$ always are a multiple of 2π. Thus, the condition in Eq. 2.1 is fulfilled, the constructively interference always occurs. That means the DBR can work as an ideal reflector.

In fact, the optical thickness of a quarter wavelength is commonly described as:

$$n_i d_i = \frac{\lambda}{4} \quad \textbf{2.4}$$

where n_i represent the refractive index of the corresponding material, and d_i represent the physical height of the layer.

The reflectivity of a DBR is given as [30, 31]:

$$R = \left(\frac{1 - \left(\frac{n_H}{n_L}\right)^{2p} \left(\frac{n_t^2}{n_s}\right)}{1 + \left(\frac{n_H}{n_L}\right)^{2p} \left(\frac{n_t^2}{n_s}\right)} \right)^2 \quad \textbf{2.5}$$

where p is the number of thin layers, n_H is the refractive index of the high index layer, n_L is the refractive index of the low index layer, n_t and n_s are the refractive indices of the surrounding medium and the substrate, respectively. The expression shows that the reflectivity is determined by the contrast of refractive indices and the number of thin film layers. Theoretical calculations show that reflectivity of a DBR can be increased by increasing the refractive index contrast of the two materials, and the number of thin film layers [32, 33].

The most interesting properties of the DBRs are their reflection and transmission spectra. In this work, a stack of layers with alternately high and low refractive index of the DBRs can be considered as a 1D periodic structure, and their reflection and transmission spectra can be calculated by using the transfer matrix method (TMM). The main idea of this method is to describe the sequence of different optical layers equivalent to a chain of two-ports in electrical engineering. Therefore each thin film layer of the DBR structure is characterized by a 2 x 2 matrix to describe the ingoing and outgoing electri-

cal and magnetic fields, thus, the electromagnetic waves in each interface. In this way it is possible to describe the propagation of light through a layered medium of p individual layers by a matrix multiplication of p individual 2 x 2 matrices. The advantage of using matrix representation of the electromagnetic field of light is that now for a sequence of layers only matrices for each layer type has to be defined including all the specific physical aspects. As a result, reflectance and transmittance of the light through multi thin film layers are derived directly from the components of the transfer matrix.

Based on the TMM the reflection spectrum and transmission spectrum of a DBR is calculated and presented in Fig. 2.2 (a) and (b). Here, a spectrum region where the DBR provides extremely high reflectance is called the stopband. In the reflection spectrum Fig. 2.2 (a) the stopband results from the constructive interference of the reflected light waves whereas in the transmission spectrum Fig. 2.2 (b) the stopband is generated by the destructive interference of the transmitted light waves and thus its transmittance is close to zero [34]. In case of dielectrics or semiconductors with very low absorption losses, maximum reflectance can very closely reach 100 % at the design wavelength [33].

Neglecting loss the width of the stopband can be written as [30]:

$$\Delta\lambda_0 = \frac{4\lambda_0}{\pi} sin^{-1}\left(\frac{n_H - n_L}{n_H + n_L}\right) \qquad \textbf{2.6}$$

where λ_0 is the center wavelength of the stopband.

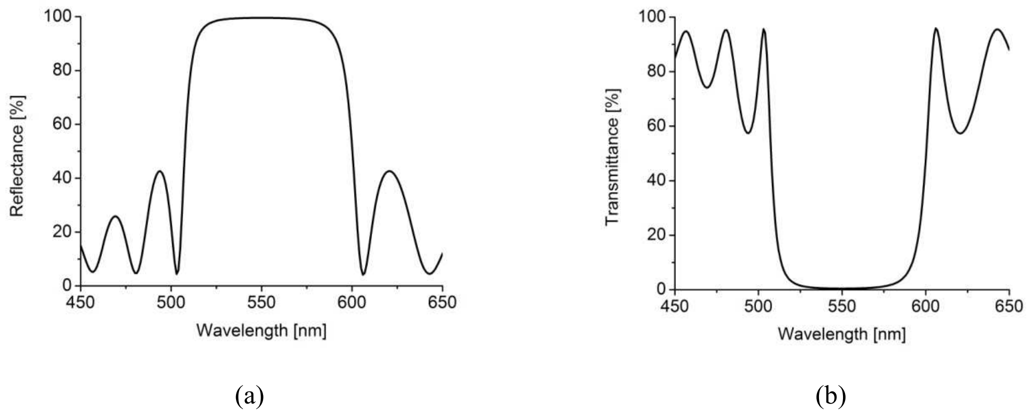

(a) (b)

Fig. 2.2. Reflection spectrum (a) and transmission spectrum (b) of a DBR consisting of 9.5 periods of Si_4N_4 and SiO_2.

As derived from the equation, the width of the stopband grows with increasing of refractive index contrast of two materials. The sharpness of its edges is determined by the number of layers. The higher the number of layers in use is, the sharper the edges can

be. However, increasing the number of layers also leads to the increase of losses in material and in practicable fabrication processes.

2.1.1.2 Fabry Pérot filters

A FP filter consists of two DBRs and a cavity in between as shown in Fig. 2.3 (a). It is also based on the principle of multiple beam interference. If the cavity height of less than a couple of wavelengths, it can be considered as a defect in the periodic structure of a DBR which adds an extra phase shift when light propagates through it. The height of the cavity is discussed later in the following part.

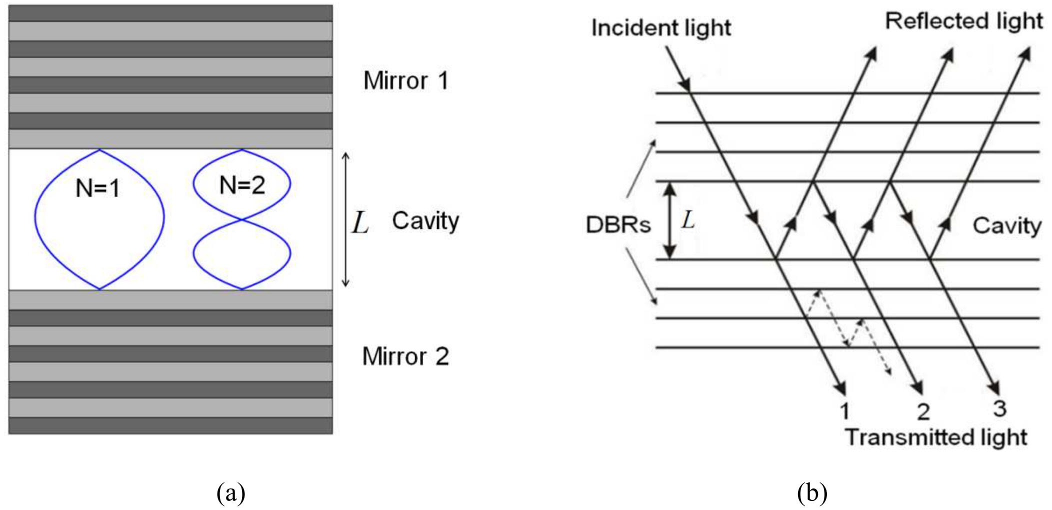

(a) (b)

Fig. 2.3. (a) Schematic view of a FP filter with two cavity modes, and (b) scheme of reflected and transmitted light in a FP filter. The figure is not in scale since the cavity is enlarged at the expense of the $\lambda/4$ layers [32].

Assume that the physical height of the cavity is L, the refractive index of the cavity is n_c. Light propagating through the cavity gains a phase shift of:

$$\delta = \frac{2\pi n_c}{\lambda} L \qquad \textbf{2.7}$$

So the phase difference of transmitted beams (e.g. the beam 1, 2, 3 in Fig. 2.3 (b)) caused by the reflections at the border of the filter cavity is 2δ. Assuming that two identical mirrors are ideal and there is no absorption in the cavity, the transmittance T of the FP filter is denoted in Eq. 2.8 below:

$$T = \frac{1}{1 + F sin^2 \delta} \qquad \textbf{2.8}$$

where R is the reflectance of the two DBRs and F is set as:

$$F = \frac{4R}{(1-R)^2} \quad \textbf{2.9}$$

It is obvious that when $\delta = 0, \pm\pi, \pm 2\pi\ldots$ then $sin^2\delta = 0$, the transmittance T reaches its maximum $T_{Max} = 1$.

This condition can be expressed as:

$$L = \frac{m\lambda}{2n_c} \quad \textbf{2.10}$$

where $m = 1, 2, 3$ ... is the order of interference.

Under this condition, light waves resonating inside the cavity form standing waves.

This phenomenon can be explained when considering the cavity itself as a defect in periodic structure of a DBR. Compared to the normal case of a DBR in which the height of each layer is a quarter of wavelength resulting in a phase shift of $\pi/2$, the implementation of a half wavelength height cavity leads to a phase shift of π. That means the cavity adds an extra phase shift of $\pi/2$ i.e. adding another quarter wavelength layer. Whereas all waves reflected by the interfaces in a DBR superpose in form of an imaginary, exponentially decaying mode the extra phase shift results in constructive interference and the corresponding real cavity mode as seen in Fig. 2.4. This can only be understood when considering the whole filter structure.

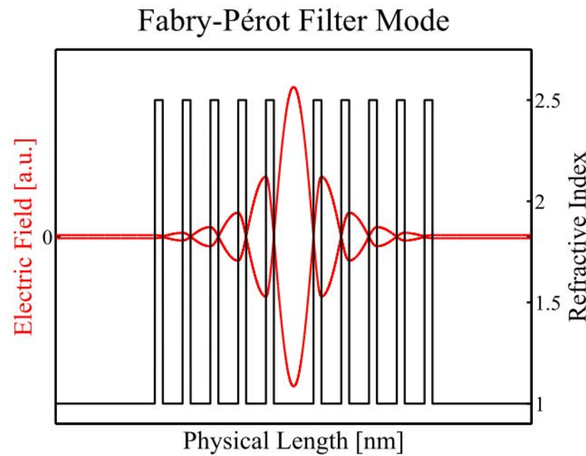

Fig. 2.4. Electric field of the fundamental mode in a FP filter and the related refractive index profile [33].

From Eq. 2.8, the transmittance can be concluded as a function of the reflectivity of the DBRs and the cavity mode. A plot of the transmittance of a FP filter cavity is presented in Fig. 2.5. Here, the transmittances of the filter with different DBR reflectivities are taken into account. The rising peaks defining resonant wavelengths are called transmit-

ted modes, or filter transmission lines. As seen from the figure, the higher the reflectivity of the DBR, the narrower the filter transmission lines become.

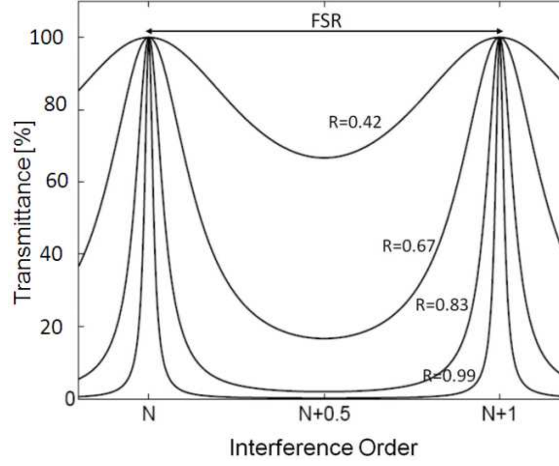

Fig. 2.5. Transmittance of a FP filter with variable DBR mirror reflectivity.

2.1.1.3 Characteristic optical parameters of Fabry Pérot filters

In order to characterize the spectral properties of the FP filter arrays, several important parameters are commonly utilized to evaluate the spectral qualities of the FP filters such as: the Full Width at Half Maximum $(FWHM)$, the Resolving Power $(\Re)$, the Free Spectral Range (FSR) and the Finesse $(\mathcal{F})$.

The first important parameter is the Full Width at Half Maximum ($FWHM$) which is the separation between the points on either side of a maximum where the intensity has fallen to half the maximum value. As seen in Eq. 2.11 the $FWHM$ strongly depends on the reflectivity R of the DBR. With increasing reflectivity, the $FWHM$ is decreased.

$$FWHM = \frac{\lambda^2(1-R)}{2\pi L\sqrt{R}} \qquad \mathbf{2.11}$$

The $FWHM$ of the filter at a given wavelength determines the resolving power which is the second parameter of interest:

$$\Re = \frac{\lambda}{FWHM} \qquad \mathbf{2.12}$$

The third parameter is the distance between adjacent transmitted modes known as the Free Spectral Range (FSR) (as seen in Fig. 2.5)

$$FSR = \frac{\lambda^2}{2L} \qquad \mathbf{2.13}$$

The above relationship implies that the FSR is inversely proportional to the cavity height L and, hence, for a given wavelength it can be increased by reducing the cavity height to the order of magnitude of the wavelength. For a FP filter used in optical spectroscopy, the $FWHM$ is required to be small enough to resolve the spectrum. The FSR, in contrast, has to be large enough to avoid overlap of different filter transmission lines.

The ratio of FSR and $FWHM$ of an individual filter transmission line contributes to the third important parameter: the Finesse $\mathcal{F}$ [30]. As seen from Eq. 2.12 the reflectivity R of the DBR mirrors is the only factor which influences the Finesse value.

$$\mathcal{F} = \frac{FSR}{FWHM} = \frac{\pi\sqrt{R}}{1-R} \qquad \textbf{2.14}$$

2.1.2 State of the Art: Fabry Pérot Filter based Nanospectrometers

Concerning medical applications, optical spectrometers, which are spectroscopic devices, play an important role in measuring the interaction of light with specific molecules or solid state matter involving reflection and transmission phenomena. Since conventional spectrometers are normally expensive, bulky laboratory equipments which often do not fit the requirements of medical applications, it is necessary to develop miniaturized spectrometers. However, producing miniaturized and low-cost spectrometers of high precision is still a big challenge due to the strongly decreasing optical resolution when just shrinking the size of the traditional monochromator based spectrometers [9].

In order to miniaturize spectrometers, great efforts have been made in the last decade, and different approaches of miniaturized microspectrometers have been developed. These microspectrometers are based on optical gratings [35, 36], or interferometric principles such as Mach-Zehnder types or FP types [11, 13, 15]. Among those approaches, recently the implementation of FP filter based microspectrometers has been paid more attention due to the great potential in spectral resolution, intrinsically compact structures, flexibility in spatial distribution and compatibility with commercially available detectors. The idea of this approach is to combine a FP filter arrays and a detector array which can act as a microspectrometer. Here, each detector corresponds to one individual filter to detect a very narrow band of wavelengths (filter lines) transmitted through the filter. An array of FP filters is used in which each filter selects a different spectral filter line. The spectral position of each band of wavelength is defined by each individual cavity height of the filter.

Based on this idea, Correia et al. firstly combined FP filter arrays including 16 cavity heights and photodiodes to detect 16 different wavelengths [10]. Similarly, S.W. Wang et al. implemented a similar structure and extended to 128 different wavelengths in the

range of 722 nm to 880 nm [11]. The above-mentioned FP filter based microspectrometers, however, have common drawbacks: their fabrication requires multiple processing steps to obtain specific nanosize geometric structures. It that case various cavity heights [10-16] differ in vertical direction in the nm scale. For example, to fabricate 2^M different cavity heights, at least M individual steps including lithography and etching (or deposition) processes are required. These processes are obviously extremely cost efficient in industrial fabrication if a large number of different wavelength is envisaged.

To reduce the cost, while maintaining the outstanding advantages of the FP filter structure, a novel methodology of fabricating the miniaturized FP filter based spectrometers using NannoImprint technology is developed and introduced at INA [17-22, 37]. Compared to the state-of-the-art technology [10-14], the multiple cavity fabrication steps are replaced by one single step, using high vertical resolution 3D NanoImprint technology. Since NanoImprint technology is involved, the researchers at INA introduced it as a *nanospectrometer* [17-24]. By applying 3D NanoImprint technology during the fabrication process of FP f lter arrays, the implemented nanospectrometers become promising candidates to satisfy the growing requirements in medical applications and optical sensing systems. They are very small, low cost, of light weight and of high spectral performance. Besides that they have a great potential to be integrated into existing mobile devices as well as to networked sensing systems, thus, enabling smart personal environments.

There are two types of nanospectrometers which have been implemented at INA: the static nanospectrometers and the micromachined tunable nanospectrometers. The static nanospectrometers are the combination of static FP filter arrays and commercially available detectors e.g. CCDs, CMOS-chips or photodiode arrays. Similarly, the tunable nanospectrometers consist of tunable FP filter arrays and commercially available detectors. Details about the static FP filter arrays and tunable FP filter arrays are introduced later in section 2.1.4 and 2.1.5, respectively.

2.1.3 3D NanoImprint technology

NanoImprint technology is a parallel lithography technique, based on the molding of a soft polymer by a template. It is commonly considered to be invented in 1995 by Stephen Y. Chou and his group [38]. Soon after this invention, many variations and implementations for NanoImprint lithography were developed and widely spread for applications in electronics, optics, photonic and biology. In MEMS, one of the most attractive applications of NanoImprint technology is to structure different cavity heights of Fabry Pérot filter arrays. In this case, FP filters with different cavity heights can be per-

formed by only one step NanoImprint. Here, the key issue is the template. Conventional templates, however, typically consist of only two different height levels [25, 28]. Therefore, in order to generate a flexible 3D cavity structure, the conventional NanoImprint templates had to be considerably enhanced towards 3D NanoImprint templates [18, 21, 24].

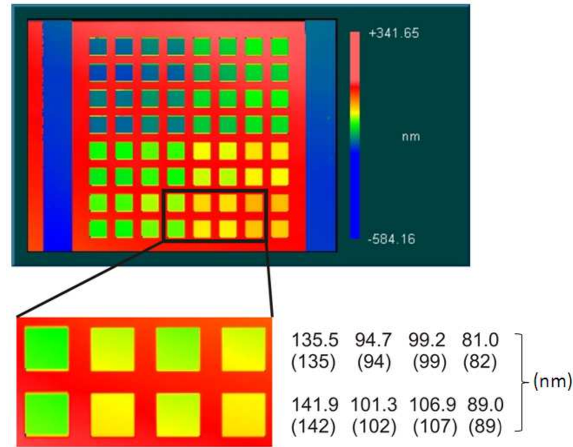

Fig. 2.6. White Light Interferometer (WLI) measurements of a 3D NanoImprint template. A selection of filters is framed and magnified below together with the designed sink depths and the measured depths in brackets [22, 39].

At INA, a novel methodology to fabricate 3D NanoImprint templates with ultra high vertical resolution has been developed [18, 22, 37, 39, 40]. For the proof of concept, the 3D templates contain arrays of “negative” or “positive” mesa structures with up to 64 different sink depths. To meet the requirements of different filter applications, the differences of the sink depth are variable from several nanometers to several hundred nanometers. The fabrication process of 3D templates requires a multiple repetition of photolithography process, reactive ion etching (RIE) and white light interferometry (WLI) measurements (for etching depth control and surface inspection).

Figure 2.6 (top) shows a WLI image of a transparent template that contains an array of sink structures (“negative mesa”) of 64 different depths. Figure 2.6 (bottom) depicts a selection of different filters together with the designed sink depths and the measured sink depths in brackets below. The corresponding dimensions are given in nm. WLI measurements indicate ultra high vertical resolution < 1nm of the 3D patterns on the template.

The fabrication process of structuring different cavity heights in an array using 3D NanoImprint technology is illustrated in Fig. 2.7. First, a soft thin material layer is deposited on the bottom DBR by spincoating or dispensing. A 3D NanoImprint template is pressed into the material to mold the different cavity heights. The material has to be

hardened thermally (Thermal NanoImprint) or by exposing to UV light (UV NanoImprint). After structuring the cavity, the top DBR is deposited to finish the process.

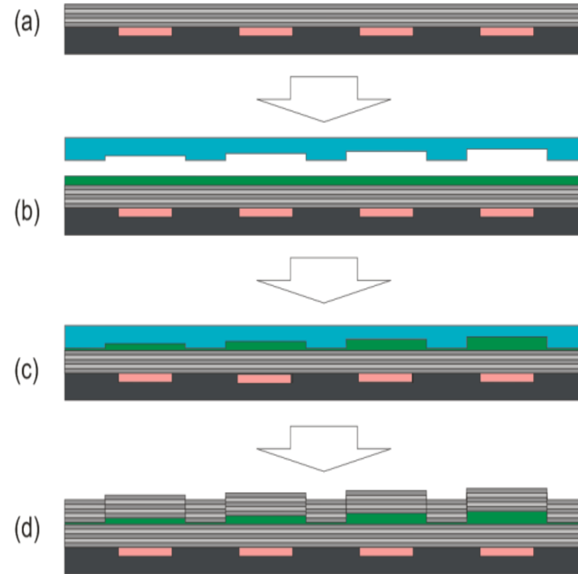

Fig. 2.7. Schematic fabrication process for FP filter / detector arrays: (a) defining bottom DBR on a detector array, (b) 3D NanoImprint template above soft cavity layer, (c) NanoImprint and curing of the polymer, (d) removal of template and deposition of the top DBR [22].

2.1.4 Static Fabry Pérot filter arrays

A static nanospectrometer consists of a static FP filter array on top of a detector array as shown in Fig. 2.8. Each FP filter in an array composes of a bottom DBR, a resonance cavity and a top DBR. The top and bottom DBR are identical and consist of periodically arranged thin dielectric films of materials with alternating high and low refractive indexes. The optical thickness of each dielectric thin film layer included in the DBR is a quarter of the design wavelength. The DBRs are deposited by either by Plasma Enhanced Chemical Vapor Deposition (PECVD) or by Ion Beam Sputter Deposition (IBSD). For spectral detection, the deposition of the DBRs is carried out on a transparent substrate which is later bonded on a detector array such as CCD, CMOS-chip or photodiode array. Each FP filter is assigned to a defined area of the detector array. This area can contain single detector elements or groups of them. Therefore, the lateral geometries of the cavities are designed to match the detector. The lateral and vertical dimensions of the cavities are precisely structured by 3D NanoImprint technology. The cavities only have a few nanometer differences in the vertical direction. The precision of the cavity in the vertical direction is a key factor which influences the accuracy of the spectral position and transmittance of the filter transmission line.

Figure 2.8 (top) depicts a cross section of a part of a static FP filter array with four different cavity heights and the corresponding calculated transmission spectra Fig. 2.8 (bottom). The filter transmission lines within the stopband are characterized by the $FWHM$ and their spectral positions depend on the filter cavity heights. By changing the cavity height, the transmission wavelengths can be precisely chosen.

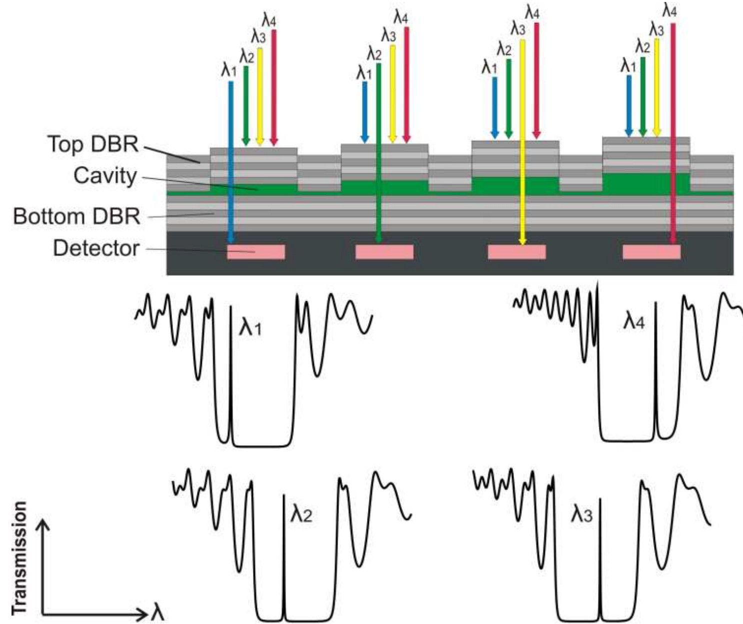

Fig. 2.8. Schematic cross section of an 3D NanoImprinted FP filter array on top of a detector array and corresponding calculated transmission spectra [22, 39].

In principle, static FP filter arrays can include 256, 512, 1024 or more pixels on an area of only a few square millimeters. A specific spectral pixel (filter transmission line, e.g. λ_2 in Fig. 2.8) can occur several times and at different positions in the arrays just as required for redundancy or special requirements.

For a proof of concept a FP filter array with 64 different cavity heights (64 spectrally different pixels) on a substrate was implemented by 3D NanoImprint technology as shown in the WLI image below (Fig. 2.9). The cavity heights range from approx. 80 nm to 240 nm in vertical direction, and cover a lateral area of 100 x 100 µm^2 each. The implemented DBRs are designed for a central wavelength of λ_0 = 575 nm to enable the filter arrays to detect in the visible spectral range. 5.5 periods of $\lambda/4$ TiO_2 and $\lambda/4$ SiO_2 layers are deposited by ion beam sputter deposition to define the DBRs. $\lambda/2$ cavities are formed by UV NanoImprint using mr-UVcur 21 as organic cavity material. After the 3D imprinting and the deposition of the top DBRs, a FP filter array with 64 different cavity heights is created. The individual sinks (hollow structures) characterized by indi-

vidual sink depths are transformed in their surface morphology into mesa (elevated structures) characterized by mesa heights.

The low surface roughness of less than 1 nm and the conservation of important geometrical parameters is maintained during the 3D NanoImprint process [39].

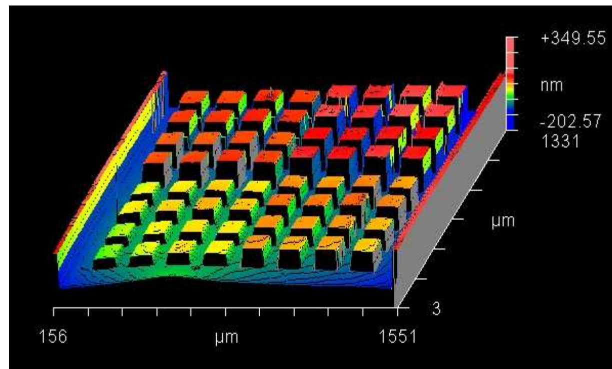

Fig. 2.9. WLI characterization of an imprinted filter array with 64 different heights. The colors in the 3D diagram indicate the different heights. The surface roughness on each individual cavity (mesa) is approx. 0.6 nm rms[1] [22, 39].

2.1.5 Basics of micromachined tunable FP Filters

The basics of micromachined tunable FP filters are introduced in this part. It first recalls a theoretical model calculation of the ideal static tuning function of a micromachined tunable FP filter reported already in a previous research. Afterwards, an introduction of the tunable FP filter arrays for applications in nanospectrometers is given and a simple mechanical oscillator model is described. For the applications of the micromachined tunable FP filter arrays in future, both, high temporal stability and high actuation efficiency are preferable. For this thesis there is a strong motivation to identify an optimum microelectromechanical actuation method. In this chapter the foundations of a time-invariant (DC) and a time-variant actuation (AC) are presented to define the basis for chapter 5, including experimental studies and a detailed study of advantages and disadvantages of different microelectromechanical actuation methods.

2.1.5.1 Ideal static tuning function

Micromachined tunable FP filters have been reported in the past based on different material systems and on several designs. The one which is closest to this work is described in the PhD thesis of A. Tarraf [41]. It consists of a dielectric DBR mirror, an air gap cavity and a dielectric top DBR fixed via three or four suspensions to supporting posts. While the FP filters were actuated by thermal tuning in previous works, in this thesis,

[1] rms: Root mean square

the tuning is implemented by using electrostatic actuation which is as also described in Ref. [24, 42-44]. The membranes of micromachined tunable FP filters whose cavities are air gaps can be varied by a few nm in heights by electrostatic actuation [24, 45]. This reveals a spectral shift of the filter line which is well known as spectral FP filter tuning by micromachined actuation. The mechanical efficiency of displacement strongly depends on the suspension geometry (lengths, width, thickness, bending, and number of suspensions), the material parameters (composition, number of periods) and the membrane geometry. The static mechanical displacement function $h(V)$ describes the displacement of the membranes of FP filters as a function of a varying DC actuation voltage V. That mechanical displacement function is not equal for all tunable filters. On the other hand the impact of a cavity height change h on wavelength is also not at all equal for all tunable filters. This impact depends on the cavity height, the refractive index contrast, the number of periods, loss etc. For details see Ref. [41, 43, 46, 47]. Thus, the optical tuning efficiency depends on three main parameters: the DBR design, the cavity height and the filter's lateral geometry.

In the following only some important aspects are recalled, the optical tuning efficiency $\Delta\lambda/h$ and the optical tuning function $\lambda(L)$. The mechanical displacement behavior of the FP filter affects directly the wavelength tuning. By actively actuating the position of the upper DBR, the optical height of the cavity can be tuned, and thus different filter transmission lines can be selected.

Using a simple one dimensional model capacitor model a simple relation of $\Delta\lambda = \Delta\lambda(V)$ was derived [48] in which the complicated influence of the suspension geometry (lengths, width, thickness, bending, number of suspensions), the material parameters (composition, number of periods) and the membrane geometry can be incorporated approximatively via first, the spring constant k and second, the optical tuning efficiency $\eta = \Delta\lambda/h$.

$$V = L\sqrt{\frac{2k}{\varepsilon A\eta}\Delta\lambda} - \sqrt{\frac{2k}{\varepsilon A\eta^3}\Delta\lambda^3} \quad \textbf{2.15}$$

In this formula L denotes the cavity height at $V = 0$, A the membrane area, ε the permittivity of the air, and h is the change of the air cavity height which is equal to the displacement of the movable plate according to Fig. 2.14 and Fig. 2.16. Generally, the value of tuning efficiency is calculated by means of TMM. For $t \ll \ell$, $h \ll L$ and $t \ll w$, the spring constant can be approximated from the equation $k = Ewt^3/4\ell^3$ where w, t, ℓ, E are the width, the thickness, the length, and the Young modulus of the equivalent materials of the membrane, respectively [49].

According to Eq. 2.15, as an example of micromachined tunable FP filter ($L = 325\ nm, A = 5206\ \mu m^2, k = 413\ N/m, \eta = 0.7$) the relation $\Delta\lambda = \Delta\lambda(V)$ has been calculated and displayed in Fig. 2.10. Note that the values chosen for k and η are arbitrary, just for an example. The calculation is implemented when considering an DC voltage actuation is applied. As seen from the figure, with growing applied voltage, the air-gap cavity is decreased and thus, the wavelength of the filter transmission line decreases.

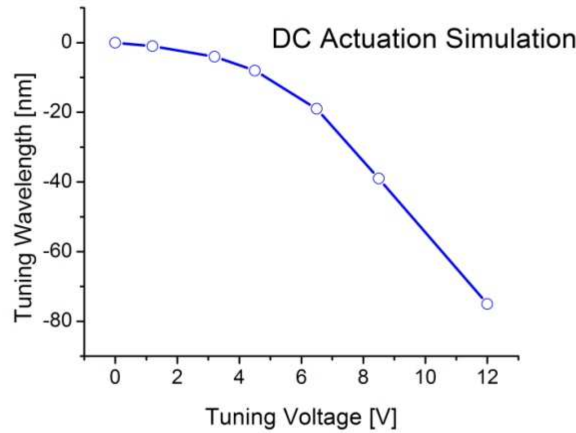

Fig. 2.10. Tuning of an electrostatically actuated FP filter device: transmission line wavelength as a function of applied DC voltage.

The optical tuning efficiency depends on three main parameters: the DBR design, the cavity height, the filter's lateral geometry and the spectral position of the DBR central frequency relative to the design wavelength. A simple simulation of the dependence of tuning efficiency on the cavity height is illustrated in Fig. 2.11 [32]. The simulation is applied for the filters with 5.5 periods of TiO_2/SiO_2, the height L of air gap cavity is of 550 nm, the filter's lateral geometry is not considered in this case. The change of cavity height is depicted as $\partial \cdot L$ with - $0.4 < \partial < 0.4$. As seen from the figure, increasing the height of the air gap L results in the decrease of the tuning efficiency. In fact, tuning efficiency also depends strongly on other parameters, much more than shown in the figure with the dependence on the cavity height. Theoretical calculations and experimental results demonstrate that a better tuning efficiency is achieved if the filter is implemented with a laterally extended , with a low number of suspensions, and with long, laterally bent-shaped suspensions [48, 50, 51].

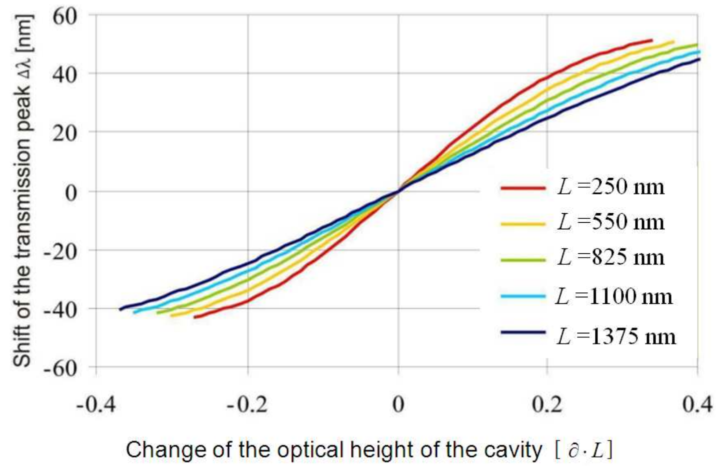

Fig. 2.11. Tuning of FP filters: Wavelength of filter transmission line as a function of cavity height [32].

2.1.5.2 Tunable Fabry Pérot filter arrays

Tunable FP filter arrays can be considered as a derivative type of static filter arrays. The micromachined tunable nanospectrometers is composed of a detector array and a corresponding array of different micromachined tunable FP filters whose cavities are air gaps that can be varied by a few nm in heights by electrostatic actuation [24, 45]. The basic motivation of developing tunable filter arrays is to fabricate cost-efficient nanospectrometers for the IR or the UV range. In the UV range, the involved dielectric layers suffer from increasing absorption with decreasing wavelength. Air gap cavities have no absorption, and thus, offer superior performance in UV spectroscopy and offer tuning options. For wavelengths > 1 μm, Si-based detector arrays have to be replaced e.g. by much more expensive InGaAs detectors [52]. Nevertheless, low cost IR nanospectrometers are possible by considerably reducing the number of individual detectors (and filters in the array). Therefore, a tunable nanospectrometer with different tunable FP filters can be designed to detect a broad wavelength range.

The scheme of a tunable FP filter array illustrating its working principle is shown in Fig. 2.12. Different initial air cavity heights (i.e. the air cavity heights without tuning) are designed to obtain different initial wavelengths of the corresponding filter transmission lines of FP filters. Similar to the static filter arrays, 3D NanoImprint technology is used to structure the dimensions of all the supporting posts and sacrificial layers (subsequently the air gaps) of different heights together in only a single NanoImprint step. Afterwards a process to pattern the micromachined structure including lithography, vertical etching, and protection layer fabrication and finally sacrificial layer underetching is performed to implement air cavities with different heights. At the end, top and bottom electrodes are deposited [44]. The tuning is performed by electrostatic actuation, i.e.

applying a voltage between the contact electrodes. The electrostatic forces between these electrodes move the upper suspended DBRs and alter the cavity heights appropriately [22, 53].

Figure 2.13 depicts an electron micrograph of a tunable FP filter with 9.5 periods of Si_3N_4/SiO_2 DBRs deposited by PECVD. The cavity layer is the polymer mr-UVcur06 which is suitable for UV NanoImprint technology. The polymer which is used as a sacrificial material has been removed selectively by oxygen plasma to create an air cavity after underetch. Outside the suspensions and membrane region, the polymer still exists in the supporting post region.

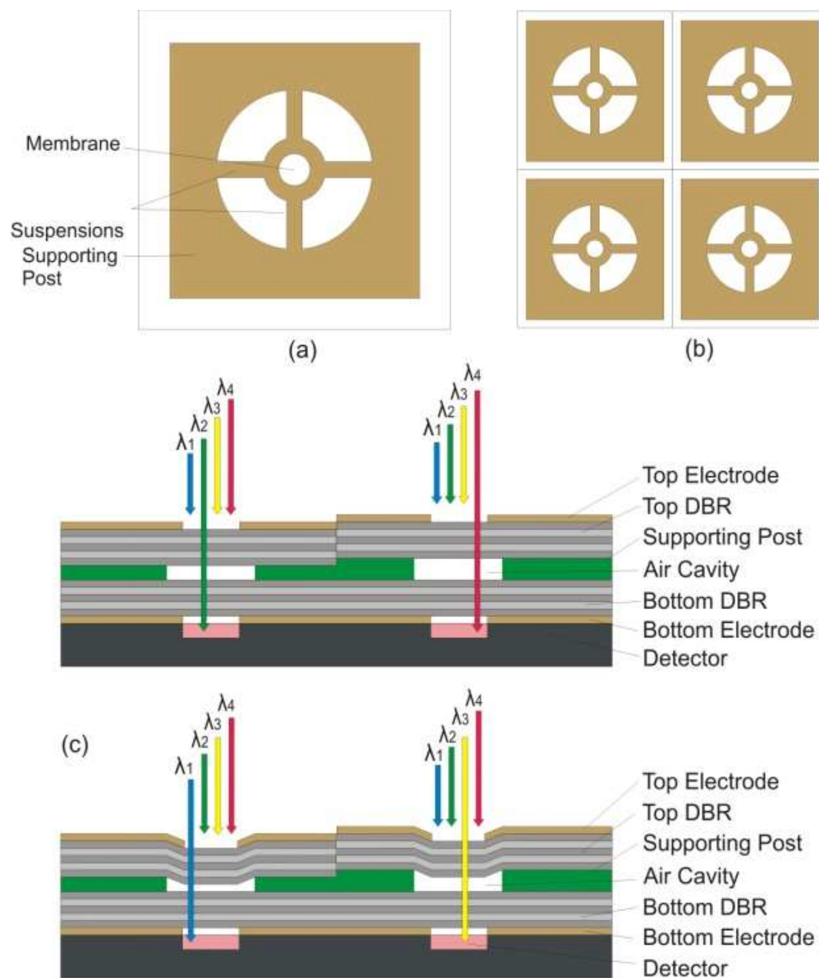

Fig. 2.12. Scheme of an tunable FP filter array design: (a) top view of a single tunable filter, (b) top view of a filter array, (c) cross sectional view without (top) and with electrostatic tuning (bottom) [22].

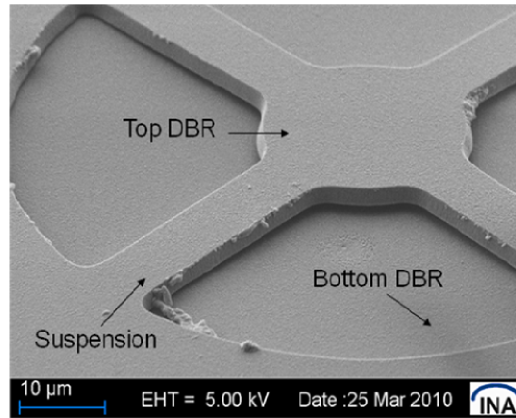

Fig. 2.13. SEM micrograph of a micromachined tunable FP filter [22].

2.1.5.3 A simple elastic capacitor model of a micromachined tunable FP filter

In micrometer and nanometer scale, the electrostatic force is often used for actuating MEMS devices in general and FP filters in particular [54-56] due to its dominance against other fundamental forces. In order to investigate the static and dynamic mechanical properties of a FP tunable filter in terms of temporal membrane stability and electrostatic actuation efficiency, a simple elastic capacitor model is applied as an approximation (Fig. 2.14). The two DBRs can be considered as two parallel plates of a capacitor where one plate is typically fixed and the other is suspended by several suspensions, which are here combined into a single mechanical elastic spring.

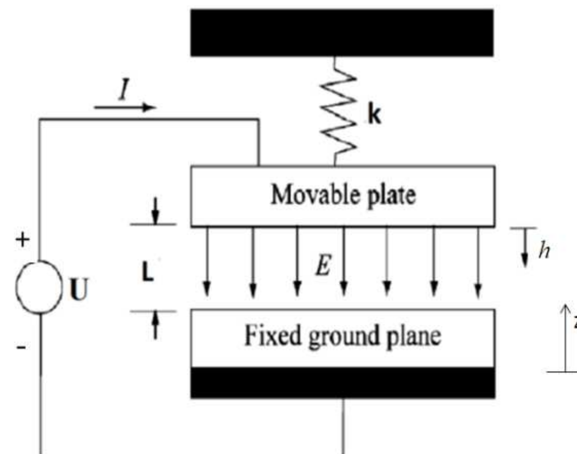

Fig. 2.14. Scheme of a one dimensional capacitor model. The initial cavity height when the applied voltage is zero is depicted as *L* [57].

The initial height of the air gap cavity is . When a voltage is applied, an attractive electrostatic force is generated and pushes the movable plate to move down in the vertical direction (z direction) which results in the decrease of the air gap. The position of the

movable plate in the z direction is called membrane displacement h, and is controlled by the equilibrium between the electrostatic and mechanical restoring forces of the suspensions, respectively. Each different applied voltage establishes another equilibrium between the forces and provides another distinct displacement h resulting in another distinct cavity height and, thus, in another filter transmission line wavelength.

Using Newton's Law, a movable plate capacitor can be described by a mechanical oscillator model including inertia, friction, elastic feedback and gravity which is completed by an electrostatic force:

$$m\frac{d^2h}{dt^2} + \zeta\frac{dh}{dt} + kh - F_e - F_m = 0 \qquad \textbf{2.16}$$

where m is the mass of the moving plate or in this case the top DBR including an effective part of the suspensions, ζ is the damping coefficient and k is the spring constant. The distortion h indicates the displacement of the movable plate in the vertical direction. The mechanical restoring force acting on the moving plate is defined by the product kh. F_e is the electrostatic force. F_m describes the forces that the capacitor experiences such as ambient gravity or other external forces [58, 59]. This differential equation is well known from physics as a *damped oscillator with external excitation*. In the quasi static analysis of the considered oscillator, the variation of the movable plate (top membrane) is slow enough, so that the top membrane is in equilibrium all the time i.e. the time dependent terms in Eq. 2.16 vanish.

When a voltage V is applied across the capacitor, the charge Q relates to the external voltage V as follows:

$$Q = \frac{\varepsilon AV}{L-h} \qquad \textbf{2.17}$$

The electrostatic force can be expressed by the following formula:

$$F_e = \frac{Q^2}{2\varepsilon A} = -\frac{d}{dh}\left(\frac{1}{2}CV^2\right) = \frac{\varepsilon AV^2}{2(L-h)^2} \qquad \textbf{2.18}$$

where ε is the permittivity of free space.

C the capacitance,

A the membrane area

L the initial cavity height of the air gap and

V the DC applied voltage.

The capacitance of the parallel plate is:

$$C = \frac{\varepsilon A}{L - h} \quad 2.19$$

Assume that there is only an electrostatic force and no other external forces, i.e. $F_m = 0$. At equilibrium, the electrostatic force is balanced by the elastic restoring force so Eq. 2.16 is simplified as:

$$\frac{\varepsilon A V^2}{2(L - h)^2} = kh \quad 2.20$$

By solving Eq. 2.20, the voltage V is achieved as [47]:

$$V = \sqrt{\frac{2(L - h)^2 kh}{\varepsilon A}} \quad 2.21$$

The maximum of external voltage which can be reached without finishing reversible displacement operations of the capacitor is called pull-in voltage V_{pi} as shown below:

$$V_{max} = V_{pi} = \sqrt{\frac{8kL^2}{27C_0}} \quad 2.22$$

where $C_0 = \varepsilon A / L$ is the initial capacitance when $h = 0$.

The maximum plate displacement h_{pi} at the pull-in voltage is:

$$h_{pi} = \frac{L}{3} \quad 2.23$$

The relation between voltage V and the displacement h is shown graphically in Fig. 2.15:

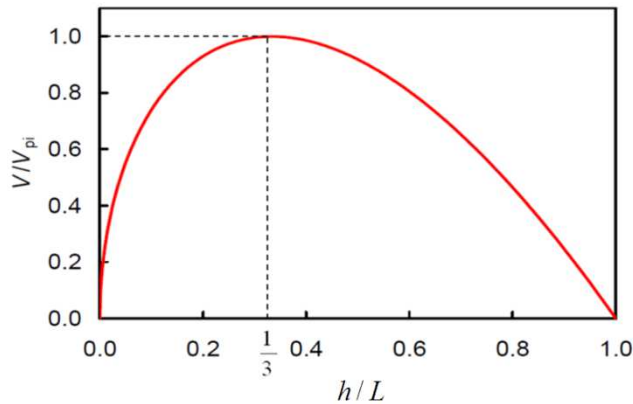

Fig. 2.15. Voltage of a movable plate capacitor as a function of displacement. The applied voltage reaches a maximum V_{pi} if the displacement is approximately $L/3$ one third of the initial air gap [58].

When the applied voltage is increased above the pull-in voltage, the electrostatic force will exceed the elastic restoring force, the equilibrium is lost and the movable plate collapses on the fixed plate. Eq. 2.22 and Eq. 2.23 show the stability limit of a tunable FP filter actuated by an electrostatic voltage. The filter is only stable below the pull-in voltage, and below approximately the displacement $L/3$ [58]. For a precise calculation of the critical displacement see [47]. The pull-in limitation originates from the fact that the charge Q depends on the remaining gap $(L - h)$ as shown in Eq. 2.17. As a result, the electrostatic force becomes nonlinear due to its dependence in $1/(L - h)^2$ whereas the elastic restoring force $F_e = kh$ is linear with h. As the remaining gap decreases, the electrostatic force increases nonlinearly while the restoring force increases linearly which leads to the instability of the system.

In consequence, the instability in mechanical tuning behavior of the filter affects directly its spectral performance e.g. maximum wavelength tuning, $FWHM$ etc. In fact, the stability of a system is influenced by many factors such as: the material, the lateral filter geometry, the geometry of the mechanical construction of the system and the dielectric charging [60]. Among those above mentioned factors, dielectric charging has received a lot of attention in the field of micro-electro-mechanics (MEMS field). It has been proven that the dielectric charging is also crucial for micromachining involving dielectric and is increasing of the pull-in voltage [58]. Since the first observation of charging effect by Tang et.al. in a stacked oxide-nitride dielectric of polysilicon [61], many researchers have been conducted to find ways to reduce the effect of the dielectric charging, and thus stabilize the system [62-66].

In tunable FP filter arrays, reducing the dielectric charging will not only help to stabilize the system but also increases the efficiency of electrostatic actuation [58]. That means it can provide the possibility of reducing the required applied voltage to obtain a desired spectral tuning range. This is an important issue in the applications of the micromachined tunable FP filters in nanospectrometers.

In the following part, the mechanical behavior of the tunable FP filters is studied for two different electrostatic actuation cases: a quasi static time-invariant actuation (DC) and a time-variant actuation (AC). This will be the basis for chapter 5, in which experimental studies using DC and AC actuation are presented. The focus on the DC and AC actuation are (i) the dielectric charging and (ii) the temporal stability of the FP filter membrane. Note that the basics of the two sections DC and AC actuation are repeated also in chapter 5 during the description of the DC and AC actuation experiments. It will be shown that if a DC bias voltage is used to micromachined actuated a FP filter, dielectric charging is considered as the main reason which results in the temporal instability of the system.

DC actuation

Since in this work, micromachined tunable FP filters including dielectric DBRs (SiO_2/Si_3N_4 or SiO_2/TiO_2) in this chapter includes the basics of possible charge transfer from conductive electrodes into the DBR dielectrics, which is called *charging effect*. Those materials have high insulation resistance, however they include also traps for positive and negative charges both deep in volume and at the multiple interfaces in multilayer stacks [66]. A schematic and simplified charge distribution inside a dielectric tunable filter with two dielectric surfaces against an air gap is demonstrated in Fig. 2.16 below. To study charging effects we have chosen a design where the charging effects are extremely active, in order to prepare a scientifically most interesting situation, which is displayed in Fig. 2.16. This is due to the fact that charges preferentially occupy central surfaces of a plate capacitor; therefore, they are cordially invited to charge the dielectrics, since the conductive electrodes are located at the outer borders of the dielectric DBRs.

A new model based on rate equations will be presented in chapter 5 to explain the experimental data observed in the experiments.

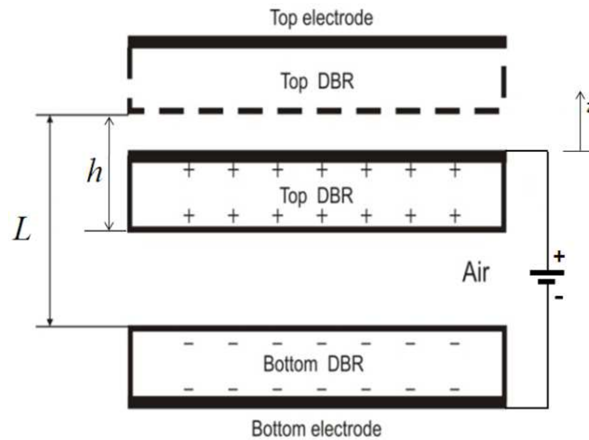

Fig. 2.16. Simplified model of charge distribution after a DC voltage has been applied for a long time. The charging effect is studied in this specially designed FP filter geometry which is superior to study charging since the dielectrics are located in the center. This geometry will provide a situation where charging is revealed extremely.

If a DC voltage is applied between the top and bottom electrode of the tunable filter (one electrode has always a positive potential, the other electrode has always a negative potential), an electric field is generated between the two electrodes. Immediately after the DC voltage is applied, the positive or negative charges are located at the central interfaces of the conductive electrodes. After some time, some the charges are continuously transferred into the dielectric layers and then are relaxing into interface or bulk

traps in the dielectrics (trapping). The amount of charges trapped in the dielectric materials increases gradually with time. This has an influence on the electrostatic force between the DBR mirrors covering the transparent electrodes outside moves, thus, the filter behavior becomes temporally unstable. Note that the detailed very much depend on the geometry and the involved materials [65].

Another effect also may occur in addition: Due to the distance between the top DBR and the bottom DBR is not larger than one micrometer; already a few volts will generate a very high electric field. When the applied voltage is increased further, exceeding the breakthrough voltage of the air, the air is ionized which leads to the generation of an avalanche of free electrons and ions. These free electrons and ions traverse through the gap and are stopped and neutralized by the trapping charges in the bottom DBR [65, 66]. As a result, the electric field is reduced further. The electrostatic force drops drastically and the membrane is further released.

Beside the effect of trapping charges in dielectric layers and the breakthrough of the air gap, the effect of leakage current arising from undesired imperfections of dielectric materials also give rise to the discharging of the filter. As a result of imperfect isolation, the dielectric materials have some non-zero conductivity. This allows a leakage current to flow; the filter is slowly discharged; then the system becomes unstable, and the top DBR moves backward towards the initial position.

Obviously, the effect of charging on the dielectric leads to a temporal instability of the micromachined tunable FP filter. Furthermore, since the electric field is reduced gradually, it is required to increase the applied voltage in order to compensate the reduction. This undesirable effect is troublesome in the application of the tunable FP filter where low applied voltages with high efficiency of electrostatic actuation are required. Therefore, in order to enhance the temporal stability of the system and to decrease the applied voltage, a proper method to eliminate the dielectric charging effect has to be addressed. In the next section, a method used for significantly reducing the charging effect by using an AC voltage actuation is presented and discussed in detail.

AC actuation

Studies of micromachined electrostatically actuated devices have indicated that the presence of DC voltage driving gives rise to the appearance of trapped charges in dielectric layers which will may considerable degrade the device. The devices become temporally unstable and require after some time gradually increased DC voltages applied. In order to eliminate this phenomenon, a straightforward way is to use an AC voltage actuation instead of DC voltage.

In general, positive charges are trapped if a positive potential exists. On the contrary, negative charges are trapped if a negative potential exists. When only an AC actuation voltage is applied, the two electrodes alternate continuously between positive and negative potential. Even though the polarities of the two electrodes change alternatively, the direction of the electrostatic force generated between the two electrodes does not change. The electrostatic force is always attractive which forces the top DBR to move down which results in the reduction of the air gap cavity.

Since the polarities at the two electrodes alternatively change from positive to negative values, at each electrode positive charges are trapped during a period of positive potential and negative charges are trapped in the subsequent period of negative potential. The trapped charges will be partially neutralized, and the influence of dielectric charges can be partly reduced by this way [65]. As a consequence of the strong reduction in charging effect, the required (temporally compensating) increasing voltage for electrostatic actuation can be maintained small or can be even omitted.

In deriving Eq. 2.21, it has been assumed that the displacement h is static, i.e. the filter does not oscillate mechanically due to the applied voltage. This is naturally valid for DC. In the case of AC voltage, displacement is approximatively static if the frequency of the applied voltage is much higher than the mechanical resonance frequency of the oscillator. In this case the top DBR cannot follow the fast oscillation of the electrostatic actuation frequency, the membrane becomes almost stationary.

In the applications of micromachined tunable FP filter arrays in nanospectrometers, a high temporal mechanical stability and a low voltage applied are the priorities. Therefore, the utilization of AC actuation voltage at frequencies much higher than the resonance frequency of the FP filter is preferable. In order to investigate the behavior of the FP filters when a DC or an AC voltage actuation is applied, in this work, spectral and mechanical characterizations of the FP tunable filter have been performed and reported in chapter 5. There, details of the obtained experimental results in these two cases are analyzed and presented.

In fact, even in the absence of an external DC voltage, when the ideal AC voltage is applied, the filter still experiences a small effective DC voltage. This DC part originates from parasitic capacitances which are typical for all devices: transistors, laser diodes, LEDs, photodiodes etc. Those parasitic capacities also exist and cannot be avoided in micro-electro-mechanical devices [58], [59]. As an AC voltage is applied, the parasitic capacitances are first charged gradually after the filter is biased. The transfer of charge from the capacities to the dielectric is going on permanently but always is proportional to the currently remaining charge in the capacities. In some cases the parasitic capacitance acts as a parasitic DC voltage source applying on the tunable filter [59]. Thus,

even without an externally applied DC voltage in many situations the filters have a parasitic DC biasing. The total voltage is in this case:

$$V = V_{DC} + V_0 sin(\omega t) \quad \textbf{2.24}$$

V_{DC} is the DC voltage arising from parasitic capacities. This undesirable DC voltage results in the reduced temporal stability of the filter. This phenomenon is also discussed further in chapter 5.

2.2 Optical characterization methodology

Optical spectroscopy is attractive for the investigation of the optical functionality of the FP filter arrays due to its high sensitivity, spectral selectivity and nondestructive features. It is useful for long-term and real time inspection without contaminating the sample. A common optical characterization setup, shown schematically in Fig. 2.17, is composed of (i) an illumination system, (ii) a collimation and magnification system, (iii) a sample stage, and (iv) a data recording and analysis system.

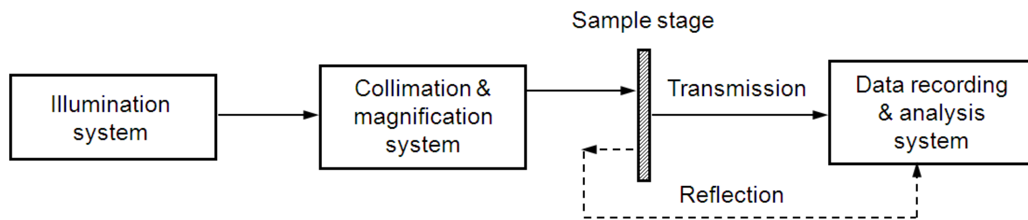

Fig. 2.17. Scheme of a characterization setup.

The light source is the main component of the illumination system, which could be a laser, an LED or a lamp and has to be adapted to the desired spectral properties. The collimation and magnification system includes either a series of optical elements or a microscope which is vitally important for forming a collimated or focus light beam. In this system, the objective lens is a key part which determines the diameter of the focused light spot and the limit of image resolution. The sample stage is used for carrying the filter arrays, defining the exact position to be characterized within the array and allows for scanning through the whole filter arrays in a step and repeat modus. The data recording and analysis system contains either an optical grating spectrometer, or an optical spectrum analyzer (OSA), or a charge coupled device (CCD), allowing quantitative analytical data processing and quantification.

2.2.1 Ilumination systems for optical spectroscopy

In spectroscopic studies, the light source plays a key role. It is needed to generate a beam of radiation with sufficient power for measurement and detection signal. In addition, the light intensity should be stable. Any fluctuation in light intensity which causes a significant variation in the spectral accuracy should be avoided. In optical spectroscopy, both continuous and line sources are used. However, due to the wide range applications of our FP filter arrays, continuous light sources with broad spectral range, sufficient power, and wide dynamic range which can operate in both spectral ranges such as the visible and NIR range are required. In this study, we utilize a Halogen (HAL) lamp and a continuum laser as continuous light sources which can fulfill the requirements of efficient power and large spectral working range.

2.2.1.1 Halogen lamp as illumination system

Halogen (HAL) lamps are the most common forms of thermal and incoherent sources for visible and NIR radiation. The HAL lamps operate as thermal radiators i.e. light are emitted by heating the filament at high temperature. The radiative emission of HAL lamps is approximated as a black body spectrum and is thus temperature dependence. As a property of black body radiation, the spectral distribution is shifted to shorter wavelengths when the temperature is increased. In Fig. 2.18 various temperatures are taken into account to illustrate the spectral behaviors of the HAL lamps. The higher the temperature (only up to 6500 K) the more the maximum peak shifts to shorter wavelengths corresponding to the enhancement of the portion of the visible light. In contrast, the lower the temperature results an increasing part of longer wavelength appears in the spectrum. As seen in the figure, at 3200 K the spectrum is continuous over the range between about 300 nm and 2500 nm, however the red region dominates the whole spectrum. The majority of the emitted energy (approx. 85 %) is distributed in the NIR and IR range, the rest falls into the visible (approx. 15-20 %) and UV range (less than 1 %). Therefore, the HAL lamp is an ideal radiation source for applications with sufficiently high optical power in both the visible and NIR working range. When compared with other light sources, the HAL lamps are relatively cost efficient, easy to replace, and provide adequate illumination [67]. It is also considerably stable in long term experiments; therefore, spatial and spectral fluctuations under normal operating conditions are nearly suppressed. Besides these advantages, the main disadvantages of the HAL lamps are their poor beam quality and their low coupling efficiency into an optical fiber which often results in a low power at the detectors.

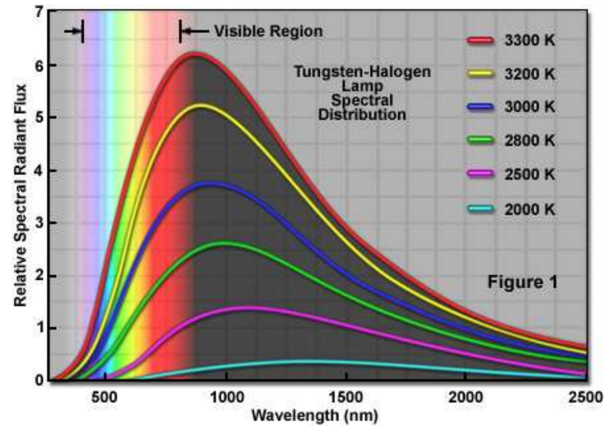

Fig. 2.18. Spectral distribution of a Tungsten Halogen lamp [68].

In this work, two HALs are utilized in the illumination system. Figure 2.19 presents the broad and continuous spectrum of the HAL lamps for the light propagating through the compact microscope spectrometer setup (which is discussed in chapter 3). The spectrum is captured in the range of 350 – 1150 nm. Note that, the compact microscopes spectrometer setup is designed to work in the visible range. Therefore, the reduction of the optical power in the NIR range displayed in the spectrum is referred to the attenuation of the light when it propagates through the internal optical elements of the microscope. The HAL lamps provide an adequate and stable illumination in long term experiments. These features help to eliminate spatial and spectral fluctuations during measurements.

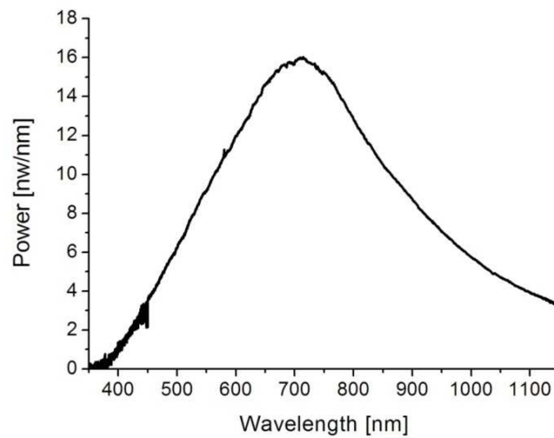

Fig. 2.19. Spectrum of the HAL lamps propagating through the compact microscope spectrometer setup.

2.2.1.2 Supercontinuum white light laser as illumination system

As compared to the properties of HAL lamps, laser produce a beam of extremely high intensity, spatially narrow and with remarkable spatial and temporal coherence that can

be coupled efficiently into fibers [69, 70]. The laser beam, however, is usually monochromatic with a narrow bandwidth of 0.01 nm or less. To cover a broader spectral range, a tunable laser is commonly utilized. In fact, there are several tuning principles, Ti-Sapphire laser, dye laser, and others [71]. Another approach to broaden the spectral range is a combination of several different lasers emitting at different wavelengths is established. This combination, however, makes an illumination system even more sophisticated and large in volume.

A supercontinuum white light laser source (SCWLL) which takes advantages of broad spectral range of incandescent lamps and high intensity of lasers is another suitable approach for spectroscopy studies [72]. SCWLL can be described as “broad as a lamp and bright as a laser” [73] with broad spectral range covering over the visible and NIR and considerably higher intensity than other kind of broadband sources. Figure 2.20 depicts a comparison in spectrum between a photonic crystal fiber based supercontinuum source and different broad band sources such as: an amplified spontaneous emission source (ASE source), an incandescent lamp, and four superluminescent diodes (SLEDs).

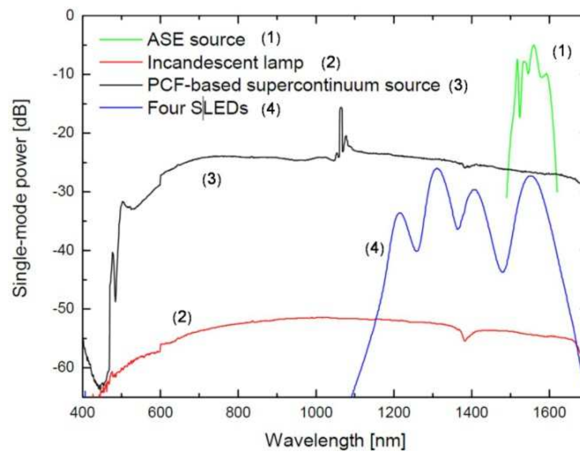

Fig. 2.20. A comparison of spectra of a supercontinuum white light laser based on a Ti-Sapphire pump laser and different broad band sources [74].

Since the SCWLL produces the light already inside a photonic crystal fiber using mainly stimulated emission processes this method of light generation is superior to that of e.g. a halide lamp, which often requires coupling the light into a fiber after the generation based on mainly spontaneous emission.

A supercontinuum generation is defined as a formation of a broad continuous spectral band when a pulse with high peak power propagates through a nonlinear medium. The first observation of supercontinuum radiation was first reported in 1970 by Alfano and Shapiro [75]. They observed a continuous broadening of spectral output (from 400 nm to 700nm) by launching a neodymium laser beam with energy of about 5 mJ through a

borosilicate glass. This initial finding, as well as later research on stimulated radiations from solid state materials, liquid, gas medial, and optical fiber created a new generation of a powerful artificial white light source with unique spectral properties [76-78]. The generation of supercontinuum radiation can be explained in many aspects such as self phase modulation, stimulated Raman scattering, four wave mixing and soliton fission.

As a property of nonlinear medium, when a strong field of laser light is launched into the medium, the refractive index of the medium is modulated by the incident beam which leads to the self phase modulation. This effect is realized as the main source of the broadening of spectra in nonlinear media such as: calcite, quartz, sodium chloride, Ti-sapphire etc.

In addition to self phase modulation, stimulated Raman scattering and four wave mixing also contribute to the broadening of the output spectrum [79]. Those effects are considered as the basic to interpret the generation of the continuum radiation in optical fibers. Compared to other case of supercontinuum spectral generation, the radiation intensity generated in optical fibers is rather low. The emitted spectra, in contrast, cover the entire visible and a considerable part of the NIR [80].

Besides those mentioned effects, the fission of soliton was recently implemented as an origin of the supercontiuum radiation in photonic crystal fibers or highly nonlinear fiber by Ranka et. al in 2000 [81]. Compared to other supercontiuum generation in other kinds of matter, the supercontiuum spectra in photonic crystal fiber is regarded as the widest spectra which can be obtained by propagating a femto second laser spectrally close to the wavelength where we have zero dispersion [82]. Solitons are generated if a balance between self phase modulation and group velocity dispersion occurs during the propagation of the soliton femto second pulse. The femtosecond pulse is considered as a high order soliton, consequently it rapidly broadens and then fissions into fundamental solitons [83-86]. Since all fundamental solitons and their corresponding nonsolitonic radiation have different frequencies, the width of the generated spectrum increases with increasing soliton numbers or with pulse durations [87].

Due to a broad range of application of the FP filter arrays (from the visible to NIR range), at INA a SuperK EXTREME supercontinuum white light lasers[2] [73] is utilized as a light source for optical characterization of the FP filter arrays. In contrast to Fig. 2.20 our SCWLL uses a Nd-YAG laser as a pump laser. The laser delivers a very wide spectral output covering from 460 to 2400 nm while still providing a high average power of about 4.3W as shown in Fig. 2.21. Since the pump laser has very good beam quality it can be very efficiently coupled in the photonic crystal fiber where the

[2] SuperK Extreme Supercontinuum laser, Koheras

supercontinuum is generated. Therefore, there is no need for coupling light into a fiber, involving very weak coupling efficiencies. The laser output is a single mode Gaussian beam with the beam quality M^2 less than 1.1, and the beam divergence is less than 5 mrad. Furthermore, the supercontinuum laser produces high optical powers in the fiber, which still provides enough intensity per wavelength interval and therefore allows measuring the weak signals passing FP filters of very small linewidths.

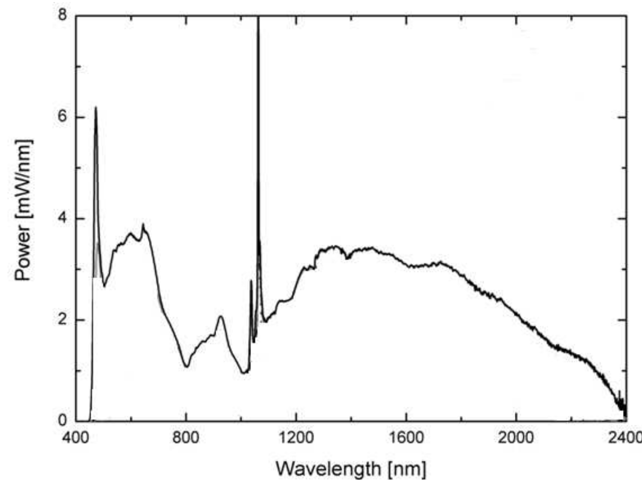

Fig. 2.21. Spectra of the supercontinuum laser based on a Nd-YAG laser as a pump laser which is used in chapter 6 [73].

The spectral emission profile of the SCWLL sensitively depends on the pump laser wavelength and power, the kind of photonic crystal fiber and other optical components. The spectrum shown in Fig. 2.21 corresponds to an Nd-YAG laser pumping at its maximum. Reducing the pump power strongly modifies the spectral extension of the emission profile. With increasing pump power the spectrum is increasingly extending to the short wavelength range.

2.2.2 Collimation and magnification systems for optical spectroscopy

In optical spectroscopy, the collimation and magnification system is important to form a focus or a collimated light beam and magnify or de-magnify the image. The main components of the collimation and magnification system are lenses that can be used either to focus a parallel beam of light into a spot or in a reverse way to spread a point source of light into a parallel beam.

In the process using FP filter arrays for spectroscopic characterization, a collimation and magnification system is required to create both, a collimated light beam and a parallel wave front at the filter surface. This can be obtained in the beam waist of a focus. Due

to the fact that the FP filters consist of multi optical layers, this feature make them very susceptible to the angle of incident beam illuminating the filters [88]. The transmission peak will widen if the angle of incidence is not vertical. Theoretical calculation of different incident angles on the transmission spectra is presented in Fig. 2.22. The filter consists of 9.5 periods of Si_3N_4/SiO_2 as top and bottom DBRs, the central wavelength is of 650 nm, the material for cavity is mr-UVCur 06, the cavity height is chosen as $\lambda/2$. As the incidence angle increases, the center wavelength of the FP filter will shift to smaller wavelengths. As a result, the spectrum achieved from oblique incidence presents a significant difference from the spectrum from perpendicular incidence. It can be seen that at less than 1° of incidence angle there is below 0.1 nm wavelength shifts in the spectral response as compared to the vertical incidence case. At 3° angle the wavelength shift is increased to 0.35 nm, and the value of 1nm shift is obtained in the case of 6°.

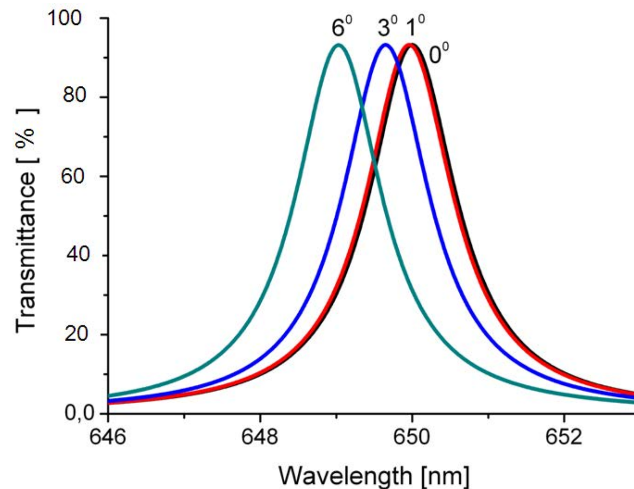

Fig. 2.22. Transmission spectra of a multiple thin film FP filter illuminated by different incident angles.

In this study, several kinds of lenses and complex optical lens systems which are commonly used in optical spectroscopy to create a beam waist with parallel wave fronts i.e. a "perpendicular beam" with respect to the sample surface such as: objective lens, condenser, and microscope are taken into account. Their functionalities of creating such a beam are discussed in detail in the following parts.

2.2.2.1 Objective lenses for optical spectroscopy

An objective lens is a system of several lenses which gather light from an object being observed, focuses the light beam and produces a real image. Depending on the degree of aberration correction, objective lenses are divided into three classifications such as:

Achromatic, Fluorites and Apochromatic. Optical aberrations are caused by artifacts arising from the interaction of light with glass lenses such as coma, astigmatism, distortion, vignetting, geometrical and chromatic aberrations [89]. Among these optical aberration, geometrical aberrations and chromatic aberrations are the primary cause of aberration in an optical system [89, 90].

The most common objective lenses are Achromatic objectives which can correct the chromatic aberration for two wavelengths (e.g. red and blue). They also correct spherical aberration for one wavelength (e.g. green). The higher level of correction is Fluorites objectives which enable to chromatically and spherically correct for two wavelengths. The highest level of correction is Apochromatic objectives, which are able to chromatically correct for three wavelengths or even more (e.g. red, green and blue) and spherically correct for two wavelengths. Due to higher level of correction, Apochromatic objectives can provide a better resolving power, and a higher degree of contrast than the others [91].

Every objective lens has parameters representing the most important specifications such as: numerical aperture (NA), magnification of the object, working distance, and immersion. Among of them, numerical aperture is a critical parameter which defines one of the most important optical features: the resolving power. Generally speaking, the numerical aperture is defined as a dimensionless number that defines the range of angles under which the objective lens can gather the light. The numerical aperture is calculated by the following equation:

$$NA = n\,sin(\alpha) \qquad \textbf{2.25}$$

In which n is the refractive index of the environment between the specimen and the objective lens, and α is the maximum angle under which the objective lens can gather the light.

When the specimen is illuminated by an incident beam, the light beam is diffracted by the specimen. The light diffracted is brought into focus at the image plane by the objective lens. Here, the direct and diffracted lights cause constructive and destructive interference resulting in bright and dark areas. These patterns of bright and dark are recognized as an image of the specimen.

Figure 2.23 represents the diffraction patterns resulting from two circular apertures have a bright region in the centre and some dark regions on both sides. The patterns are known as Airy disk. When the Airy disks are far apart, their images are well resolved (Fig. 2.23 (a)). When two disks are so close (Fig. 2.23 (c)) then the sum of two diffraction Airy disks is indistinguishable from one, thus, the images are not resolved. The limit at which two Airy disks can be resolved into separate entities is called the Ray-

leigh criterion. At the limit of resolution, the first minimum of one diffraction image overlaps with the central maximum of the neighboring diffraction image as can be seen in Fig. 2.23 (b) [92]:

$$d = 1.22\frac{\lambda}{2NA} \quad \mathbf{2.26}$$

where d is the smallest detectable distance between two adjacent points on a men, λ is the wavelength, and NA is the numerical aperture of the objective.

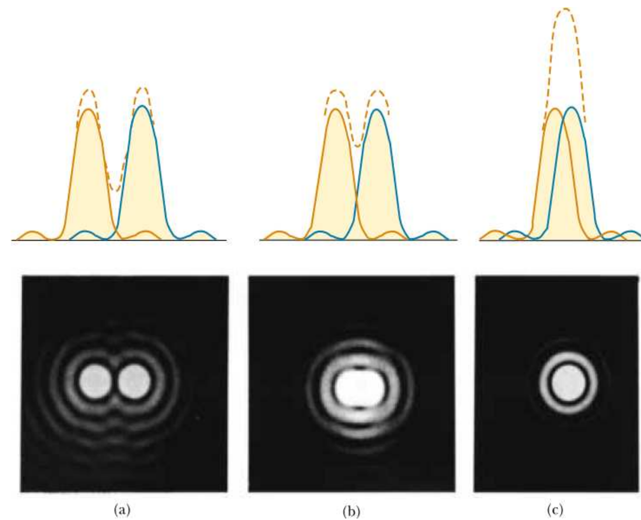

Fig. 2.23. (a) Individual diffraction patterns of two Airy disks (solid curves) and the resultant patterns (dashed curves). The Airy disks are far apart, and the patterns are well resolved. (b) The Airy disks are on the limit of resolution according to Rayleigh's criterion, the patterns are just resolved. (c) The Airy disks are so close together that their central spots overlap, thus the patterns are not resolved [93].

It is apparent that the higher the numerical aperture, the shorter the incident wavelengths, the smaller and finer the structure which the objective lens can resolve. Therefore, increasing the numerical aperture and using shorter incident wavelengths is crucial in microscope implementation technology and microscopic research.

This equation can be used to estimate the size of the spot focused by the objective lens on the specimen. At focus, the beam forms an Airy disk pattern. If the full aperture of the objective lens is illuminated, the smallest spot size is determined by the size of the middle spot of an Airy disk. As a consequence we can consider that the spot size is equivalent to the resolving power of the objective lens [91].

In any characterization setup, the objective lens is a critical part which is assigned to project a light beam on the sample. At the beam waist, the wavefront is almost planar and the beam "almost hits the sample perpendicularly". Therefore, it can sufficiently

limit the effect of shifting to shorter wavelengths in the optical characterization of the FP filter arrays.

2.2.2.2 Optical microscopes and condensers for optical spectroscopy

The optical microscope has emerged as an indispensable, powerful tool for many fields of applications. In spectroscopy, the microscope with its magnifying power is useful to characterize optical properties of microscopic samples or microscopic features of a large scale sample. In fact, a hybrid instrument which integrates an optical microscope with a grating spectrometer is capable of measuring transmission and reflection spectra of samples on a micro scale or smaller [53, 94]. It can even be configured to measure fluorescence and luminescence spectra.

In order to understand microscopy operation methodology, the working principle of a microscope is described in the following part. A modern microscope includes a series of optical elements such as objective lens, condenser system, eyepieces, tube lens, beam splitter, mirror, etc.. The basic operating principle of an infinite microscope is represented in Fig. 2.24 below. An objective lens which is a high magnifying lens with a short focal length is implemented. A specimen (**O**) being examined is brought very close to the objective lens. The light from the specimen comes to a focus at an intermediate image plane located at a fixed distance inside the microscope tube. This creates an enlarged and inverted image of the subject (**O'**). The image is then magnified further by an eyepiece, produces an image of the specimen on the retina which appears inverted to the users.

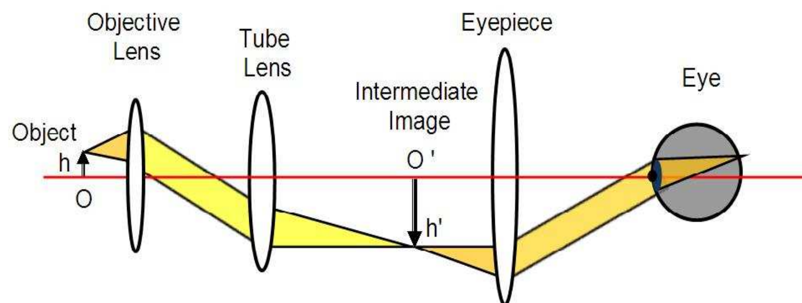

Fig. 2.24. Optical ray traces of a microscope system corrected to infinity.

In microscopy, the homogeneous illumination of the specimen is crucial to achieve high resolution images. In order to fulfill this requirement, in 1893 August Köhler introduced a predominant method which can provide optimum illumination on the specimen by creating a parallel and collimated beam illuminating the specimen [95]. Compared to the conventional microscope, modern scientific microscopes which are designed based

on the Köhler illumination require additional optics such as: field lens, field diaphragm, and condenser.

The functionality of creating parallel light beam using Köhler illumination is illustrated in Fig. 2.25. The field lens projects an image of the lamp filament into the aperture diaphragm of the condenser. The condenser lens then projects an image of the filament to infinity. Each point on the filament gives rise to a parallel bundle of rays inclined at a certain angle to the axis of the microscope, as shown in the ray path. Points far from the axis give rise to steeply inclined bundles, whereas points near the axis results in a small inclination. These bundles are then illuminated on the plane of the specimen. However, the number of the bundles which can fall onto the plane of the specimen is determined by the condenser aperture diaphragm. Note that, if the illumination source covers a large angle, it can be considered as a spatially incoherent source. In contrast, if it covers a small angle, it is spatially coherent. Therefore, the closing or opening of the illuminating aperture diaphragm, or in other words choosing lower or greater numerical aperture, can define the spatial coherence feature of the microscope [96]. In order to provide a high resolution image, the aperture diaphragm is opened to the correct position with respect to the objective lens' numerical aperture. The numerical aperture of the condenser is typically set as equal to that of the objective lens.

In the optical characterization process of the FP filter arrays, creating a beam which is perpendicular to the filter surface is the priority which is dominant over the need of obtaining high resolution image. The transmission peak will widen and the center wavelength of the FP filter will shifts to smaller wavelengths if the angle of incident is large (chapter 2.2.2). Therefore, the condition that the numerical aperture of the condenser is equal as to that of the objective lens can be neglected.

In this work, to create a perpendicular beam which is projected on the filters being characterized, an optical microscope[3] is utilized. The condenser of the microscope is an aplanatic–chromatic condenser[4]. In order to assure the incident beam hits the sample surface perpendicularly, the condenser diaphragm of the microscope is adjusted until it is small enough to block the entire tilted incident light and allow only the collimated light passing through.

[3] Imager D1m Zeiss

[4] Achromatic-aplanatic universal condenser 0.9H D Ph DIC Carl Zeiss

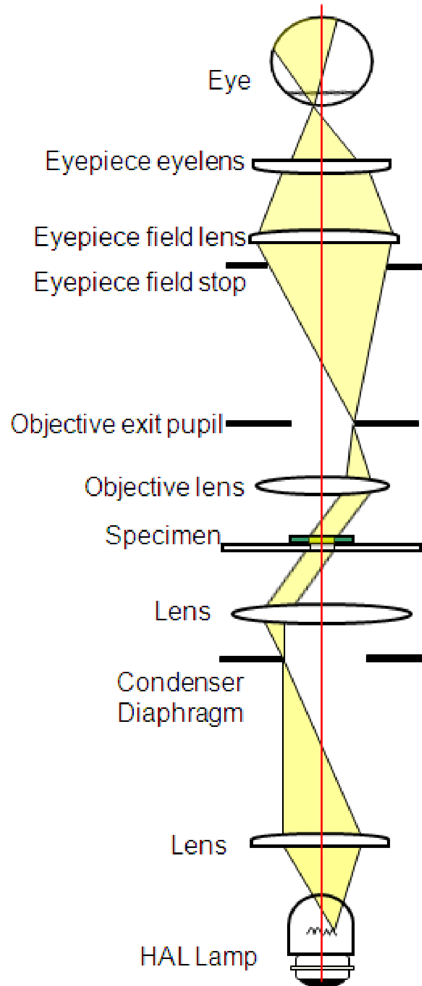

Fig. 2.25. Light part in Köhler illumination. The condenser creates a parallel beam. By adjusting the condenser diaphragm properly a well collimated beam which is perpendicular with respect to the filter layers is performed.

2.2.3 Methodology of spectral analysis and recording

Generally, the spectral analysis and recording methodology considered in the optical characterization procedure of the FP filter arrays requires a dispersal of polychromatic radiation into monochromatic bands. The most common way of producing such bands is with a device called a monochromator. Based on different constructions, monochromator falls into two main classes: prism monochromators and grating monochromators. However, grating monochromators generally dominate over prism monochromators due to the higher resolution and much weaker systematic errors arising e.g. temperature shifts as compared to prism monochromators [97]. Based on grating monochromators, different instruments are implemented and developed for spectral analysis and recording. Grating spectrometers and optical spectrum analyzers (OSA) based on grating monochromators are two kinds of these implemented instruments which are

commonly used in many optical characterization setups. In the following part, a brief review of the grating monochromator and the two alternative devices mentioned above are discussed in more detail.

2.2.3.1 Grating monochromator for spectral dispersion

A standard grating monochromator contains an entrance slit, two concave mirrors, a diffraction grating and an exit slit as illustrated in Fig. 2.26 below. An incident light is guided to the entrance slit. The width and height of the entrance slit define the amount of light available for use. The entrance slit is located at the effective focus of concave mirror 1, so that the incident light is reflected, and collimated onto a diffraction grating. The diffraction grating is used to separate the different wavelengths of light. The diffracted light is then refocused on the exit slit by concave mirror 2. In order to scan the whole spectrum the diffraction grating is rotated relatively to the incident beams. Due to this rotation, different bands of wavelengths are diffracted and projected toward the exit slit. The widths of the entrance and exit slit are variable and are used to determine the wavelength resolution of the instrument. The narrower the slits are, the better the resolution the monochromator can provide [97]. However, since the slit width is reduced, it will cut down the amount of light available for use. In practice, the widths of the entrance and exit slits are chosen by balancing the spectral resolution and the output light intensity (optical throughput). In any optical instrument, the formation of aberration gives rise to the blurring of the image when light propagates through optical elements. In a monochromator, aberrations are not introduced by the planar diffraction grating, however, mostly contributed by the use of spherical mirrors [97].

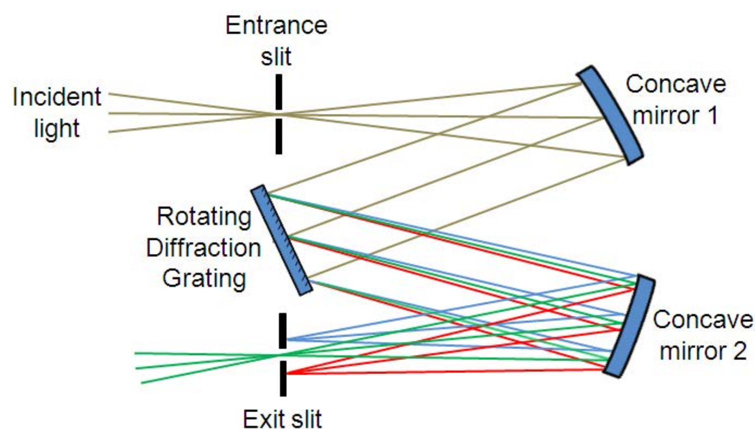

Fig. 2.26. Scheme of a grating monochromator consisting of a light source, an entrance slit, two concave mirrors, a diffraction grating and finally an exit slit. By rotating the diffraction grating relatively to the incident beam, the whole spectrum is scanned.

To determine the spectral analytic quality of a grating monochromator, there are two important parameters that are commonly used e.g. the resolving power $\Re$ and the wavelength resolution $\delta\lambda$. The resolving power $\Re$ of a monochromator describes the limit of its ability to separate adjacent spectral line of average wavelength λ, and it is given by the expression [98]:

$$\Re = \frac{\lambda}{\delta\lambda} = mN \qquad \textbf{2.27}$$

where m is the diffraction order and N is the number of grating lines illuminated by the radiation from the entrance slit. As expressed by (Eq. 2.27), the resolving power $\Re$ depends on the diffraction order and the number of grating lines. The resolving power of typical UV-visible monochromators ranges from 10^3 to 10^4. While the resolving power can be considered as a characteristic of the grating, the ability to resolve two wavelengths λ_1 and $\lambda_2 = \lambda_1 + \delta\lambda$ generally depends not only on the grating but also on the dimensions and locations of the entrance and exit slits, the aberrations in the images, and the magnification of the images. The minimum wavelength difference $\delta\lambda$ between two wavelengths that can be resolved is called the wavelength resolution. It has been proved that the wavelength resolution increases with an increase in number of grating lines N, and it also increases as the slit width decreases. The narrower the slits are, the better the resolution the monochromator can provide. However, since the slit width is reduced, it will cut down the amount of light available for use. In practice, the widths of the entrance and exit slits are chosen by balancing spectral resolution and output light intensity. Compared to the resolving power, the measurement of wavelength resolution is more relevant, since it takes into account the image effects of the system [97].

2.2.3.2 Grating spectrometer for spectral dispersion

The grating spectrometer is a type of instrument employing a grating monochromator commonly used to measure spectra, i.e. the light intensity profile over a specific range of wavelengths. In principle, the design structure of a grating spectrometer is nearly identical to that of the monochromator. It includes a mechanism to scan the light by a grating monochromator and to record the intensity by a detector [98]. In this case, the detector is located behind the exit slit.

In this work, for spectral analysis and recording of optical FP filter arrays in the visible range (from 400 to 900 nm), a grating spectrometer HR 2000 with wavelength resolution of 0.5 nm is utilized. The construction of the spectrometer is the same as described above. However, the spectrometer is designed so as its components (including the grating) are fixed. A narrow spectral band as a small part of the spectrum passes the rectangularly shaped area of the exit slit. Thus the left hand side slit border corresponds

to one border wavelength of that narrow spectral band and the right hand side slit border corresponds to the opposite wavelength border. The width of the exit slit is chosen as a compromise between intensity and resolution. It is narrow enough to enable the required resolution and wide enough to obtain an acceptable signal to noise ratio. In this case a single detector is sufficient. However, in order to use the multiplex advantage instead of the exit slit a relatively wide rectangular exit aperture is used in combination with a detector array, in most of the cases a CCD array, which is fitting precisely in its dimensions to the exit aperture. In this case the whole spectrum is recorded simultaneously. Each pixel of the CCD arrays detects a small band of the spectrum. Also in the second case $I(\lambda) \cdot \Delta\lambda$ is measured, where λ are the individual center wavelengths of the different pixels. The spectrum is then assembled from different pixels.

2.2.3.3 Optical spectrum analyzers for spectral dispersion based on grating monochromators

Optical spectrum analyzers (OSA) based on grating monochromators may contain either a single monochromator, a double monochromator, or a double path monochromator. Although OSAs based on single monochromator have relatively low cost, and high sensitivity, they have a small dynamic range[5]. In many spectroscopes with high wavelength resolution, thus, OSAs based on double monochromators are preferable due to their dynamic range improvement as compared with OSAs based on single monochromator. However OSAs based on double monochromators are comparably large and contain many drawbacks e.g. the reduction of spanning width due to the limitation of monochromator-monochromator tuning match; and degraded sensitivity which gives rise from the doubled losses in the monochromators [97]. Furthermore, they are required to be placed on a stable vibration isolated optical bench to avoid shock absorbance which results in a smaller sensitivity to vibration. These above mentioned drawbacks can be avoided by the use of OSAs based on double pass monochromator which provide the dynamic range advantage of the double monochromators and the sensitivity and size advantages of the single monochromators.

Figure 2.27 presents the optical configuration of a modern OSA based on double pass monochromator. The OSA uses a monochromator with only one diffraction grating and a return reflection component to diffract the light twice. As illustrated in the figure, the light beam coming from the incident connector is collimated by concave mirror 1, and dispersed by the grating. The dispersed light is collimated, and then guided to the return reflection component by concave mirror 2. Thereby, the first optical operation of the

[5] In General, the dynamic range is the ability of an analyzer to measure harmonically related signals and the interaction of two or more signals.

first monochromator is finished. The light reflected from the return reflection component is guided back to the concave mirror 2, and the grating. It is diffracted the second time, then becoming the incident beam on the concave mirror 1 and the photodiode. This defines the second optical operation equivalent to the function of the second monochromator.

In a modern double pass monochromator, the return reflection component is a critical part which can improve the spectral resolution and reduce the actual length of the monochromator. The return reflection component is structured with a combination of either planar mirrors and a slit; or planar mirrors, reflectors and a slit [99]. The slit of the reflective optical component is used to eliminate stray light. The function of the return reflection component is to reverse the dispersion direction[6] X of the incident light before leaving it (as demonstrated in the figure). This function assures that the grating diffracts the light at different dispersion direction. Due to this function, it increases the wavelength resolution of the OSAs.

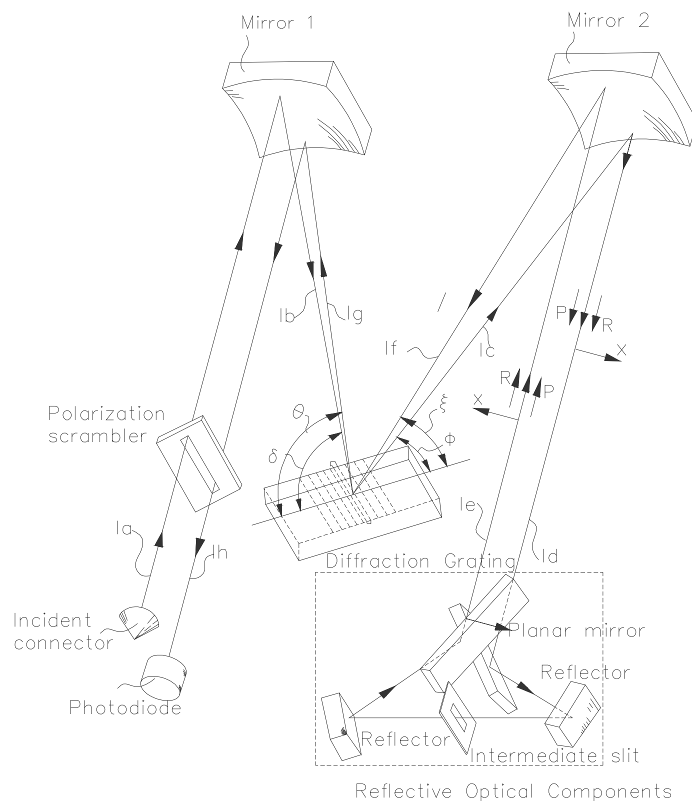

Fig. 2.27. Optical configuration of Double Path Monochromator which is equipped with a polarization scrambler, and a return reflection component. The return reflection component consists of two planar mirrors, two reflectors and an intermediate slit [99]. The direction of light propagation is illustrated as 1a – 1h.

[6] Direction of diffraction

Furthermore, the construction of the return reflection component ensures that incident light *1d* and the reflected light *1e* are parallel. Thus, the angles ξ and Φ, the angles θ and δ are identical. As a result, the incident light *1b* and diffracted light *1g* with respect to the grating are parallel. These behaviors do not change no matter what the angle of the grating is set. These features are advantages of the modern double pass monochromator based OSA compared with the conventional ones in which the angle of the light changed slightly in the first and the second optical operation with respect to the optical elements. Because of this, extra optical elements and extra mechanical alignment for maintaining high spectral resolution were required. Thus, the body of the conventional double pass monochromators became long and the aberrations increase [99]. By using the return reflection component, these problems were overcome which results in the elimination of optical aberration, and the reduction of the actual volume of the modern double pass monochromator.

In fact, the efficiency of the diffraction grating is dependent on the polarization of the incident light. As a result, the amplitude of the diffracted light beam may vary for input of light beams of constant amplitudes but different polarizations. This phenomenon results in an intensity uncertainty for measurements of polarized light. In order to eliminate the polarization dependence of the instrument, the OSA is developed with the use of a polarization scrambler to depolarize light. Here, the degree of polarization of the incident beam *1a* and outgoing *1h* can be reduced to zero by modulating the birefringence of the medium inside the polarization scrambler in which the light passes. As a result, the light beam is then rendered completely unpolarized [100]. Besides the use of a polarization scrambler, another approach to reduce the polarization sensitivity of an OSA is the use of a half wave plate which was first introduced by Wildnauer et al [101].

In this work, two double pass monochromator based OSAs namely the Yokogawa AQ 6375 and AQ 6373 are utilized for data recording [102]. The two OSAs effectively work in a range of 350 – 1200nm, and 1200 – 2400 nm respectively with high optical measurement capabilities. They provide a variable wavelength resolution of 0.02 nm to 10 nm, selected by the user. The polarization dependency is small, approximately 0.1 dB. These features significantly improve the reliability of the characterization process.

2.2.4 Basics of white light interferometry to visualize micromachined displacements

In the investigation of tuning behaviors, the displacement of FP filter's membrane is the focus of the mechanical investigations. The displacement measurements can be carried out by using a White Light Interferometry (WLI). White light interferometry (WLI) has been widely used as a fast, non contact optical technology for investigating the surface

geometry, and surface roughness of the mesa structures with high vertical resolution (within 0.1 nm) [103-105]. Surface roughness measurements can be also conducted by the use of scanning probe microscopy in which an image of the surface is obtained by mechanically scanning a physical probe through the whole sample. This would lead to a noticeable damage of the sample surface. Therefore, WLI is more adequate technique than scanning probe microscopy for characterizing the topography of the optical FP filter arrays.

In this work, a vertical scanning has been used to measure the vertical heights of the static filter arrays, as well as the displacement of the top DBR of a tunable FP filter in an array. The WLI includes a white light source, a Mirau interferometer, a magnification selector, and a camera which are shown in Fig. 2.28. The incoming light from the white light source is split by the beam splitter into two beams which are later coupled onto the sample and a reference mirror, respectively. The reflected beams recombine in the interferometer, undergoing constructive and destructive interference, and then generating a pattern of bright and dark interference fringes. This pattern is known as interferogram.

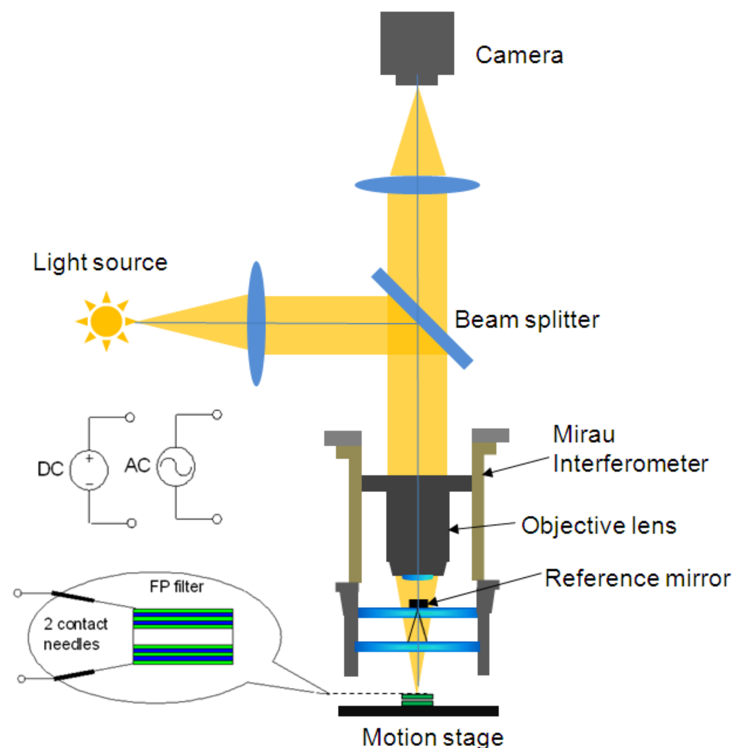

Fig. 2.28. Experimental setup of the white light interferometry for measuring surface roughness and mechanical displacement of the static and tunable filter arrays, respectively. To investigate the tuning behavior of the tunable filter during actuation, two kinds of voltage supply, DC and AC, are implemented with the WLI. Two needles are connected to the top and bottom electrodes of the filter.

During operation, the Mirau reference interferometer is vertically translated by a piezoelectric transducer. Thus, the distance between the objective lens and the sample is slightly varied while the distance between the objective lens and the reference mirror remains fixed. A phase shift generated during the vertical movement results in a new pattern of dark and bright fringes. The camera stores the intensity variation as a function of vertical scanning position. By processing the interferogram of each pixel in the camera, a 3D image of the sample surface can be generated.

In WLI, a white light source is implemented instead of a laser source. It is due to the fact that the while light source has a much smaller coherence length compared to a laser light source. Hence, the orders of the interference fringes are limited and able to be calculated.

The WLI in use in this work is a NewView 5000 scanning white-light interferometer from Zygo Corporation. The system has a maximal vertical step height of 100 μm, and a maximum vertical resolution of 0.1 nm. The field of view and the lateral resolution are determined by the objectives as well as the image zoom setting. The field of view is up to 3.525 mm × 2.65 mm by a 5 x Michelson objective, while the lateral resolution is down to 0.32 μm by a 50 x Mirau objective. The above-mentioned technical parameters can adapt all the requirements in lateral and vertical dimensions for surface roughness measurement of the 3D templates or 3D static filter structures, as well as displacement measurement of the tunable filter arrays.

In order to investigate the tuning behavior of the tunable filter during actuation, two kinds of voltage actuations, DC and AC, are implemented with the WLI. Two needles are placed on the motion stage and contacted to the top and bottom electrodes of the filter. The displacements of the filter membrane are recorded when different values of voltage and frequency are applied.

3 Previous optical setup designs to characterize optical properties of Fabry Pérot filter arrays

For the experimental investigation of the functionality of FP filter arrays, optical spectroscopy is attractive due to its high sensitivity, selectivity and nondestructive features. It is useful for both, a long-term and real time inspection without contaminating the sample. In fact, there are several options to design corresponding optical characterization systems. Concerning the sequence of the optical components there are two different options: (i) tunable monochromatic light source/ sample/ detector, (ii) broadband light source/ sample/ monochromator/ detector. Based on this sequence, different approaches have been developed to characterize the optical properties and tuning behaviors of the FP filter arrays. Firstly, three existing old characterization setups: a commercial Lambda 900 spectrophotometer, an optical bench setup, and a fiber based setup are introduced and described. The advantages and disadvantages of the setups occurring during characterizing optical and tuning properties of the FP filter arrays of each setup are also discussed in detail. Afterwards, the chapter describes the construction details and the working principle of a new characterization setup: the compact microscope spectrometer setup which by far overcomes the current drawbacks of the previous setups. A precise alignment and calibration of the compact microscope spectrometer setup which are the critical issues to obtain the reliable results is also presented in this chapter.

3.1 Lamdba 900 spectrophotometer

The Lambda 900 UV/Visible/NIR spectrophotometer[7] is a commercial system commonly used to characterize the transmission and absorption spectra of samples in the UV, visible and NIR spectral regions. Concerning to the sequence of optical components, the structure of the Lambda 900 spectrophotometer is considered as tunable monochromatic light source/ sample/ detector. The functionality of the spectrophotometer is similar to that of a standard spectrometer. It contains two radiation sources, a double grating monochromator and detectors. Two radiation sources, a deuterium lamp and a halogen lamp, are used to cover the spectral working range of the spectrophotometer. A combination of the two lamps with a double monochromator presents as a wide spectral range tunable monochromatic light source which typically works in the range of 300 – 3000 nm. Within the double monochromator, the light is collimated by several mirrors. This feature ensures that the monochromatic light coming out from the source is well

[7] Lambda 900 UV/Visible/NIR spectrophotometer, Perkin Elmer

collimated to illuminate the sample being measured. The light passing through the sample is guided by a system of mirrors to the detectors. The maximum resolution of the device is 0.5 nm [106].

The schematic diagram of the system is illustrated in Fig. 3.1. In general, the basic operation of the system is to split the beam into two beams of equal intensity: the reference beam and the sample beam. Firstly, two identical glass substrates which are employed to deposit the filter on top of them are introduced into the beams. The subsequent measurements under this situation provide a “spectral reference” which is called “baseline”. After recording the baseline, the desired transmission measurement of the samples can be done by in our case simply replacing one of glass substrate by a FP filter structure. Then a division of two spectra: one from the transmitted beam through the sample and the other from the reference beam is recorded and denoted as transmission spectrum of the characterized filter.

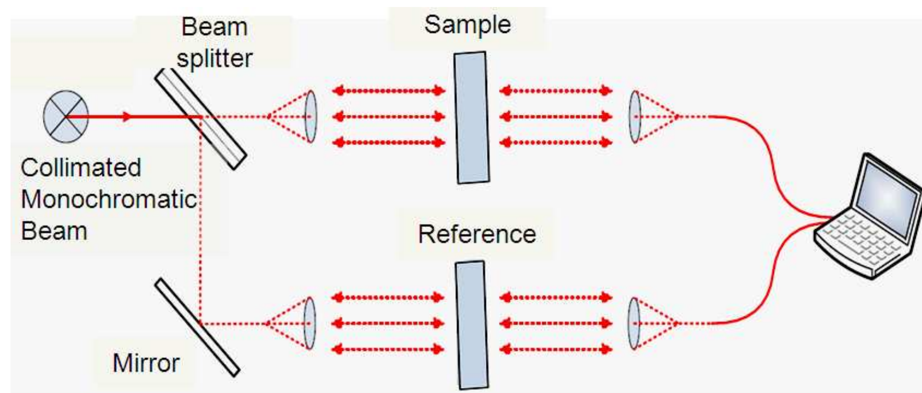

Fig. 3.1. Schematic setup of the Lambda 900 spectrophotometer [107].

As observed from the schematic setup, both transmission curves are recorded in parallel. The benefit of monitoring both beams during this measurement helps to eliminate any intensity fluctuations of the light source. The main advantages of the Lambda spectrophotometer 900 are (i) characterizing optical properties of FP filter in a wide spectral working range from the UV to the NIR and (ii) elimination of any intensity fluctuations of the light source by monitoring both beams simultaneously. However, these advantages can be only applied for unstructured FP filter which are laterally large enough. For the filters with a lateral structure design in the µm rang, the device is incapabe to characterize the optical properties without overlapping it with the properties of the laterally neighboring filters. It is unable to monitor the details of surface structures of the filter, and thus could not identify which area in the sample is measured. Furthermore, the impossibility to operate in reflected measurement also addresses other disadvantages of the spectrophotometer Lambda 900.

3.2 Optical bench setup

Concerning the sequence of tunable monochromatic light source/ sample/ detector, the optical bench setup[8] is another advanced approach which can overcome the current drawback of the spectrophotometer Lambda 900 in characterizing micro structured FP filter. Similarly to the previous case, the tunable monochromator light source is implemented by the combination of a halogen lamp and a monochromator. To measure the spectral transmission of the filter arrays, the wavelength is scanned over the spectral region where the FP filter arrays were designed to function. In this case, the smallest scanning step is 0.2 nm and the wavelength resolution is in the range of 0.5 to 1 nm. Figure 3.2 presents the schematic diagram of the optical bench setup.

As seen in the figure, the monochromatic light is collimated with lenses to illuminate the filter arrays. On both sides of the arrays, two pinholes are utilized. They limit the angles of the incident beams until they are small enough not to degrade the filter spectral quality. Only a very narrow band of wavelengths can pass monochromator. This band is spectrally tunable and is used to characterize the spectral transmission behavior of the FP filters. The transmitted light is captured by an objective lens which then focuses and directs the light on to a CCD camera. The CCD camera is assigned as a detector which measures the amount of light that passing the filter. Here, a group of pixels with the size of 7.4 x 7.4 µm, each, corresponds to a single filter in an array. After scanning thoroughly the total spectral range, a curve of the filter transmission intensity is obtained by combining all the intensities recorded by the pixels. Finally, the transmission spectrum of the characterized filter is defined from a division of two spectra: one from the filter and the other only from the halogen lamp as a reference. The monitoring of the filter image is conducted by an objective lens which magnifies and projects the sample surface's image on the CCD camera with qualified image resolution. Thus, it is well defined which area of the sample is measured.

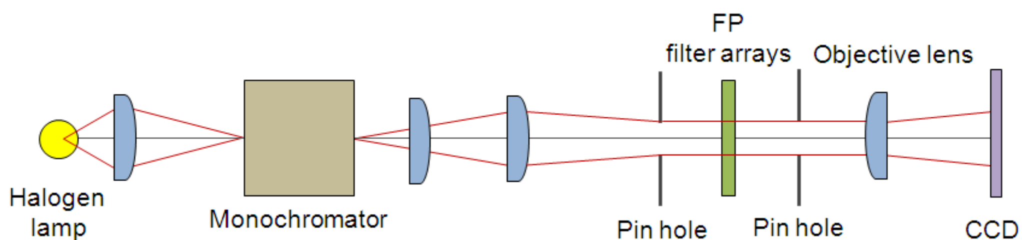

Fig. 3.2. Schematic diagram of the optical bench setup.

[8] The optical bench setup is implemented at Opsolution Nanophotonics GmbH, Kassel, Germany.

The main advantage of this setup is to characterize FP filter with micro structures as compared to the spectrophotometer Lambda 900. Moreover, the setup alternatively also provides a possibility of creating a high uniform large area of illumination. However, the setup presents some disadvantages. For instance: the two transmission spectra from the lamp and from the sample are not recorded in parallel. Therefore, any intensity fluctuation of the light source during the setup operation may cause adverse effects on the quality of the final transmission spectra. Furthermore, due to the horizontal orientation of the setup, it reveals some difficulties to accurately position the tunable filter. Other current drawbacks of the optical bench setup are (i) poor resolution spectra as a result of light divergence when light propagates through the setup and (ii) the impossibility to operate in reflection measurement.

3.3 The fiber based setup

The fiber based setup is another approach to characterize the optical properties and tuning behaviors of FP filter arrays [42, 46]. In contrast to the two previous ones, the fiber based setup is developed according to the sequence of: broadband light source/ sample/ monochromator/ detector. The setup is optimized for NIR wavelengths and is vertically oriented which is beneficial for actuation of tunable filter. The schematic of the measurement apparatus is depicted in Fig. 3.3. In this design, a broadband LED[9] working in the NIR spectral range is used as a light source. In this case always the whole spectrum of the light source illuminates the filter arrays. Light is guided from the LED by a single mode fiber to the 50:50 3dB coupler which divides it into two separated beams of identical intensity and spectrum. One beam travels to the matched end, where it is extinguished. The second beam is coupled into another single mode fiber and guided to the sample that is located very close to the tip of the fiber.

In order to characterize the properties of micro structured FP filter, the fiber based setup makes advantage of the close proximity of the fiber with the sample, as it shown in the Fig. 3.3. A single mode fiber having a fiber core of 9 µm which is approximately lateral the size of the characterized filter is placed closely to the filter membrane. This feature ensures that the incident light only illuminates one filter, and thus, each FP filter in an array is characterized separately. The wavelengths transmitted or reflected through the filter are then collected and analyzed by an OSA. In order to characterize other filters, the sample stage is translated in the horizontal direction (xy direction) to define the new positions to be characterized.

[9] Agilent 83437A

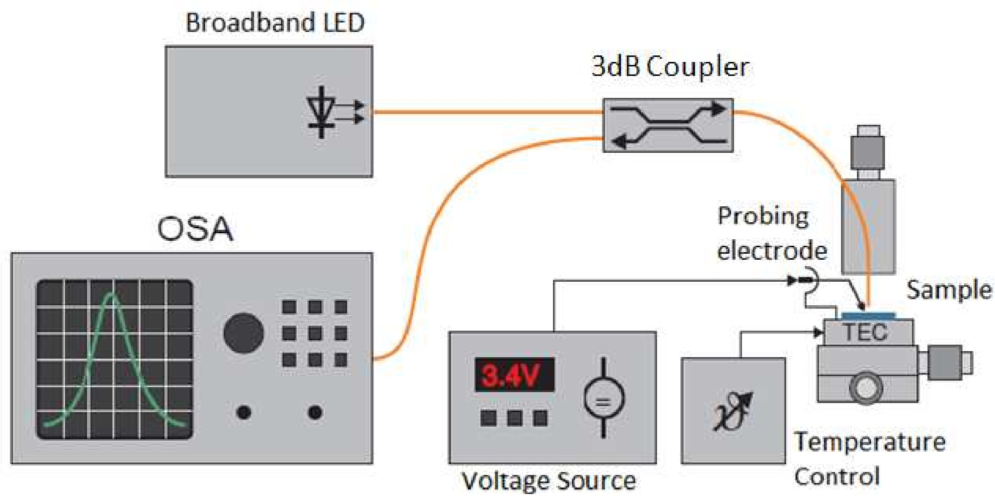

Fig. 3.3. Schematic diagram of the fiber based setup for reflection measurement [46].

Besides the possibility of characterizing each FP filter separately, the fiber based setup offers an opportunity of conducting both transmission and reflection measurements. For reflection measurements, the reflected light from the sample is coupled back to the same fiber and propagates through the coupler into the OSA, where the spectral properties of the reflected light are analyzed. For transmission measurements, the transmitted light is recorded by a detector which is located underneath the sample stage. The spectral properties of the transmitted light are analyzed by the OSA afterwards.

The system is technically noteworthy to perform the tuning effect of tunable filters by applying a voltage. However, the setup itself presents several limiting factors that are coming from the optical losses during operation and the alignment between the fiber and the sample. For reflection measurement, the light has to pass twice the coupler which means that finally only 25 % of the light from the source is delivered to the OSA. Other disadvantages of this method are (i) the time consuming positioning of the fiber tip into the proximity of the filter surface in vertical and lateral directions and (ii) the ease of damage to the filters, since the filter tip is very close to the top DBR mirror. As a consequence of accidental mechanical vibrations on the optical table, the fiber can easily come in contact with the filter surface during the alignment and measurement procedure and damage the structures. Moreover, the cladding surrounding the fiber core which has diameter of 125 µm also makes it troublesome to align the fiber core with the filter membrane since the total fiber covers a very large area of the filter surface.

Obviously, each of the previously mentioned setups for characterization optical properties and tuning behaviors of FP filter arrays has some advantages and disadvantages. The major disadvantages of these setups are the above mentioned limitations in characterizing optical properties and tuning behaviors of the FP filter in both reflection and transmission measurement with high spectral quality. The fiber based setup which is

able to operate in both transmission and reflection measurement, however, it reveals a difficulty in aligning the fiber tip without damaging the FP structure.

In order to overcome the current drawbacks of these setups, new characterization setups which can effectively work in both transmission and reflection measurement with high spectral quality, short inspection time while not contaminating the micro structure of the FP filter are highly requested. In this work, two characterization setups: the compact microscope spectrometer and the free beam broad band confocal setup have been developed and will be introduced in the following parts.

3.4 Compact microscope spectrometer setup

This compact microscope spectrometer setup was installed within this thesis. The other setups mentioned in this chapter were state of the art when this thesis was started.

In this section, the compact microscope spectrometer setup which can by far overcome the drawbacks of the previous setups is introduced. The setup is based on a microscope and a spectrometer or optical spectrum analyzer (OSA). Concerning the sequence of the optical components the setup is arranged as: broad band light source/ sample/ monochromator/ detector. In the setup, a Halogen lamp (HAL) is utilized as a broad band light source; a grating spectrometer or an OSA plays the role as a combination of a monochromator and a detector. The setup can provide high spectral and spatial accuracy, high measurement speed, ability of measuring microstructure dimensions, and capability of actuating the tunable FP filter arrays. Furthermore, it is easy to use and possible to replace optical elements inside the system to meet further requirements. In the following part, the construction details, the working principle and the calibration procedure of the compact microscope spectrometer meter setup are presented.

3.4.1 Construction details of the compact microscope spectrometer setup

As described in chapter 2.2, in a setup used for optical spectroscopy, there are four main parts which are needed for conducting experimental measurements such as (i) an illumination system, (ii) a collimation and magnification system, (iii) a sample stage and finally (iv) a data recording and analysis system. In the case of the compact microscope spectrometer setup, the setup utilizes two halogen lamps as broad band light sources. The collimation and magnification system and sample stage are implemented by an optical microscope. A grating spectrometer or an OSA is assigned as the data recording and analysis system. The construction detail of the setup is illustrated in Fig. 3.4 below.

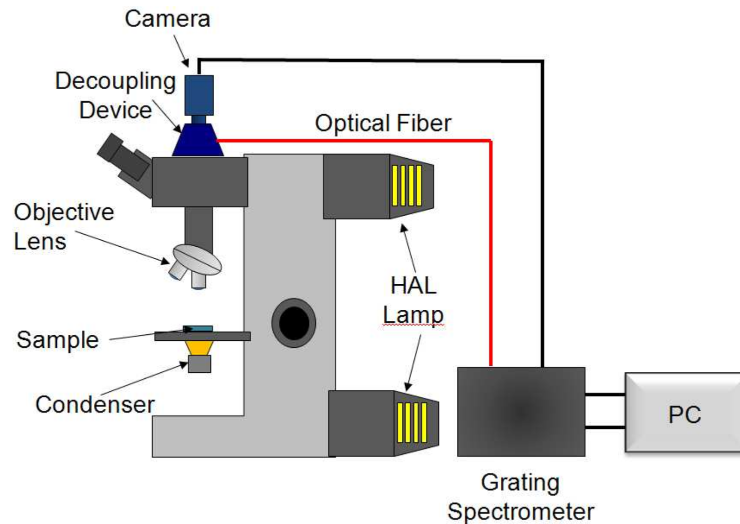

Fig. 3.4. Scheme of the experimental setup of the compact microscope spectrometer for the measurement of transmission and reflection spectra.

3.4.1.1 The illumination system of the setup

Due to the wide range applications of our FP filter arrays (from the visible to NIR range), in this setup, two HALs[10] are chosen for the illumination system. Details about the HAL lamps are described in chapter 2.2.1.1. Here, one lamp is assigned for reflection measurement; the other is for transmission measurement.

3.4.1.2 The collimation and magnification system and the sample stage of the setup

In order to obtain high spectral accuracy, one thing which must be carefully considered when designing a setup to characterize optical properties of FP filter arrays is the incident angle of the illumination beam. The transmission peak will widen and the center wavelength of the FP filter will shifts to smaller wavelengths if the angle of incident is large (chapter 2.2.2). In order to create a perpendicular light beam with respect to the filter surface and magnify the sample image, the setup is developed with the use of an optical microscope[11]. The microscope consists of an aplanatic–chromatic condenser[12]. The function to create a parallel beam which is perpendicular to filter surface is obtained by adjusting the condenser diaphragm until it is small enough to block the entire tilted incident light and allow only the collimated light passing through (as discussed in chapter 2.2.2.2).

[10] HALs 100 Carl Zeiss

[11] Imager D1m Zeiss

[12] Achromatic-aplanatic universal condenser 0.9H D Ph DIC Carl Zeiss

An objective lens is an important part of the collimation and magnification system. It is utilized to gather light from the sample being observed and focus the light rays to produce a real image. The microscope contains three EC Epiplan Neofluar objective lenses (2.5 x/0.06[13], 10 x/0.25[14] and 50 x/0.8[15]) which can considerably constrain optical aberration phenomena. The high numerical apertures (NAs) of the lenses result in high resolution and bright image with rich contrast of the sample being measured. The objective lenses are color corrected from 350 to 1200 nm with transmission efficiency of above 80 % in the VIS range, and above 40 % in the NIR range. The high transmittance of the objective lens assures the main optical power of transmitted or reflected light coming from the characterized filter is guided to data recording and analysis system. Hence, it significantly reduces losses during the operation of the setup.

In any characterization setup, the sample stage is always an important part which carries the filter arrays, and scanning the whole sample. Due to the fact that each FP filter in an array has a slight difference in vertical dimension. Thus, to assure the sample surfaces are always laid at the focal point of the objectives lenses, the sample stage is required to precisely translate in vertical direction (z direction). As described in the previous parts, each sample being measured may contain a thousand of individual FP filters, and each filter requires a systematic optical characterization. Therefore, to investigate the optical properties of the whole sample, the sample stage is assigned to accurately move in the lateral direction (xy direction). In this setup, accurate translations of the sample stage in xyz direction is conducted by using a motorized translation stage[16] with the travel range of 100 x 80 mm in lateral direction, and the smallest step size of 0.1 µm. These features lead to a fast and precise lateral positioning thus, different positions that address different individual filters for characterization are quickly reached. This function significantly minimizes the total measurement time, thus enables immediate feedback to the technological fabrication. When the calibration and alignment process of the setup is accomplished, the measurement time for each filter takes around ten to twenty seconds.

During the measurement, in order to capture the picture of the structure, as well as to define the exact positions of the filter in an array, the setup imaging system is equipped with a CCD camera[17]. In fact, the image of the HAL lamp is set to infinity; hence, it is not visible in the detector screen of the camera. Therefore, only the image from the sample surface is obtained and captured by the camera.

---

[13] Epiplan-Neofluar 2.5X/0,075 HD DIC M27 Zeiss

[14] Epiplan-Neofluar 10X/0,25 HD DIC M27 Zeiss

[15] Epiplan-Neofluar 50X/0,8 HD DIC M27 Zeiss

[16] Scan 100 x 80-1 mm Märzhäuser Wetzlar

[17] DFK 41AF02 Imaging source

3.4.1.3 The data recording and analysis system of the setup

The data recording system consists of a coupling device[18] together with a grating spectrometer or an OSA based on double pass monochromator. The coupling device is used to select and couple the transmitted or reflected light from the FP filter being measured into an optical fiber. The received signal is then analyzed by the spectrometer or the OSA. The construction detail of the coupling device is depicted in Fig. 3.5. The rectangular adjustable diaphragm has the minimum and maximum width and height of 0.1 mm and 7 mm respectively. By adjusting the diaphragm, users can control the amount of light to pass and then reach to a single lens. This amount of light corresponds to the size of inspected area in an array. The single lens having a focal length of 10 mm is assigned to focus and couple the light into the optical fiber.

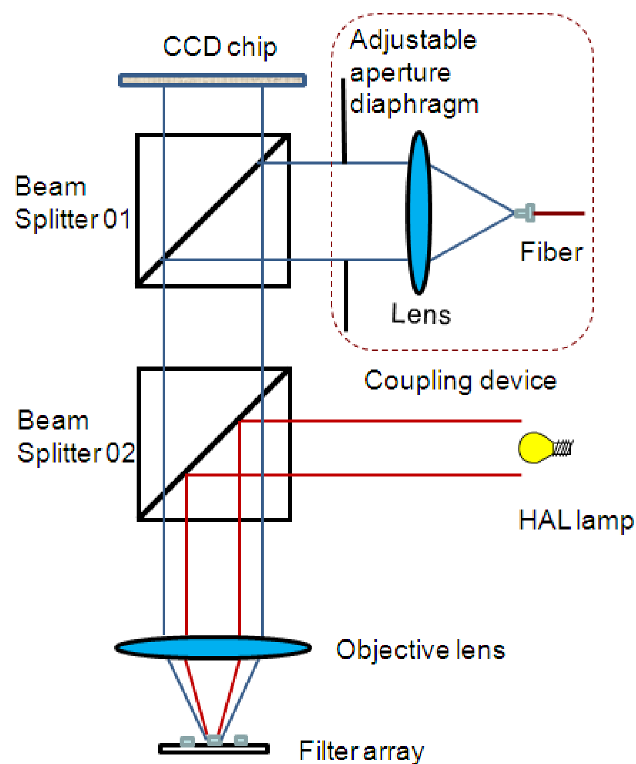

Fig. 3.5. Scheme of the setup for reflection measurement.

Two main issues that are needed to be concerned in coupling light into an optical fiber are the radius of the fiber and its numerical aperture. This is inferred from the fact that light is collected only from an area of the optical fiber radius; and the maximum angle coupled into the fiber is restricted by its numerical aperture. In this setup, the coupling procedure involves in focusing the light from a spatially incoherent source, the HAL

[18] J&M Mic – out 3 for microscopy

lamp, onto a fiber core. This leads to significant losses of optical power during coupling. Therefore, to achieve maximum coupling efficiency, a multimode fiber with a very large core diameter and a largest available numerical aperture according to the core diameter is required. Furthermore, using multimode fiber also provides the advantage of less sensitivity to misalignment during the operation of the setup. In order to fulfill these requirements, a multimode fiber[19] has a diameter of 600 µm and NA of 0.22 is utilized to coupling the light and sent it to the grating spectrometer or the OSA.

The data recording system is accomplished with the use of a grating spectrometer or an OSA based on double pass monochromator. The utilized grating spectrometer[20] provides a spectral resolution of 0.5 nm and a working range of 400 to 900 nm which is adequate for visible range application of the FP filter arrays. For broader spectral range operation and more precise characterization supply, the use of an OSA is necessary. In this setup, the OSA based on double pass monochromator [21] which is well suited for a broad range operation from 350 nm to 1200 nm is chosen. Due to its ability of offering high speed, accurate analysis and variable wavelength resolutions from 0.02 nm to 10 nm, the OSA can efficiently organize in many different characterization conditions in short inspected time, thus, providing very fast feed back to fabrication processes.

During operation, the compact microscope spectrometer setup can function in such a way that the processes of measuring and imaging the filter being investigated can be carried out at the same time. This can be done by the utilization of a beam splitter which is indicated in Fig. 3.5 as *beam splitter 01*. In the operating wavelength range, the beam splitter can reflect 80 % of the entire optical power while transmit only 20 %. Thus, the main optical power of the transmitted or reflected light coming from the characterized filter is delivered to the data recording system. Only a small amount of the entire optical power is delivered to the imaging system for capturing the image of the filter array, this eliminates glare in the forming of image during the illumination of the incandescent HAL lamp.

In order to perform reflection measurement, the setup is developed with the use of another beam splitter defined as *beam splitter 02* in Fig. 3.5. The division ratio of the beam splitter is 35:65 i.e 65 % of the entire power is reflected whereas only 35 % is transmitted. Therefore, the main optical power is remained to illuminate the filter arrays.

[19] AS 600/660 IRA, J&M

[20] HR 2000 Ocean Optics

[21] Yokogawa AQ 6373

For characterizing micromachined tunable filter arrays, two contact needles[22] are utilized for electrostatic actuation. These needles are connected to the top and bottom electrodes and securely fixed on the sample translation stage (see Fig. 3.6). An electrical power supply delivering variable voltages for filter tuning is applied. In this study, two kinds of power supply, AC and DC are applied for further investigations of the filter tuning behaviors.

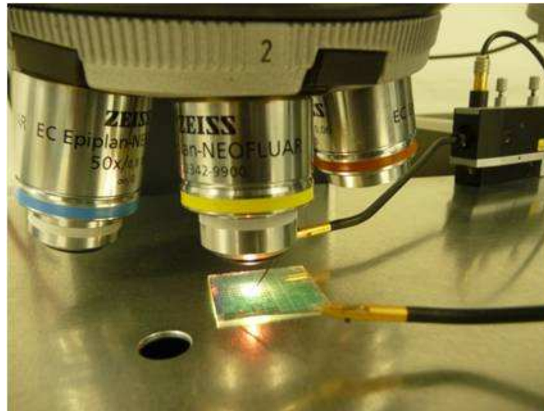

Fig. 3.6. Two needles for electrostatic actuation in the microscope spectrometer setup.

For further purposes; e.g. measurements in the UV, NIR or IR range, the HAL, objective lenses and other optical elements can be replaced to fulfill other new requirements.

3.4.2 Working principle of the compact microscope spectrometer setup

In this part, the working principle of the compact microscope grating spectrometer setup for investigating the optical properties and tuning behaviors of the static and tunable FP filter arrays is introduced. The properties are measured in both reflection and transmission. To perform an accurate measurement, it is demanded to precisely calibrate the whole setup every time a new lateral geometry of the characterized FP filter is requested. Hence, the procedures of calibrating the setup, aligning and measuring samples are later described in detail.

3.4.2.1 Working principle of the setup in reflection measurement

A scheme of primary parts of the system while measuring in reflection measurement is displayed in Fig. 3.5. The light from the upper lamp is directed onto *beam splitter 02*, which divides the light into two beams. One fraction strikes vertically to the objective lens which illuminates the sample surface as a field of a few millimeters in diameter. Some light passes through the filters; some reflects backward. The reflected light is col-

[22] MicroTech

lected by the objective lens, passed through *beam splitter 02* one more time and then split into two parts at the upper *beam splitter 01*. The transmitted part is guided to the CCD camera to capture the top view of the filter structure. The reflected part illuminates an adjustable rectangular diameter diaphragm and finally it is coupled into an optical fiber by the coupling device. The reflected spectrum can now be analyzed by the grating spectrometer or the OSA. To perform a reference spectrum, a 100 % reflected mirror (a full mirror) is applied. The full mirror is actually a substrate coated with Aluminum which has high reflectivity in the visible range and NIR. The broad band spectrum from the HAL lamp is reflected 100 % by the full mirror which is then regarded as a reference spectrum.

In an ideal case, the absorbance of light in the optical elements and the full mirror is negligible, and the coupling efficiency into the multimode fiber is considered maximum. The spectrometer or OSA just receives 18 % of the light source's optical power due to the losses when light propagates through *beam splitter 02* twice, then strikes *beam splitter 01* before coupling into the fiber.

3.4.2.2 Working principle of the setup in transmission measurement

In the case of transmission measurement, the light beam is provided by the lower HAL lamp, which illuminates the system from underneath. A mirror reflects the beam upward and leads it to the condenser diaphragm. After passing through the filter arrays, transmitted or diffracted light is gathered by the objective lens and directed to *beam splitter 01*. In this case, *beam splitter 02* which is only necessarily requested in reflection measurement is removed to eliminate looses. The remained *beam splitter 01* splits the beam into two parts. One fraction which carries only 20 % of the entire optical power strikes the CCD camera vertically to display the top view image of the filter structure. The other fraction containing the majority of the entire optical power of about 80 % is reflected to the rectangular adjustable aperture diaphragm. Afterwards, it is focused by a single lens and coupled into the optical fiber. Comparing to the case of reflection measurement, only *beam splitter 01* is assigned in use for transmission configuration, this gives rise to the considerable reduction of losses when light travels inside the setup. The schematic of the system for transmission measurement is depicted in Fig. 3.7.

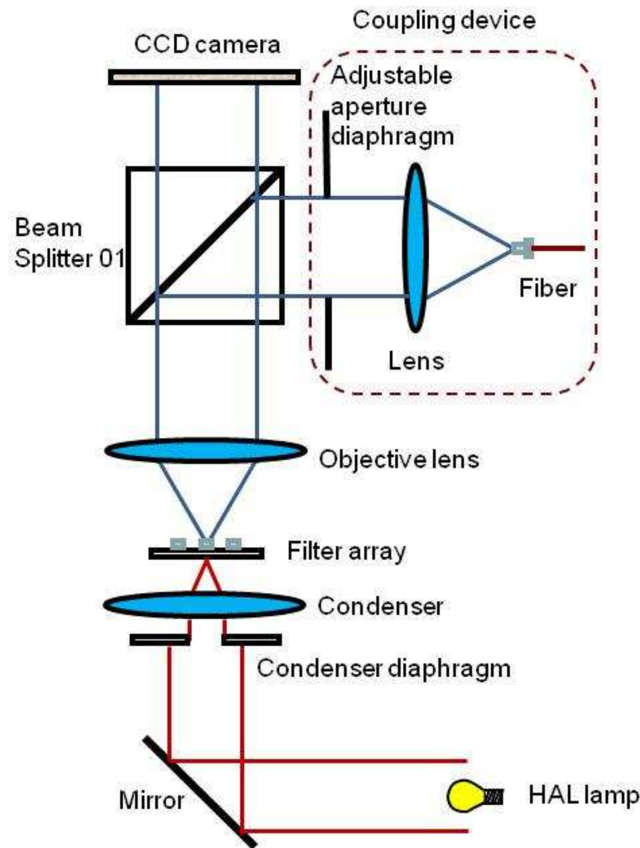

Fig. 3.7. Scheme of the sytem for transmission measurement.

As proposed in the previous part, the compact microscope spectrometer is assigned to characterize the filter membrane with the lateral size of ten up to hundred micrometers. This leads to a challenge of precisely detecting the signal from such a small structure. In order to solve this problem, the setup presents a function of spacially selecting filter being measured. The spacial selective function of the setup utilizing in both transmission and reflection measurement is illustrated in Fig. 3.8. As mentioned before, light is focused on the filter arrays as a circle of a few millimeters in diameter. That means the light spot covers a certain area in the arrays. Due to the objective lens and the beam splitter, all the illuminated filters in that area can create magnified images on the image plane of the aperture diaphragm. Light from only one filter, placed at position AB, whose image is projected to the position A′B′ on the open part of the adjustable aperture diaphragm, can be coupled into the fiber. Light originating from other filters which are not measured is suppressed. This feature assures the characterization and data recording processes are applied on only one FP filter in each measurement. By adjusting the aperture diameter of the rectangular diaphragm to fit with different image sizes, the entire or just a small part of the considered filters with alternative lateral dimensions can be measured.

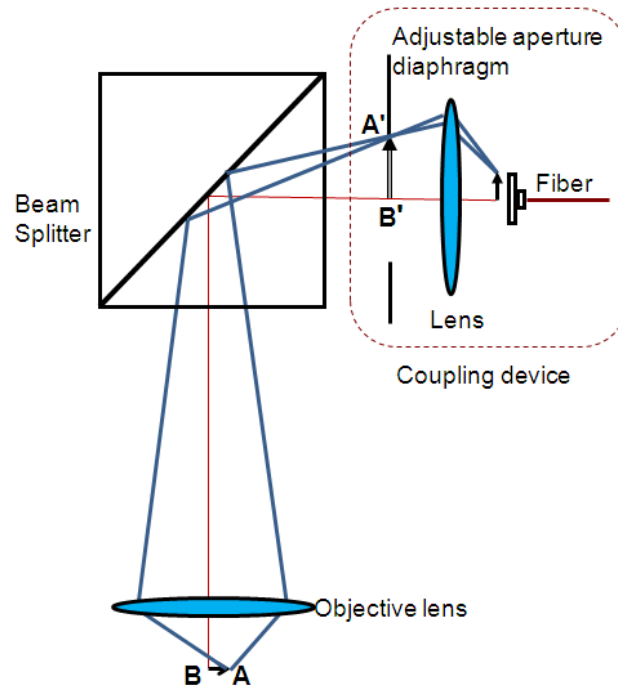

Fig. 3.8. Ray paths in the compact microscope grating spectrometer setup. By properly adjusting the adjustable aperture diaphragm, only the light coming out from one filter located at position AB can be coupled into the fiber. The others are neglected.

3.4.3 General spectral features in calibrating setups and correcting spectra

In measurement setups all optical components reveal more or less pronounced wavelength dependences:

- The applied light sources (lamps, lasers, LEDs) emit strongly different intensity spectra.

- Optical lenses, prisms and fibers reveal different spectral absorption spectra.

- Mirrors have different spectral reflectance characteristics, depending on materials and geometrical data.

- Grating spectrometers have different spectral diffraction efficiencies.

- Detectors have a different spectral sensitivity.

Therefore, all the components participate in the measurement process with a different characteristic dependence on wavelength. By all the components of the measurement setup, the real spectrum (intensity as a function of wavelength) is sequentially modified by all these optical components. Therefore, the measured spectrum has to be corrected to obtain the real spectrum. This is done by the *spectral calibration profile* which is different and characteristic for each setup.

Correcting reflectance spectra: we have to use the identical total setup and record both, the reflectance spectrum of the sample and the reflectance spectrum of an ideal mirror (having 100% reflectivity over the whole wavelength range considered). Further correction profiles have to be applied if the mirror is not ideal. Since no reflectance measurements are shown in this thesis the mathematical procedure of correction using the calibration profile is not shown in detail.

Correcting transmission spectra: is much simpler. Again we have to use the identical total setup and record both, the transmission spectrum of the sample including the substrate and the transmission spectrum of the isolated pure substrate (reference spectrum) over the whole wavelength range considered. Roughly spoken, the correction is done by dividing the reference spectrum by the reflectance spectrum related to the sample. For each setup the calibration and correction procedure is like this, but details are different. Therefore, the calibration and correction is explained in detail during the presentation of each individual setup.

3.4.4 The calibration procedure of the setup

As described previously, adjusting the diameter of the rectangular diaphragm is a critical step to define and configure the dimension of inspected area. In order to precisely adjust the diaphragm, an additional calibration process is required in this setup. The calibration procedure is described in detail below. The calibration procedure is divided into two main steps.

Firstly, a filter with a predefined lateral membrane is inserted into the light part of the setup. The filter is oriented so that the membrane centre is placed in the optical axis of the setup. The objective lens together with the beam splitters project a real image of the magnified filter membrane A_1B_1 onto the image plane of the camera which is then displayed on a computer screen. At the same time, a magnified image A_2B_2 having the exact same size as A_1B_1 is created in the image plane of the rectangular adjustable aperture diaphragm. The interested lateral dimension of the magnified image which is depicted as a white square on the computer screen is defined in Fig. 3.9 (b). This dimension is stored, and acts as a reference which later will help to properly adjust the diaphragm.

Secondly, the filter is replaced by the full mirror (Aluminum coated mirror). A tungsten lamp[23] connecting to the multimode optical fiber functions as an external light source for calibration. Light emitted from the tungsten lamp is projected on the adjustable diaphragm, propagating through its open part, reaching the beam splitter, objective lens,

[23] Tungsten halogen lamp LS-1 Ocean Optics

finally focusing on the mirror surface as a small light spot. The light spot represents the miniaturized image of the open part of the adjustable diaphragm. Due to the highly reflective mirror, the beam is then reflected backward to the objective lens and beam splitter. Again, a magnified image of the light spot on the full mirror is produced and captured by the objective lens and beam splitter, projected on the camera. The size of the magnified light spot image displayed on the camera and the size of the open part in the adjustable diaphragm are identical. The light spot image is displayed on the same screen together with the white square which was predefined as the magnified dimension of the filter membrane. By adjusting the rectangular aperture diaphragm, users can localize and frame the light spot until it lies within the white square, and their lateral dimensions are perfectly matched (Fig. 3.9 (c)).

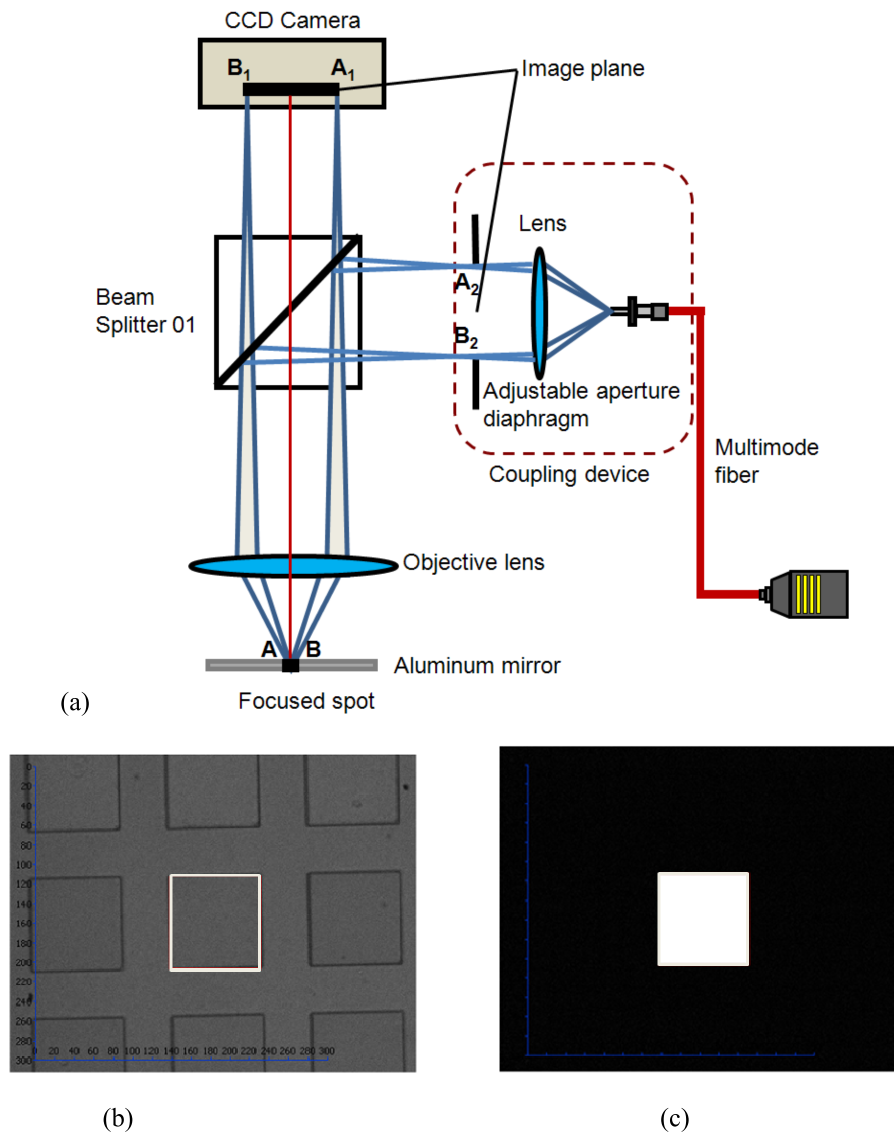

Fig. 3.9. (a) Ray paths of the setup for calibration process, (b) defining the lateral dimension of the characterized filter, (c) localizing and framing the outgoing light in to that white square.

For each measurement the spectral characteristic of the HAL lamp is initially measured without the samples to obtain the spectral intensity profile as a reference spectrum of the lamp $L_i(\lambda)$. For reflection characterization, the reference spectrum of the lamp $L_R(\lambda)$ is measured using the full mirror reflecting 100 % within the spectral range of interest. For transmission characterization the reference spectrum of the lamp $L_T(\lambda)$ is measured using a substrate without filters, identical in material and thickness to those used for the FP filter arrays.

In case the grating spectrometer is utilized, the spectral calibration of the grating spectrometer is done with a spectrally narrow laser line, which is precisely known in wavelength. Firstly, a spectrum is measured without any optical excitation (dark spectrum $D_i(\lambda)$). Afterwards, all the desired reflection spectra $S_R(\lambda)$ or transmission spectra $S_T(\lambda)$ of the FP filter arrays are captured and numerically corrected using Eq. 3.1. This can compensate for all the thermal drift in the detector of the spectrometer and the aging of the lamps.

$$T(\lambda) = \frac{S_T(\lambda) - D_T(\lambda)}{L_T(\lambda) - D_T(\lambda)} \times 100\%$$

$$R(\lambda) = \frac{S_R(\lambda) - D_R(\lambda)}{L_R(\lambda) - D_R(\lambda)} \times 100\% \qquad \textbf{3.1}$$

In case the OSA is implemented, the transmission spectrum $T(\lambda)$ is obtained by dividing the spectrum measured with the sample $S_T(\lambda)$ by the reference spectrum $L_T(\lambda)$. With other words the measured data are subtracted logarithmically from the reference spectrum $L_T(\lambda)$. These processes reveal the calibration of the T, R and λ axis. The spectra $R(\lambda)$ and $T(\lambda)$ are in percentage units (%).

4 Geometric and compositional details of the samples studied

In this chapter, the geometric and compositional details of the samples including static and tunable FP filters which are studied in the following chapters are presented.

4.1 Geometric and compositional details of unstructured Fabry Pérot filters

An unstructured FP filters consists of a top DBR, a bottom DBR and a polymer cavity. Details about materials for DBR, cavity, number of DBR periods and the predefined central wavelengths of the unstructured FP filters characterized in this work are listed in table 1.

Table 1. Geometrical parameters of the characterized unstructured FP filters.

Physical parameters for filter device	UF1	UF2
Cavity material	mr-UVcur06	mr-UVcur21
DBR materials	Si_3N_4/SiO_2	Si_3N_4/SiO_2
DBRs periods	9.5	9.5
Central wavelength	650 nm	650 nm

4.2 Geometric and compositional details of static Fabry Pérot filters

Geometric and compositional details of three static FP filter arrays and one static FP filter in an array are demonstrated in table 2. The filters are structured by 3D NanoImprint technology. The parameters which are important to define the spectral properties of static FP filter are the cavity and DBRs materials, the number of DBR periods, lateral dimension of one filter, the central wavelength of the DBR λ_{DBR} and of the cavity λ_{cav}.

Table 2. Geometrical parameters of the characterized static FP filters and arrays.

Physical parameters for filter device	**SF1 (arrays)**	**SF2 (filter)**	**SF3 (arrays)**	**SF4 (arrays)**
Cavity material	mr-UVcur21	mr-UVcur21	mr-UVcur06	So-gel
DBR materials	TiO_2/SiO_2	TiO_2/SiO_2	TiO_2/SiO_2	SiO_2/Nb_2O_5
DBRs periods	5.5	5.5	5.5	6.5
Central wavelength of the DBR λ_{DBR} (nm)	575	575	575	950
Lateral dimension of one filter (µm x µm)	100 x 100	100 x 100	100 x 100	100 x 100
Central wavelength of the cavity λ_{cav}	----	618 nm	----	----

4.3 Geometric and compositional details of tunable Fabry Pérot filters

Fig. 4.1 illustrates a 3D side view of a tunable FP filter. The filter top view is demonstrated in Fig. 4.2. The vertical dimensions are corresponding to their dimension in z direction. Similarly, lateral dimensions of the filters are corresponding to their dimensions in xy direction. Note that, in the design of our filters, a thin layer of ITO is deposited over the filter substrate and it functions as the bottom electrode. The top electrode is created either by depositing a thin layer of ITO or Al on top of the DBR. In the case of ITO top electrode, a thin layer of ITO is deposited over the whole membrane, the suspensions as seen in Fig. 4.1. In the case of Al top electrode, the deposited Al layer covers the suspensions and only a part of the membrane which form as the donut shape in Fig. 4.3.

Important geometric parameters of the filter are the number of suspensions, the suspension geometry (e.g. straight, bent, angled), the suspension width t, the suspension length ℓ and finally the membrane radius r. The suspension thickness t is calculated by the sum of top electrode's thickness and the thickness of the top DBR. In case the filter has Al as top electrode, the radius of the open part which is not covered by the Al layer is denoted as q (see Fig. 4.3). Other parameters are defined by the mask design of the tunable filter. Those parameters are described in detail in table 3.

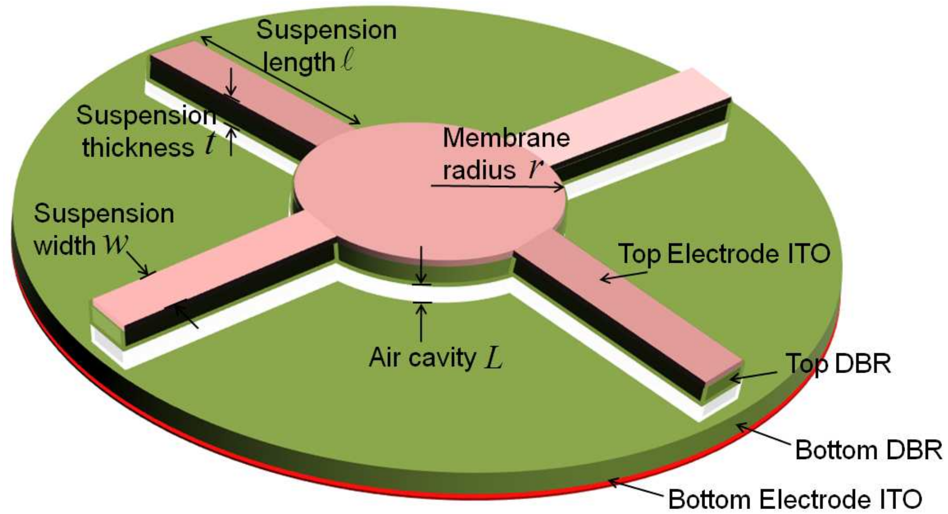

Fig. 4.1. 3D side view of a tunable FP filter with ITO as bottom and top electrodes.

Fig. 4.2. Top view of several tunable FP filters with ITO as the top and bottom electrodes.

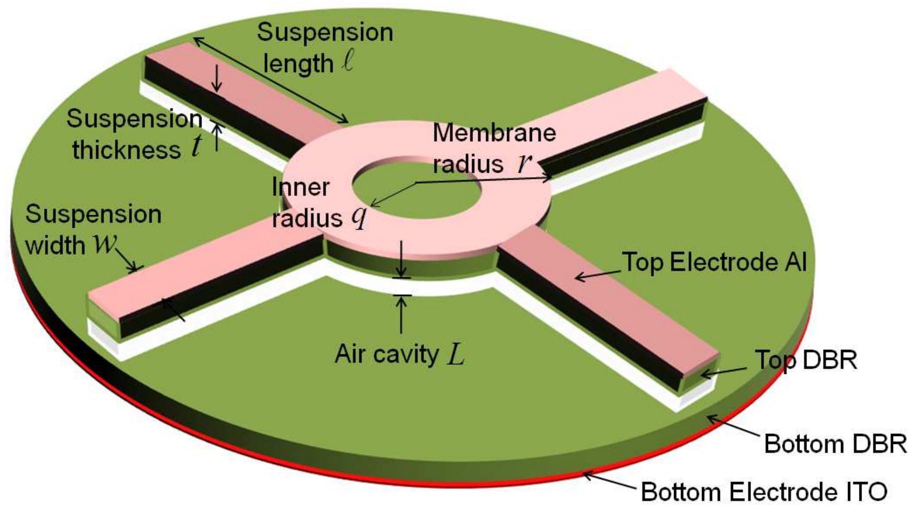

Fig. 4.3. 3D side view of a tunable FP filter with ITO as bottom electrode and Al as top electrodes.

Table 3. Geometrical parameters of the characterized micomachined tunable FP filters.

Physical parameters for filter device	**TF1**	**TF2**	**TF3**	**TF4**
Number of suspensions	4	3	3	3
Suspension geometry	Straight	Bent	Bent	Straight
Suspension length ℓ	30 µm	73 µm	73 µm	65 µm
Suspension width t	8 µm	10 µm	10 µm	6 µm
Membrane radius r	12.5 µm	10 µm	15 µm	30 µm
Inner radius q	----	----	10 µm	25 µm
DBR materials	Si_3N_4/SiO_2	Si_3N_4/SiO_2	Si_3N_4/SiO_2	Si_3N_4/SiO_2
DBRs periods	9.5	9.5	9.5	9.5
DBR central wavelength λ_{DBR}	650 nm	650 nm	650 nm	650 nm
Electrode material	ITO/ITO	ITO/ITO	ITO/Al	ITO/Al

The area acting in the electrostatic actuation is that area part of the membrane which is covered by a conductive material and a weighted part of the suspensions. Note that it is impossible to calculate from the geometry an area A which has been used in the simple elastic models of chapter 2. For the complicated 3D geometries occurring during the displacement and buckling of the membranes a simple model as used in chapter 2 is not accurate enough. A 3D mechanical model such as described in [47] has to be used.

5 Experimental results using the compact microscope spectrometer setup for characterization of Fabry Pérot filter arrays

The experimental results obtained from the compact microscope spectrometer setup reveal the optical properties and tuning behaviors of the static and tunable FP filter arrays and are presented in this chapter. Some parameters of interest such as the $FWHM$, the spectral position of the filter transmission line, and the total spectral bandwidth of the arrays are described. The tuning behaviors in term of mechanical temporal stability and efficiency of electrostatic actuation of the tunable filter arrays while a DC and an AC voltage are applied are further characteristic factors that are needed to determine.

As mentioned in chapter 2, the fabrication process of FP filter arrays requires complex fabrication steps. In fact, each fabrication step may cause a small deviation in the centre wavelength. Therefore, optical characterization is not only applied to accomplished FP filter arrays, it is used after finishing each important fabrication step. For example, after accomplishing the deposition of the first DBR, the unstructured sample is characterized to define its center wavelength. If any variation in centre wavelength is observed, the later fabrication process of depositing the cavity and the top DBR is adjusted properly to compensate this variation, and thus optimize overall optical filter performance. Afterwards, since the whole filter arrays are already structured, each filter is again characterized to investigate its optical properties and tuning behaviors.

5.1 Optical characterization of laterally unstructured Fabry Pérot filters

In this part, optical characterizations of unstructured FP filter UF1 (see table 1, chapter 4) are taken into account. The filter consists of a cavity and two DBRs with Si_3N_4/SiO_2 as high and low refractive index materials. Si_3N_4/SiO_2 materials were chosen due to the low mechanical stress when comparing with other pair of materials e.g. poly-Si/SiO_2 and low-cost fabrication by plasma enhanced chemical vapor deposition (PECVD). To increase the filter's reflectivity and thus obtaining a small $FWHM$ of the filter transmission line, each DBR is designed with 9.5 periods (19 layers) of Si_3N_4 and SiO_2. The deposition of the DBRs is carried out by PECVD. The mr-UVcur06 which is suitable for depositing the cavity is implemented for the fabrication of the cavity with an optical thickness of $\lambda/2$.

As the cavity features an optical thickness of $\lambda/2$, the FSR is significantly large. The separation between filter transmission lines is larger than the filter stop band. Therefore, there is only one filter transmission line presenting within the stopband. Figure 5.1 presents the experimental transmittance spectrum of the filter obtained by the compact microscope spectrometer setup. For spectral analysis the grating spectrometer with the resolution of 0.5 nm is utilized. The spectrum shows a stopband of 110 nm (from 590 nm to 700 nm) in which the transmittance of 58 % at wavelength of 653 nm. The $FWHM$ of the filter transmission line is 2.8 nm.

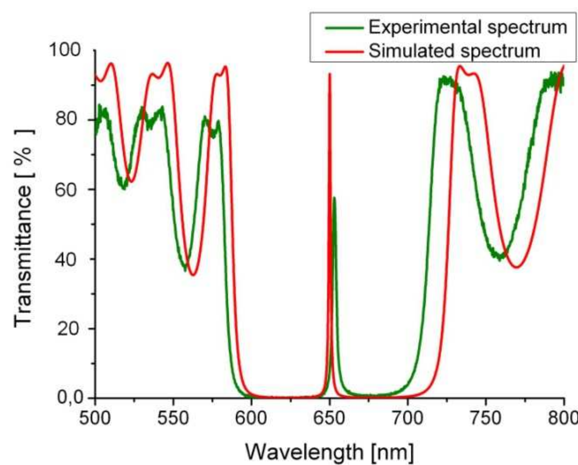

Fig. 5.1. Experimental and simulated spectrum of a nonstructured FP filter: 9.5 periods of Si_3N_4/SiO_2 DBR, mr-UVcur 06 for $\lambda/2$ cavity, central fabricated wavelength of 650 nm.

In order to verify the optical quality of the characterized filter as well as the accuracy of the characterization setup, a transmission spectrum of the filter is theoretically calculated and then utilized for simulated and experimental spectral comparisons. The simulated transmission spectrum is presented in Fig. 5.1 showing a stop band of 120 nm, and a filter transmission line at centre wavelength 650 nm with 93 % transmittance, the achieved $FWHM$ is 1.2 nm.

Comparing simulated data and experimental data, correlations in the spectral bandwidth, and the spectral position of the filter transmission line are observed. A small shift to longer wavelength of the filter transmission line inside the stopband is most likely caused by variation of the real cavity thickness. Due to the high number of layers for top and bottom DBR and the cavity, a marginal material absorption in Si_3N_4 and SiO_2 layers lead to the decrease of maximum transmittance of the filter transmission line within the stopband. A broader filter transmission line in experimental spectrum with a $FWHM$ of 2.8 nm is observed, whereas the optical simulation predicts a $FWHM$ of only 1.2 nm for

this filter. The reason of this broadening probably comes either from the inhomogeneity of the deposited layers, or from some defects such as dust occurring during fabrication processes. These defects are able to scatter the incident light which leads to the increase of the incident angle.

For any new technique to be used, it must be demonstrated that it gives results in agreement with more established techniques. In this case, a comparison of the compact microscope spectrometer system and the spectra from Lambda 900 spectrophotometer[24] (see chapter 3.1) are treated with some caution (Fig. 5.2). In both cases, the spectral resolutions are chosen as 0.5 nm. Spectrum achieved from Lambda 900 spectrophotometer also shows the stopband of 110 nm, a filter transmission line transmittance of only 30 % and a $FWHM$ of 5 nm.

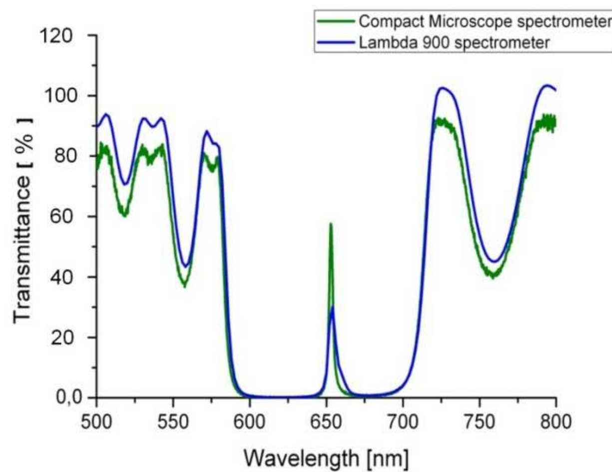

Fig. 5.2. Spectrum achieved from the compact microscope spectrometer and the Lambda 900 spectrophotometer when measuring the nonstructured FP filter.

The observed resemblances in the spectral positions of the filter transmission line and the stopband between two spectra indicate the reliability of the compact microscope spectrometer setup. The different transmittance of the filter transmission line and the narrower $FWHM$ is referred to the difference in the inspected position and in the size of the inspected area. Note that, the filter is not perfectly homogenous; it always contains some defects which causes the reduction of the transmittance and the expansion of the $FWHM$. Therefore, measuring in different positions leads to a slight variation in the transmittance and the $FWHM$ of the peak. Even though the same position is selected for characterization, the inhomogeneity of the filter still gives rise to the variable transmittance and $FWHM$ when the size of the inspected areas are different in the two setups.

[24] Lambda 900 UV/Visible/NIR spectrophotometers PerkinElmer

The size of the inspected area in the compact microscope spectrometer is varied from ten up to hundred micrometers whereas the inspected area in the Lambda 900 spectrophotometer is approx. 5 mm x 5mm [106].

5.2 Optical characterization of static Fabry Pérot filter arrays

Static FP filter arrays can contain thousand FP filters whose lateral dimensions may vary from ten up to hundred square micrometers. Each filter is required to be characterized separately. The transmission spectra of several static filters in the array are illustrated in Fig. 5.3.

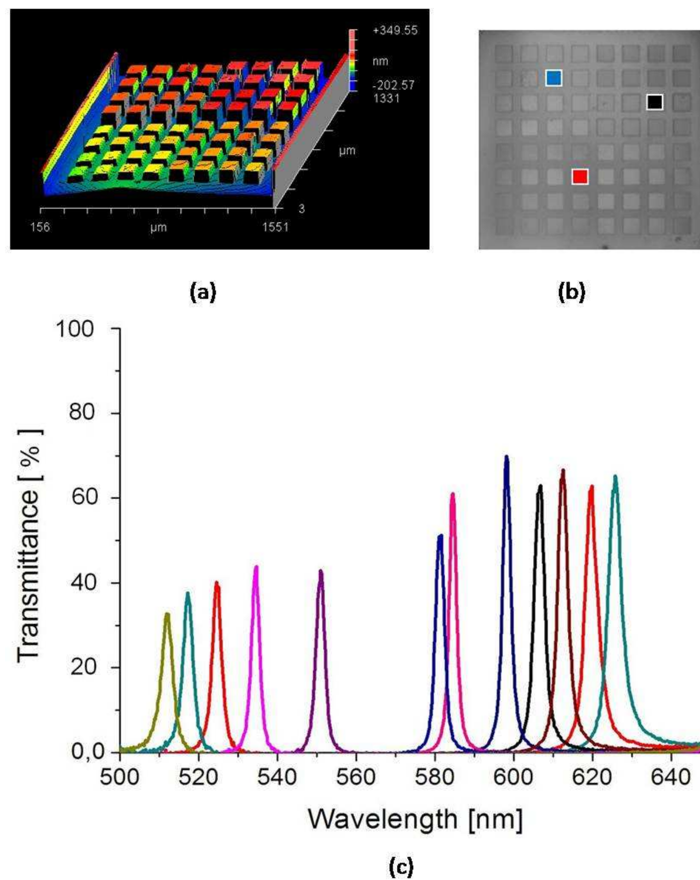

Fig. 5.3. (a) Static filter structure from the side view, (b) topview, and (c) its corresponding spectra. The side view structure is taken from the WLI, the top view structure is taken from the compact microscope spectrometer setup.

Characterized static filter arrays SF1 (see table 2, chapter 4) are implemented with 5.5 periods of TiO_2/SiO_2 for top and bottom DBRs. The cavities are structured by 3D NanoImprint technology using mr-UVcur21 as UV-curable polymer. The lateral filter size is 100 x 100 μm^2. The central wavelength is of 575 nm. For data recording, the

grating spectrometer with 0.5 nm resolution is addressed. The white square in the inset defines the measured area of about 100 x 100 µm^2 which is also the actual size of the filter. The measured $FWHMs$ range between 3 nm and 5 nm. The desired variations of transmitted wavelengths are due to the intentionally varied cavity heights. The thicker the cavity, the longer are the transmitted wavelengths. The variances in transmittance of the filter transmission lines are partly related to (i) the difference in material absorption at different wavelengths of the DBRs and cavity material, to (ii) non homogeneous DBRs concerning individual layer thicknesses and composition inhomogeneities known as undesired chirping effects and (iii) different spectral position with respect to the design center wavelength.

In order to validate the accuracy of the setup in characterizing micro structure dimensions, comparisons of transmission spectra from the compact microscope spectrometer setup and from the simulated calculation in addition with the spectrum obtained from the optical bench setup (see chapter 3.2) are carried out. For this purpose, a static filter in an array SF2 is chosen to characterize. The experimental spectrum of the filter shows a stopband of 190 nm, including a filter transmission line at 618 nm with the transmittance of 62 %. The $FWHM$ of the filter transmission line is 3.7 nm. Comparing the experimental and simulated spectrum (Fig. 5.4), good resemblances in the stopband width and the $FWHM$ are obtained. Again, a deviation in filter transmission line of about 2 nm is observed, which is most probably due to the variation of the cavity heights between the designed and fabricated filter. Another reason which may contribute to the shift to short wavelength is the occurrence of a small tilted angle of incident which leads to a small shift to shorter wavelength of the spectrum. The broader in $FWHM$ and lower in transmittance might be attributed from material absorption and from the imperfection of the DBRs.

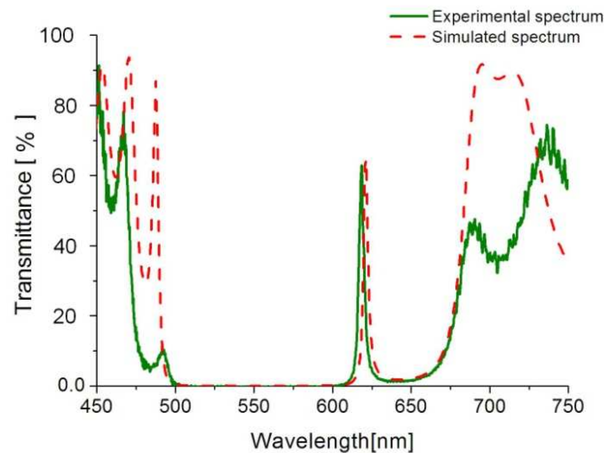

Fig. 5.4. Experimental and simulated spectra of a single FP filter in an array.

The spectra comparison obtained from the two setups the optical bench setup (circular symbols) and the compact microscope spectrometer setup (solid line) is illustrated in Fig. 5.5. The optical bench utilizes a monochromator combined with a HAL lamp as a tunable wavelength monochromatic light source. The wavelengths are swept from 460 nm to 628 nm with 0.2 nm incremental step. The spectra agree very well in the stopband width and the spectral position of the filter transmission line. Furthermore, the higher transmittance of the filter transmission line and the narrower $FWHM$ achieving from the compact microscope spectrometer setup prove the high accuracy of the system in micro structure characterization.

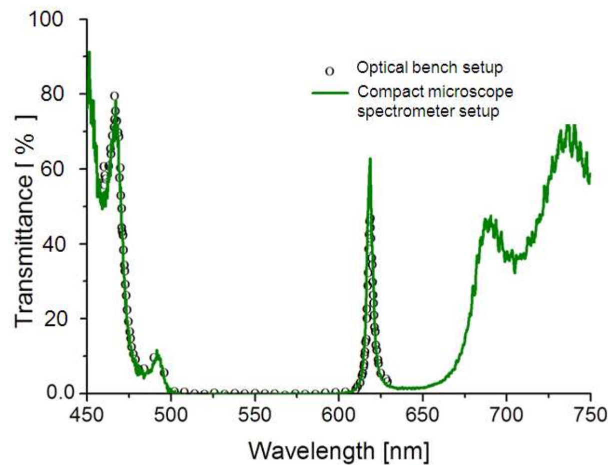

Fig. 5.5. Spectra from the compact microscope spectrometer and the optical bench setup.

5.3 Optical characterization of micromachined tunable Fabry Pérot filter arrays

In this part, the optical characterization of tunable FP filter arrays is presented. Compared to the case of a static filter, a micromachined tunable FP filter generally reveals filter transmission lines of broader linewidths. The reason for the broader spectral linewidth is the undesired and sometimes unavoidable buckling and bending of the released membrane. In case of compressive stress, after the underetching of the filter membranes and suspensions, the residual stress forces the structures to expand. Since the membrane is fixed on 3 or 4 sides, it will be deformed in vertical direction. Primarily, this causes a noticeable vertical buckling of the membrane as demonstrated in the 3D image of the characterized filter in Fig. 5.6 (a). Since the membrane is deformed vertically, the surface curvature can be considered as spherical. This spherical feature observed in Fig. 5.6 (b) represents the variation in a cavity height over the horizontal reference. By applying a Gaussian beam model these deformations cause a significant widening of the incident beam during the multiple reflections within the cavity. It leads

to lateral irradiations of the optical field and cavity losses, results in an increase of the linewidths and in a low transmittance of the filter transmission lines.

However, under certain geometrical conditions of the filter structure, the buckling of the membrane can be utilized as a beneficial point for obtaining better optical performance. Due to the buckling, the top DBR has a certain curvature; it becomes a concave mirror. The filter itself can be considered as a plano-concave resonator which can provide a stable configuration for the confinement of light within the cavity. The confinement condition of the light in a plano-concave resonator occurs when the radius of the membrane sphere is identical to the radius of the curvature of the beam wavefront. This condition refers to the geometrical condition of the filter which is the distance between the top and bottom DBR must be less than the radius of the curvature of the membrane sphere. Under this condition, the tunable filter behaves as a stable resonator [108].

In the following part, these spectral behaviors are investigated further by considering and comparing two different kinds of filter geometries: first a filter with four straight suspensions and second a filter with three bent suspensions.

A tunable FP filter TF1 (see Fig. 4.1 and table 3 in chapter 4) having a 12.5 μm membrane radius (corresponding to 25 μm membrane diameter) mounted by four straight suspensions as illustrated in Fig. 5.6 (a), (b) is characterized first. The suspension length ℓ and suspension width t are 30 μm and 8 μm, respectively. The filter is implemented with 9.5 periods DBRs of Si_3N_4/SiO_2 and an air-gap cavity. In this case, the filter has ITO as top and bottom electrode, and the centre wavelength of 650 nm. The inspected area in this case is 20 μm x 20 μm in diameter denoted as the white square in Fig. 5.6 (c). Again, the spectrometer with 0.5 nm resolution is utilized to analyze the data. The spectrum of a non-actuated filter is denoted as the curve of 0 V in Fig. 5.6 (d).

To actuate the filter, two electrode needles are placed on the microscope translation stage. A DC voltage supply is assigned for electrostatic actuation. The tuning is performed by varying the applied voltage between 0 V to 25 V. Due to electrostatic force, the air cavity height is decreased a few nanometers that corresponds to the movement of the filter transmission line to shorter wavelengths. Fig. 5.6 (d) displays spectra of micromachined tuned filters revealing a total spectral tuning range of 75 nm within a stopband of 125 nm. During the tuning the stopband width and its spectral position did not change.

As seen in the spectrum, the filter transmittances are varied around 50 %. This variation is referred to the optical losses of the tunable filter. Due to the implementation of an air gap cavity, losses which are caused by the cavity such as the wavelength dependent material absorption are considerably reduced. However, optical losses still occur in this

case in the DBR mirrors and as a result of membrane buckling. This buckling gives rise to the lateral radiation of the propagating light beam inside the structure.

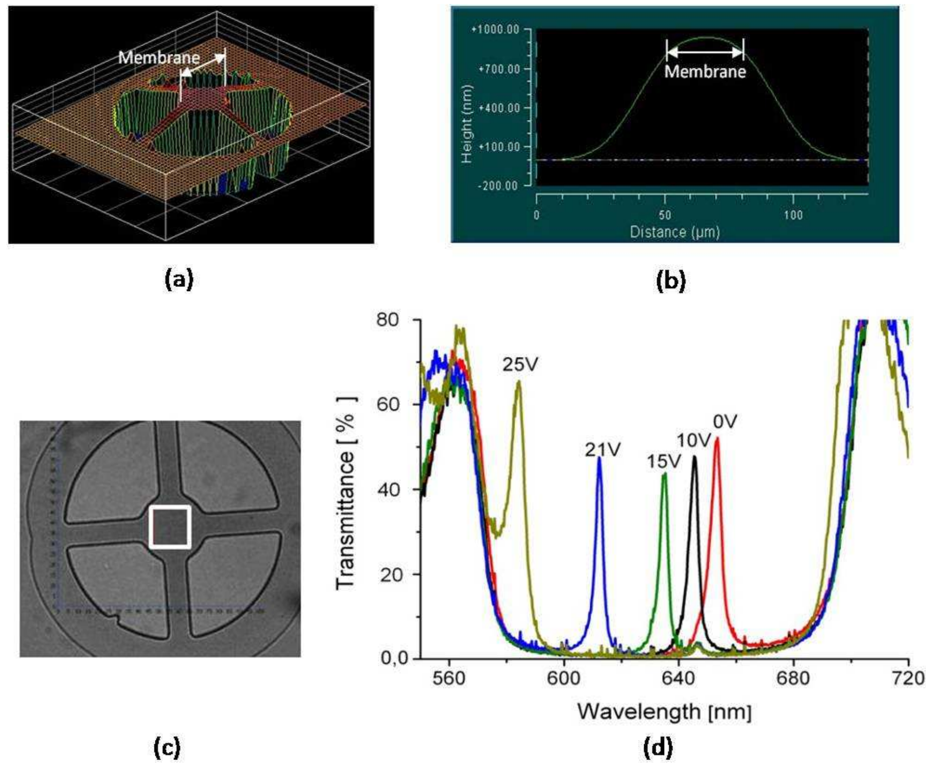

Fig. 5.6. (a) 3D image of the characterized tunable filter TF1 and (b) its measured cavity height captured by WLI, (c) top view of a tunable FP filter with 4 straight suspensions and membrane radius of 12.5 µm, inspected area is 20 µm^2 (white square), (d) corresponding electrostatic actuation results of the tunable FP filter where the applied voltage is increased from 0 V to 25 V.

During actuation, a variation in the $FWHM$ of the filter during tuning is also observed. As described in chapter 2.1.1.3, the $FWHM$ is directly proportional to the absolute wavelength value. Subsequently, for a more detailed evaluation of the filter tuning behavior, the investigation in resolving power $\mathfrak{R}$ of the filter transmission line is performed. Table 4 represents the calculated spectral resolution $\mathfrak{R}$ of five different filter transmissions lines corresponding to five different applied tuning voltages.

In this filter, the resolving power $\mathfrak{R}$ is increased gradually when the applied voltage is increased in the range of 0 to 21 V. This behavior can be explained by considering the change in the radius of the curvature of the membrane. As seen in the Fig. 5.6 (b), before actuation the spherical radius of the membrane is considerably smaller than the cavity height. Since a voltage is induced, an electrostatic force is applied on the whole membrane to push it down. Thus, the air gap is reduced, the bending of the membrane is decreased which results in the increase of the radius of the membrane curvature. If the

applied voltage is increased further, the difference in length between the radius of the membrane curvature and the air gap height is reduced. The increase of the applied voltage also gives rise to the enhancement of resemblance between the radius of curvature of the membrane and that of the Gaussian beam wavefront. This leads to a better confinement of the light within the cavity. As a result, a better spectral resolution of the filter transmission line is achieved. The highest confinement of light is obtained when the radius of the membrane sphere and that of the beam wavefront are identical. And the distance between two DBRs are less than the radius of curvature of the membrane sphere. This condition is depicted in Fig. 5.7.

Table 4. Comparision of resolving power of five filter transmissions lines corresponding to five applied voltages.

Applied Voltage (V)	0	10	15	21	25
λ (nm)	653.51	645.38	635.29	612.19	584.34
$FWHM$ (nm)	4.5	4.0	3.5	3.0	7.8
$\Re$	145.2	161.3	181.5	204	74.9

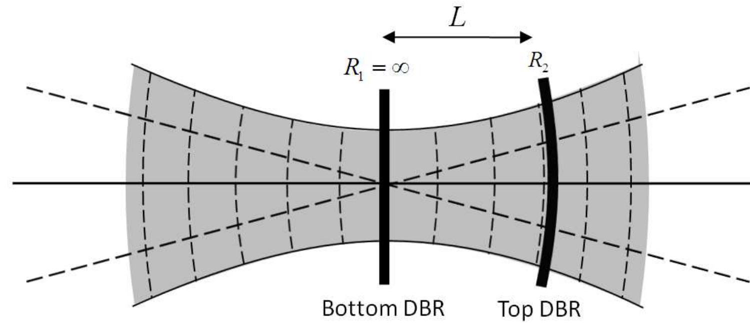

Fig. 5.7. Schematic diagram of the tunable FP filter TF1 and the Gaussian beam wavefront propagation. The filter is considered as a plano-concave resonator. When the confinement condition is satisfied, the radius of the membrane sphere is the same as the radius curvature of the beam wavefront. The air gap cavity length L must be equal or less than the radius of the curvature of the top membrane sphere R_2.

Since the applied voltage is increased further to 25V, here, an obvious decrease of the resolving power $\Re$; i.e. an increase of $FWHM$ is observed. At this voltage, the filter transmission line locates near the edge of the stopband where the reflectivity of the mirror is decreasing. Thereby, it results in the increase of the $FWHM$ value according to Eq. 2.11 in chapter 2.1.1.3.

Another example of spectral tuning behaviors of the tunable FP filter is demonstrated in Fig. 5.8. A tunable filter TF2 (see also Fig. 4.1 and table 3 in chapter 4) with three bent suspensions consisting of 9.5 periods of Si_3N_4/SiO_2 DBRs with three bent suspensions is taken into account. Similarly to the previous case, the filter has ITO as top and bottom electrode, and the centre wavelength of 650 nm. The filter membrane radius is of 10 µm (corresponding to the diameter of 20 µm). The inspected area is around 15 µm x 15 µm depicted as white square in Fig. 5.8 (b). Again, electrostatic actuation is performed by a DC voltage supply. The tuning is induced by a variance of applied voltages from 0 V to 21.8 V, resulting in a tuning range of 55 nm.

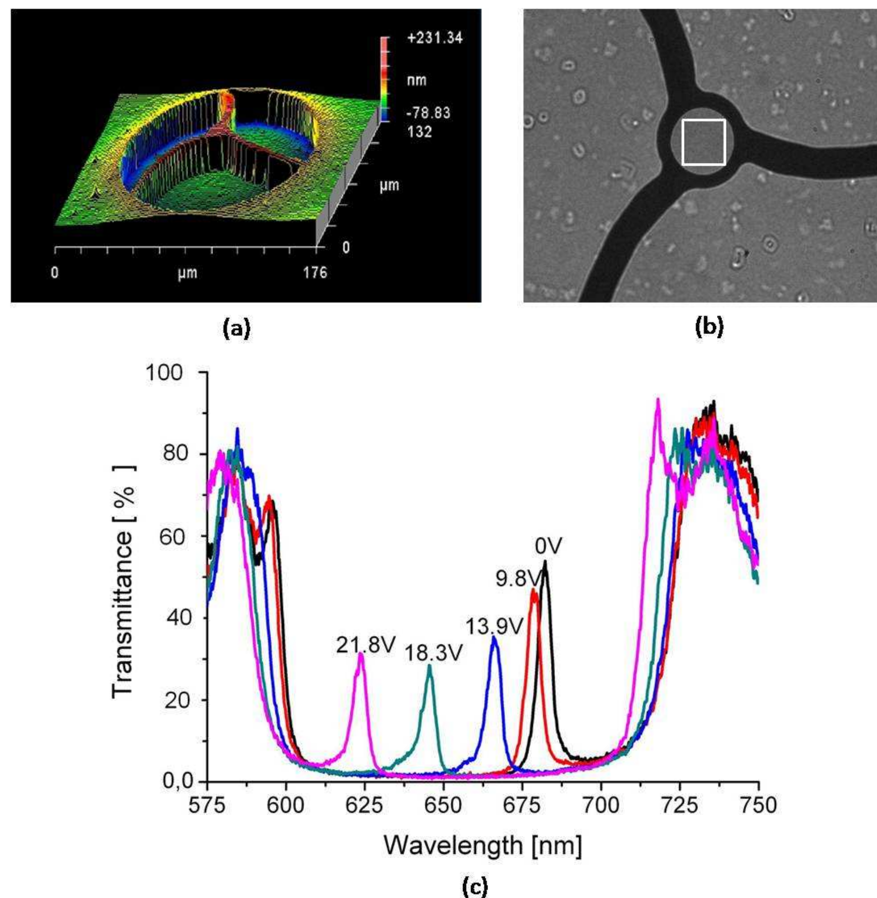

Fig. 5.8. (a) Top view of the tunable FP filter TF2 with 3 bent suspensions and membrane radius of 10 µm (diameter of 20 µm). (b) The inspected area is 15 µm x 15 µm (white square). (c) Corresponding electrostatic actuation results of tunable filters since the applied voltage is increased from 0 V to 21.8 V.

Compared with the previous case where the $FWHM$ of the filter is decreasing during actuation, a reverse situation is observed in this case. As seen in the spectrum, increasing applied voltage results in a considerable broadening of the linewidth from 7 nm to 15 nm together with an attenuation of the filter transmittance from 55 % to 30 %. This

effect can be explained by the tilting and bending of the membrane during actuation. Note that, in this case the filter TF2 consists of three bent suspensions which have the benefit of a higher flexibility for moving. However this asymmetric construction make the filter become highly sensitive to misalignments or defects during fabrication process. For instance, if one of the suspensions is weaker than the others, it may cause the tilting and bending of the filter membrane which later results in unexpected spectral behaviors. In this case, the enhancement of spectral linewidth, the reduction of transmittance together with the small shift to shorter wavelength at the “root” of the filter transmission lines are probably the consequence of the tilting and bending of the membrane during actuation. Because of these effects, the propagating Gaussian beam widens, causing lateral irradiation which is related to cavity losses. Thus, the filter transmittance is reduced and the $FWHM$ is increased.

Different tuning behaviors of the two actuated filters TF1 and TF2 were observed and investigated in this part. The differences are caused by the different geometrical designs of the filters such as the membrane diameter, the number of suspensions, suspension lengths and widths, as well as the type of suspensions e.g. bent, straight and angled. These parameters cause substantial impacts on tuning behaviors of the filter arrays. Further investigations on the influences of these parameters on the optical, mechanical and tuning behaviors of tunable filter in both, theoretical and experimental aspects are already acquired in other researches at INA [48, 50, 51].

5.4 Comparison of micromachined optical tuning of Fabry Pérot filter arrays under DC and AC actuation

Up to now the electrostatic actuation of the FP filters has been done simply by a varying a DC voltage, which we will denote “DC actuation” below. To study the tuning behavior in terms of stability and charging effects of dielectric materials we now apply a more sophisticated electrostatic tuning via a varying AC voltage, which we will denote “AC actuation” below. In this chapter, by comparing DC and AC actuation we will study in detail the influence of the character of actuation (DC or AC) on the linewidths of the transmission lines, the temporal mechanical stability and the efficiency of tuning. The compact microscope spectrometer will be used for this investigation. The results of the comparison between DC and AC actuation are explained in a preliminary way by a new model including the dynamics of trapping and reemission of charges in dielectrics in a subsequent part.

5.4.1 DC Actuation

DC actuation is a conventional method of MEMS actuation; it has been used widely due to simple equipment provision and simple measuring procedure. In this part, the spectral properties and tuning behaviors of the tunable FP filters are investigated when a DC voltage is applied. Figure 5.9 (a) illustrates the schematic diagram of a tunable filter TF3 actuated by a DC voltage. The DC voltage is applied between the top and bottom electrode of the tunable filter (the movable top DBR always has a positive potential on its electrode; the fixed bottom DBR always has a negative potential on its electrode). The resulting electrostatic force actuates the top DBR towards the bottom DBR. Thus, the top DBR is moving down in z direction (vertical direction), which results in a reduction of the air gap cavity. The initial height of the air gap cavity is L. The displacement of the movable top DBR is h.

A top view of the micromachined tunable FP filter TF3 located inside an array is depicted in Fig. 5.9 (b) and characterized subsequently in tuning behavior. The filter consists of 9.5 periods of Si_3N_4/SiO_2 for top and bottom DBRs. An air gap is implemented between the two DBRs, the centre wavelength is of 650 nm nm. The top DBR is mounted and positioned by three bent suspensions. Each suspension is characterized by a length ℓ , a width w and a thickness t. The membrane radius is of 15 µm (diameter of 30 µm). The inner radius of 10 µm . The filter has Al as top electrode, and ITO as bottom electrode. See also Fig. 4.3 and table 3 in chapter 4.

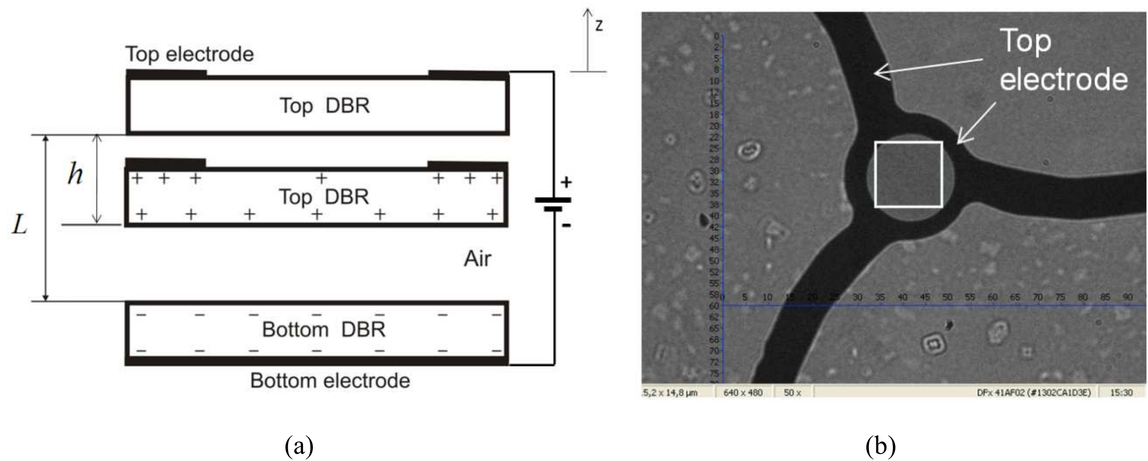

(a) (b)

Fig. 5.9. (a) Schematic diagram of a tunable filter actuated by a DC voltage and (b) top view of the characterized tunable filter TF3 consisting of three bent suspensions, the radius of the membrane is of 15 µm, the inner diameter is of 10 µm. The filter has Al as top electrode and ITO as bottom electrode.

The spectral behaviors of the tunable filter are displayed in Fig. 5.10. The filter is actuated by applying a DC voltage varying from 0V to 12 V. As seen in the figure, at 12 V a

second mode appears inside the stopband. In optical applications of the nanospectrometer, the second mode is not usable because the detector would detect both modes at the same time and would not distinguish between the different wavelengths of these modes. However, in this work, the investigation of the spectral properties of the filters are the priorities, therefore, spectra with a second mode are still taken into account.

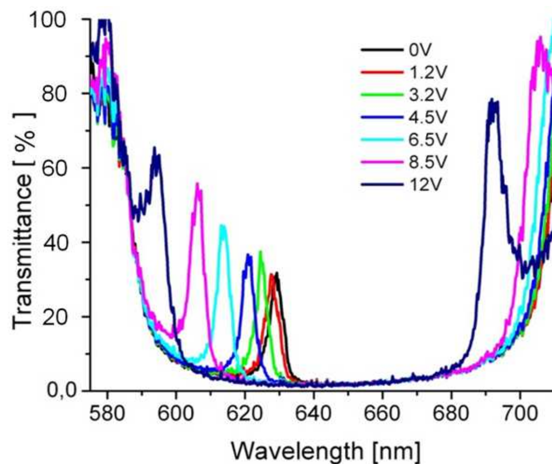

Fig. 5.10. Transmission spectra of the characterized tunable filter TF3 using DC actuation, the applied voltage is varying between 0 V to 12 V.

In parallel with spectral investigations, investigations of the mechanical displacements of the tunable FP filter are also performed using white light interferometer measurements[25]. The displacement of the membrane of filter TF3 as a function of applied voltage is illustrated in Fig. 5.11.

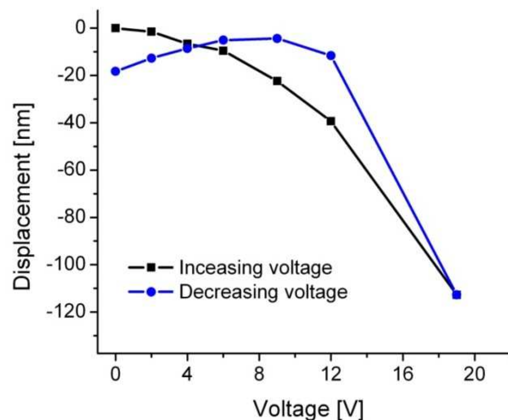

Fig. 5.11. Displacement of the membrane of the filter TF3 as a function of applied voltage using DC actuation.

[25] NewView 5000 Zygo

The applied voltage is altered between 0 and 19V. The square symbols denote the spectral change of the transmission line during a gradually increasing applied DC voltage. The circular symbols, on the other hand, present the spectral change of the transmission line during a gradually decreasing voltage applied. When a certain voltage is applied between the top and bottom electrodes, the membrane moves downward as a result of the resulting electrostatic force. The vertical displacement of the membrane is approx. 120 nm when the applied DC voltage is 19V. As can be seen in the figure, a noticeable mismatch in the vertical displacements of the membrane at a certain voltage applied is observed when this specific voltage is passed during an increasing or decreasing voltage in different experimental runs. Most probably this is due to charging effects of the dielectric materials of the DBRs occurring during actuation. If a DC voltage is applied to the tunable filter, positive charges are permanently located on one electrode and negative charges are permanently located on the other electrode. Despite the dielectrics (e.g. Si_3N_4 and SiO_2) are isolators, transfer (transport) of charges into the dielectric bulk layers occurs and the charges energetically may relax into traps (trapping). This effect is called dielectric charging of the dielectric materials and leads to undesired mechanical movements of the membranes and, thus, undesired spectral tuning of the transmission line. Since for an application the spectral position of the transmission lines are required to maintain constant, the undesired tuning is considered as a fact of "temporal instability". It will be shown that the undesired tuning effects which would require additional compensation efforts can be partly avoided by another electrostatic actuation of improved performance (AC actuation) which is presented and studied in the following part.

5.4.2 AC actuation

Depending on size and materials, MEMS devices have the resonance frequencies in the range of several tens kHz to a few MHz. In this chapter we present experimental results performed under three different AC actuation frequencies: in two cases above the resonance frequency (eigen-frequency) and in one case below the resonance frequency. We will demonstrate three important results:

1. The undesired effects involved via dielectric charging can be reduced, thus, the temporal stability is increased.
2. The compensation effort can be minimized.
3. The electrostatic actuation efficiency can be increased under certain conditions.

For AC actuation, an AC voltage is applied between the top and bottom electrodes of the filter, without an external DC bias. If the electrode of the top DBR has a positive potential and the bottom electrode top electrode has a negative potential, an attractive

force is generated. Also for the opposite case in which the top electrode has a negative potential and the bottom electrode has a positive potential, an attractive force is always created. However this attractive force is varying during time as a function of the phase of the AC voltage. The attractive force periodically will pass a minimum and there will become zero, but it will never become repulsive. The attractive electrostatic force oscillates with the double frequency as the AC voltage oscillates. At very low excitation frequencies the mechanical oscillator (membrane and suspensions) exactly follows the temporal variations of the electrostatic actuation force (external excitation force). Well below the resonance frequency the maximum membrane displacement is independent of the excitation frequency. Coming closer to the resonance frequency the maximum amplitudes are increasing, reach a peak at the resonance frequency and tend to zero for excitation frequencies increasing beyond. Above the resonance frequency the mechanical oscillator is less able to follow the fast oscillations the higher the frequencies are. This experiment is well-known as *"amplitude modulation response"*. This was not the goal of this thesis, but it will be a topic of a forthcoming thesis. For the experimental data described below, it is important to point out, that even though the polarities of the two electrodes is changing alternatively, the direction of the electrostatic excitation force generated between the two electrodes does not change. The electrostatic excitation force is always attractive which forces the top DBR to move down as already mentioned, which results in the shift of the filter transmission lines to shorter wavelengths within the stopband.

The transmission spectra are measured by the compact microscope spectrometer system. In addition, the mechanical displacement of the membrane is characterized by the white light interferometer.

In order to generate an AC voltage signal, an additional electrical system is utilized as shown in Fig. 5.12. This system includes a function generator, an amplifier, an oscilloscope and two contact needles. The aim of the function generator is to generate a sine wave signal with variable frequencies. The amplifier is assigned to vary the amplitude of the AC signal from the function generator and then supply it to two contact needles. An oscilloscope is used to display the applied AC voltage frequencies and, thus, always half of the electrostatic excitation frequency applied to the filter. The DC voltage part is always set to zero, as already mentioned. These electrical devices are combined with the compact microscope spectrometer setup or the white light interferometer to complete the AC actuation systems, respectively.

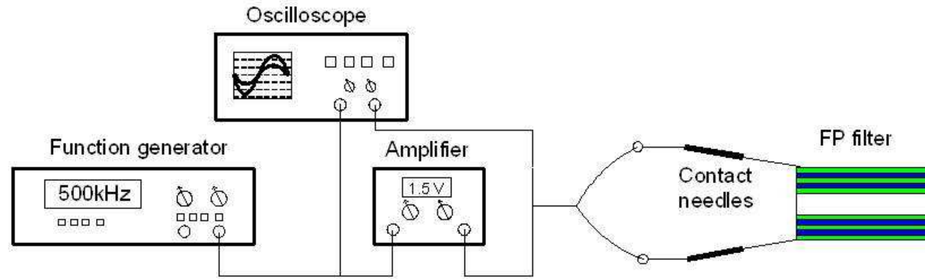

Fig. 5.12. Block diagram of the electrical set-up for AC actuation.

Fig. 5.13 presents the spectra taken for different AC voltage amplitudes. The filter transmission lines are spectrally broadening more and more and finally are spreading over a considerable part of the stopband, when the voltage is increased gradually from 0 V to 28 V. Note, that the AC voltage amplitudes refer to the half of the peak to peak voltage. This phenomenon can be explained in such a way that for an AC voltage frequency of 100 KHz which is not far from the mechanical resonance frequency of the filter, the filter still can follow the periodic external excitation force. The higher the amplitude of the applied AC voltage, the higher the amplitude of the mechanical oscillation of the membrane and, thus, the wider the spectral range the filter transmission line is touching during its oscillations. Hence, the larger the amplitude of the AC actuation, the broader and the less distinct the transmission line becomes in the spectrum. With other words, this leads to a noticeable decrease of the filter transmission lines quality, and a considerable enhancement of the $FWHM$. In the literature some authors call this behavior an "unstable one".

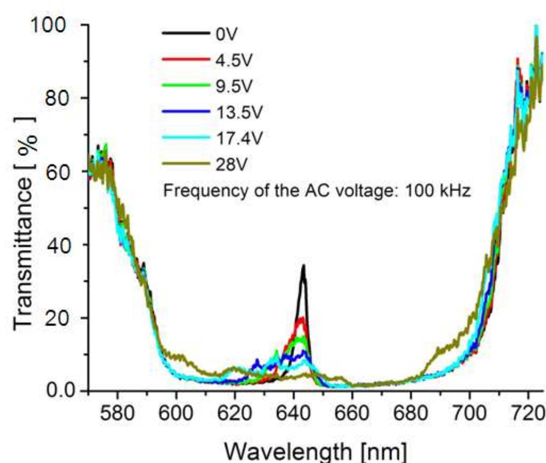

Fig. 5.13. Transmission spectra of the tunable filter TF3 for an AC voltage frequency of 100 KHz is applied. This corresponds to an electrostatic force frequency of 200 kHz.

In the following, two AC voltage frequencies 500 kHz and 1 MHz (corresponding to electrostatic excitation frequencies of 1 MHz and 2 MHz, respectively) which are above the resonance frequency optical and mechanical characterization experiments are performed as well.

The results of spectral and mechanical measurements where an electrostatic excitation frequency of 1 MHz is applied are illustrated in the Fig. 5.14 below.

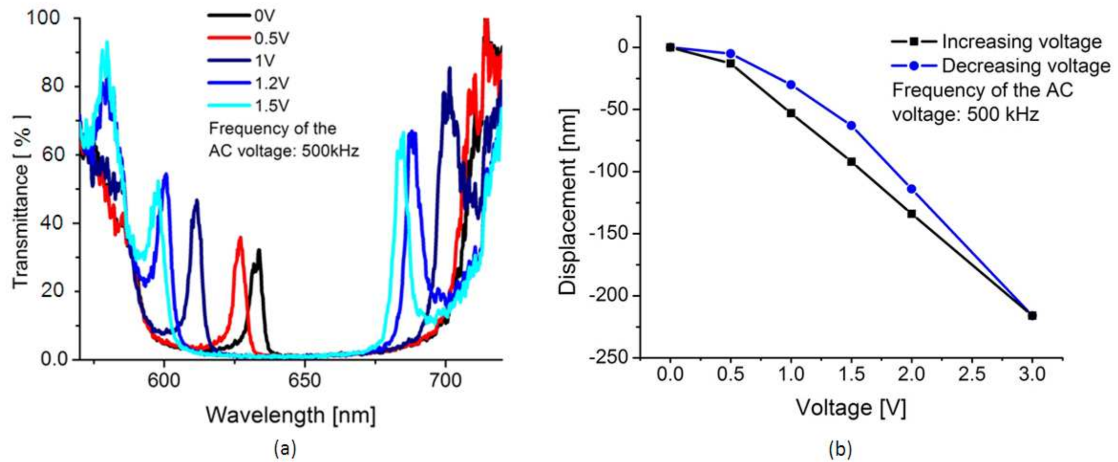

Fig. 5.14. (a) Transmission spectra and (b) mechanical displacement of the membrane using AC actuation for an AC voltage frequency of 500 KHz. This corresponds to an electrostatic force frequency of 1 MHz.

As it can be seen in Fig. 5.14 (a), the spectra present a clearly observable tuning of the filter transmission line when the applied AC voltage varies from only 0 V to 1.5 V. Note, that the linewidth seems to be unchanged. We do not observe the linewidth broadening described above. Since the excitation frequency is above the resonance frequency, the membrane is nearly not oscillating anymore and the spectral position of the filter transmission line is not changing any more in resolvable way. The membrane cannot follow the sinusoidal oscillation of the excitation force. Hence, it becomes nearly static (in the literature some authors call it “more stable”). It is remarkable how small the required AC voltages are for such a strong spectral tuning, if DC and AC tuning is compared. This will be explained in more detail in the following chapter.

Similarly to the DC actuation case, the investigations of the membrane displacement under AC actuation and an excitation frequency of 1 MHz were conducted by increasing and decreasing the applied AC voltages series several times. In Fig. 5.14 (b), the increasing voltage series is depicted by the square symbols whereas the circular symbols denote the decreasing voltage series. The mechanical displacement is in a range of 0 nm to 225 nm. As illustrated in the figure, the curves corresponding to the increasing

and decreasing series are appearing much more similar than in the DC case (Fig. 5.11) and, thus, a smaller hysteresis (a better mechanical stability in the words of some authors in the literature). Moreover, in this case the applied AC voltage needed for the displacement of more than 200 nm is only 3 V. This significant reduction in applied voltage value demonstrates that an improved efficiency of electrostatic actuation can be obtained using high excitation frequency above the resonance frequency.

Now, the spectral and mechanical behavior of tunable FP filters is investigated further by increasing the electrostatic excitation frequency up to 2 MHz, which is well above the mechanical resonance frequency of the filter. The transmission spectra and mechanical displacement profiles for an electrostatic excitation frequency of 2 MHz are presented in Fig. 5.15 (a) and Fig. 5.15 (b), respectively. Also in this case the linewidth is not broadening, since the membrane is now behaving nearly completely static (stationary). Of course, a mechanical system always oscillates very weakly due to acoustic noise and temperature. According to this figure, the variance of applied voltage from 0 V to 0.28 V results in a wavelength tuning range of 45 nm. In the mechanical tuning results, we already observe 80 nm displacement of the membrane for only an AC voltage of 0.45 V. As an experimental result we conclude: the higher the applied frequency, the lower the applied voltage which is required, and the more stationary the membrane becomes.

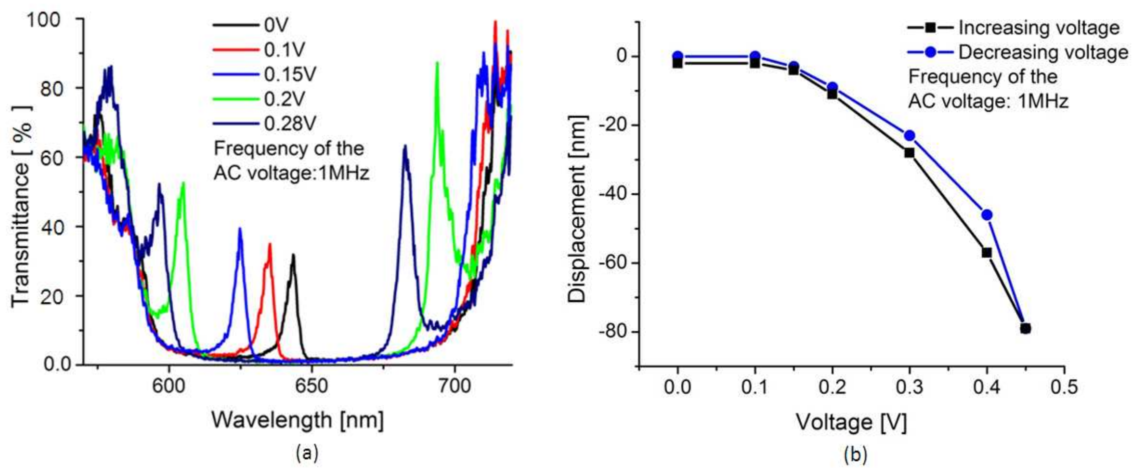

Fig. 5.15. (a) Transmission spectra and (b) mechanical displacement of the membrane using an AC voltage frequency of 1MHz. This corresponds to an electrostatic force frequency of 2 MHz.

As mentioned above, the electrostatic excitation force is varying with time but is always directed in the same direction. The force oscillates between a maximum and a minimum (which is zero). Within this short section we consider a situation above resonance frequency. The higher the frequency the better is the approximation that the membrane

experiences a "static" average electrostatic force. This "static" average electrostatic force was calculated in detail in the literature in Ref. [59] for a similar oscillator geometry as ours but current drive instead of voltage drive.

In order to define a better efficiency of electrostatic actuation, as well as a better mechanical stationary, comparisons in spectra and in mechanical displacement of the tunable filter are performed for two cases: 2 MHz electrostatic excitation frequency (AC voltage frequency of 1MHz) and DC actuation are compared (Fig. 5.16). The variances of the spectral positions of the filter transmission lines, as well as the variances of the corresponding mechanical displacement profiles of the membrane at a considered fixed voltage are investigated by repeated measurements.

For both cases, the procedure to increase and decrease the voltage gradually and repeatedly is performed (to study hysteresis) and the locations of the respective spectral position of the filter transmission line is monitored. The measurements are repeated four times, respectively. The same color spectra denote the same applied voltage. The spectral behaviors of the filter in the case of DC and 2 MHz excitation frequency are depicted in Fig. 5.16 (a) and (b), respectively. In order to obtain a better view of the transmission spectra, the two enlarged images of AC (c) and DC (d) actuation transmission spectra at 0.15 V and 6 V are taken into account.

As seen in Fig. 5.16 (a) and (b), the AC actuation reveals by far better a performance than the DC actuation. In case of AC actuation, the filter transmission lines are located nearly at the same position in the transmission spectra for a constant voltage. For an AC voltage of 0.15 V, the variance of the filter transmission lines position is approx. 3.5 nm as seen in Fig. 5.16 (c). In contrast, in the case of DC actuation a strong spectral shift is observed, expressing a much higher "instability" while studying the reproducibility. For DC actuation, e.g. at 6 V, the variance of the filter transmission lines is approx. 11 nm, see Fig. 5.16 (b). At the applied voltage of 0 V, the variance of the filter transmission line is 13 nm in case of DC actuation. This variance for DC actuation is three times larger than the variance observed for AC actuation. This is due to the negative influence of the charging effects in dielectric materials when the filter is actuated by DC voltage, since the amount of charges relaxing into the traps (trapping) can increase with time. For a long time period the trapping can even reach saturation and a strong deviation to the situation obtained shortly after applying a new situation (a new voltage). In the case of AC actuation the sign of the potential is changed periodically and the trapped charges can again be released from the traps. Thus, the effect of dielectric charging is reduced in the case of AC actuation compared to DC actuation [59, 65]. However, as we will see in chapter 5.4.3, a more detailed model including the dynamics of tunneling, transfer, transport, capture, relaxation and reemission is required to explain more phenomena

exceeding the simple comparison between AC and DC actuation above. These dynamics together with parasitic capacities might explain that we require much smaller AC voltages compared to DC voltages to obtain the same mechanical displacement.

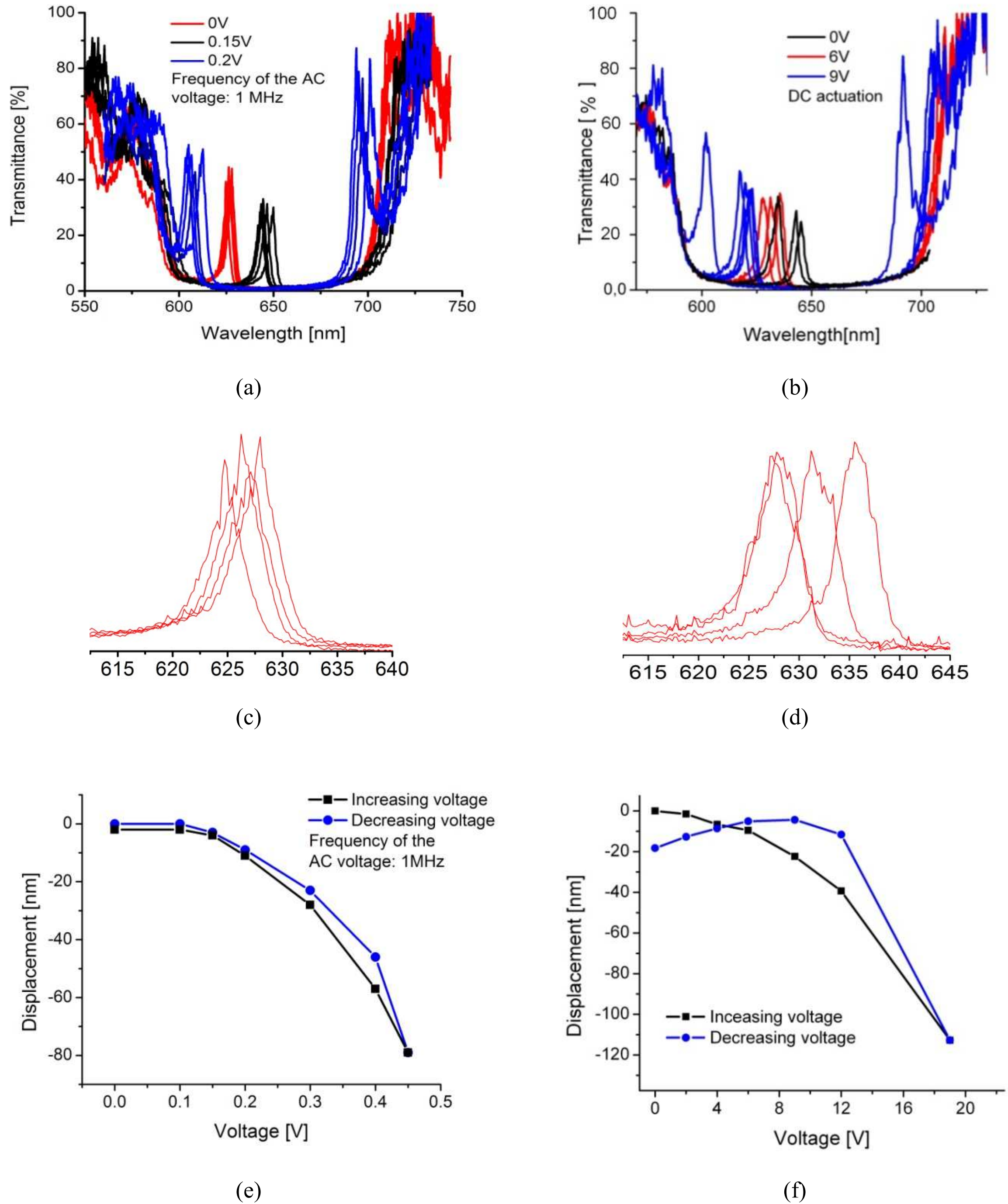

Fig. 5.16. (left row: a,c,e) Comparison between AC actuation and (right row: b,d,f) DC actuation, (a) transmission spectrum for AC actuation, (b) transmission spectrum for DC actuation. (c) The enlarged images of transmission spectra for AC and (d) DC actuation at 0.15 V and 6 V, respectively. In each figure, the same colors denote the same applied voltage. This also holds for the red color between (a) and (c) as well as for (b) and (d), respectively. (e) Mechanical displacement profiles and (f) for AC and DC actuation, respectively.

Figure 5.16 (e) and (f) illustrate a comparison in mechanical displacement between DC and AC actuation. For an AC electrostatic excitation, a frequency of 2 MHz and increasing and decreasing voltage series are applied, we observe a high reproducibility (c) and a corresponding weak hysteresis in the membrane displacement profiles (e) which are in good agreement which each other. For a DC actuation and increasing and decreasing voltage series, in contrast, we observe a weak reproducibility (d) and a corresponding strong hysteresis in the membrane displacement profiles (f) which also are in good agreement among each other. The maximum displacement deviation of below 10 nm at 0.4 V achieved in the case of AC actuation as compared to almost 30 nm displacement at 12 V in the case of DC demonstrates the higher stationary behavior of the filter under AC actuation. Furthermore, the remarkable lower applied voltage of the AC actuation less than 1 V in all cases indicates much higher actuation efficiency than for DC actuation.

Additionally, during operation, a DC actuation condition always requires longer response times. In Fig. 5.16 (f) we observe a difference in the membrane displacement of 13 nm between the initial condition shown in black at 0 V (before applying a voltage) and after increasing the voltage to the maximum value and subsequently after gradually reducing the voltage again to 0 V.

If the applied DC voltage is set from a high value again back to 0 V, always a few minutes are required until the displacement value reaches again 0 nm (observed by the white light interferometer, electro-mechanical characterization). In the case of spectral characterization, the same amount of time is required to reach the spectral position of 0 nm (i.e. the original non-actuated spectral position before starting the actuation). In the case of DC actuation, due to the restoring charge in dielectric layers the membrane needs a certain time to completely discharge until the original non-actuated state is established. In contrast, AC actuation performs a very fast time response. The original spectral position is nearly instantly reached when the voltage is reset to 0 V. In agreement with this observation the original spatial displacement value is also nearly instantly reached when the voltage is reset to 0 V. The charging effect is considerably reduced as an AC actuation is utilized. Since rapid changes from positive to negative charging in both electrodes occur regularly in each period, positive charges trapped in the first half of a period will be reemitted or alternatively neutralized by negative ones in the second half of an oscillation period of time. Thus, by permanent periodic charge neutralization, the number charges being permanently trapped inside the bulk of the dielectric material is drastically decreased. The time charges remain trapped in dielectric layers is significantly depending on the frequency.

In conclusion, AC actuation demonstrates that it can be used for MEMS actuation with higher temporal stability, better repeatability, and better efficiency of electrostatic actuation under certain conditions. The undesired effects involved via dielectric charging can be reduced, thus, the temporal stability is increased. As compared to the conventional DC electrostatic actuation, AC actuation requires a much lower actuation voltage. Depending on the required amount of stability, AC or DC actuation can be chosen to satisfy the requirements of the system. In the following a more detailed explanation based on a new proposed model [109] is given, involving a large number of different effects in the dynamics of electrostatic charging effects of the dielectric DBR materials.

5.4.3 Model for the dynamics of trapping and reemission of charges in dielectrics

Dynamic physical and chemical phenomena are often described by a set of rate equations. A first example is carrier dynamics in semiconductor nanostructures involving spatial transport rates, capture rates and release rates, as well as different energetic levels, which in addition often are spatially separated. The carrier dynamics in one and two dimensional electron-hole gases (quantum wires and quantum wells) with interface roughness (Fig. 5.27 in Ref. [110]) is an example which involves trapping and subsequent release of positive and negative charges into and out of traps of different energetic levels. A second example is related to carrier capture, reflection, transmission and transport phenomena in quantum wells used as distinguishable local traps for carrier transport [111]. A third example again from semiconductors is related to the dependence of wet-chemical etching rates on the doping level, i.e. on the absolute values of electron and hole densities. The latter phenomena have been used to fabricate grating structures in a semiconductor surface exposed to both, a liquid etchant and 2 or 3 laser beams in a laser holography setup [112].

Charging effects of dielectric materials of an insulator/metal interface and the importance for electrostatic actuation of MEMS has been reported and investigated by several groups [65, 66, 113] as already discussed above. The following theoretical model tries to describe the experimental data presented in the chapter 5.4.2 and involves the **dynamics of trapping and reemission of charges in dielectrics** based on rate equations. The involved phenomena are definitively very complex and probably would need a kinetic modeling based on e.g. a Boltzmann transport equation as well as relaxation in energy and k-space. To the best of my knowledge such a model has not been developed and used up to now. However in order to keep our model in a first approach as simple as possible, only rate equations and characteristic transfer times for different processes between the 7 different states are taken into consideration (Fig. 5.17). All involved pro-

cesses are based on the population of 6 different energy levels inside the dielectric medium as well as the metal as the seventh state. The energy levels and the processes are listed in the following:

- Barrier layer in which transport for the negative charges takes place (modeled by a transport rate with a characteristic scattering time $\tau_{n\ transp}$)
- Trap level 1n in a distance d_1 to the metal-dielectric interface (modeled by a capture rate with a characteristic time $\tau_{1n\ cap}$ and a reemission rate with a characteristic time $\tau_{1n\ re\text{-}em}$, in the following only the characteristic times are shown) **"interface trap for negative charges"**
- Trap level 2n in a distance d_2 to the metal-dielectric interface (capture and reemission: $\tau_{2n\ cap}$, $\tau_{2n\ re\text{-}em}$) **"bulk trap for negative charges"**
- Barrier layer in which transport for the positive charge takes place (modeled by a transport rate with a characteristic scattering time $\tau_{p\ transp}$)
- Trap level 1p in a distance d_1 to the metal-dielectric interface (capture and reemission: $\tau_{1p\ cap}$, $\tau_{1p\ re\text{-}em}$) **"interface trap for positive charges"**
- Trap level 2p in a distance d_2 to the metal-dielectric interface (capture and reemission: $\tau_{2p\ cap}$, $\tau_{2p\ re\text{-}em}$) **"bulk trap for positive charges"**
- Tunneling rates and corresponding tunneling times between the metal state and the dielectric barrier energy levels for negative charges $\tau_{n\ tun}$ and positive charges $\tau_{p\ tun}$
- Thermal emission rates over an interface energy barrier and corresponding thermal emission times between the metal state and the dielectric barrier energy levels for negative charges $\tau_{n\ bar}$ and positive charges $\tau_{p\ bar}$

In addition parasitic capacities including a frequency dependence are considered. Since we have only measured at frequencies lower than 2 MHz we are only able to estimate a lower time limit for some of the involved times (see below).

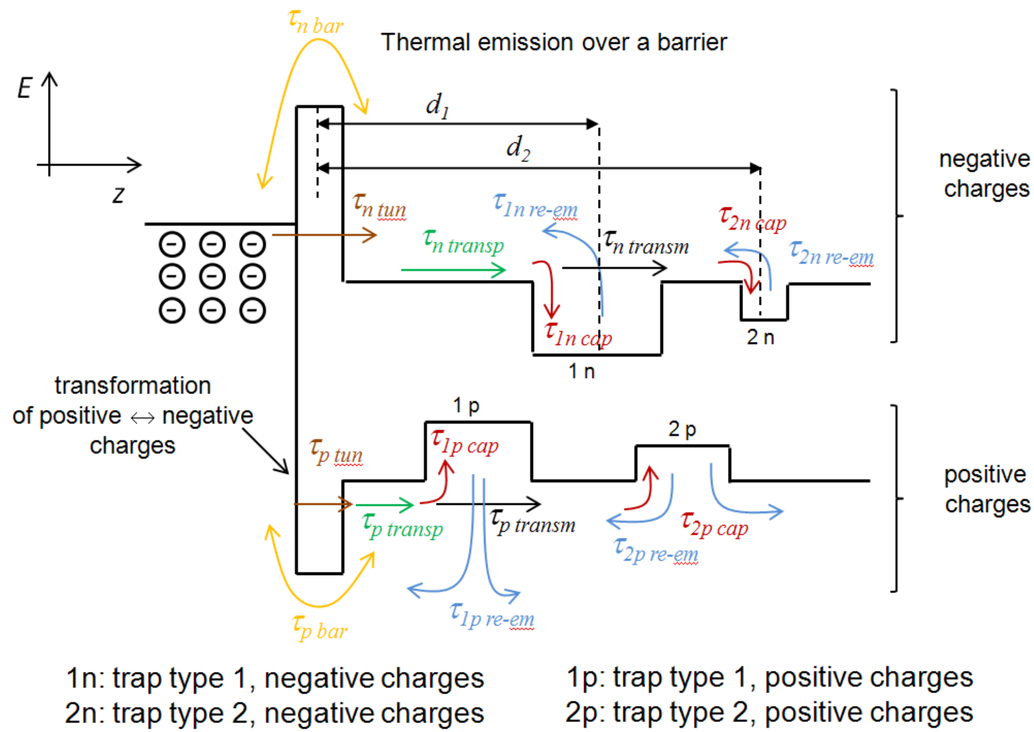

Fig. 5.17. A new model of dynamics of trapping and reemission of charges in dielectric layers of tunable FP filters in a metal/dielectric design.

In the following a preliminary explanation of the experimental data is given, which is based on the rate equation model displayed in Fig. 5.17.

1. Carrier dynamics of electrons and holes in semiconductor micro- and nanostructures have been studied in detail. Disregarding few rare situations in some strained low-dimensional the transfer, capture, tunneling and emission rates of electrons were always higher than those of holes. Although in dielectrics the involved physics are not similar, most probably for negative charges the transport, capture and thermal reemission times will be also here smaller than for positive charges. This is due to the fact that in solids there are no mobile positively charged elementary charges. The dynamics of positive charges is due to a collective action of several electrons. In semiconductors, e.g., the modeling involving holes is elegant but replaces and describes a collective electron dynamics. However, for the preliminary explanation of the experimental AC actuation data is finally not crucial if the dynamics of negative charges is faster than that of the positive charges.
2. In the following a rectangular profile of the AC voltage variation with time is considered. Here, alternatively positive and negative constant voltages of identical time interval are applied. The lengths of these time intervals depend on the frequency.
   2.1 Only for this point 2.1 an alternative model is considered which is based on constant charging currents for the trapping and detrapping. In addition an

AC frequency is considered which is high enough, so that the trapped charges remain always below the maximum possible. That means that no saturation effects are involved. Within this model and for the interval of positive potential on the electrodes, the amount of trapped positive charges increases linearly with time. In the subsequent interval of negative potential on the electrodes, within this model the amount of trapped positive charges decreases again linearly with time. At the same time for the interval of positive potential on the electrodes considered first, the amount of trapped negative charges decreases linearly with time; in the subsequent interval of negative potential on the electrodes considered before, the amount of trapped positive charges increases again linearly with time. In conclusion, after a full period of a single positive and a single negative potential interval exactly the identical charge is trapped compared to the situation before that period. This holds for all four traps (n_1, n_2, p_1 and p_2). This is simple based on the situation of charging and discharging occurring with constant currents. This model would not allow a temporal increase of trapped charges from period to period. Also the inclusion of saturation effects when all possible traps would be occupied would change this situation. In this model the AC voltage amplitude required for desired constant wavelength tuning would not depend on the actuation voltage. This is in contradiction to the experimental observations. For 2 MHz much smaller AC voltage amplitude is required for a constant wavelength tuning compared to 1MHz. Thus, the assumption of situation with constant charging currents for the trapping and detrapping is unrealistic and not compatible with the reality. Therefore, in the next step, a rate equation model is used in section 2.2.

2.2 Within this model automatically "saturation effects" are involved and clearly visible even if the amount of trapped charges does not reach the density of states of the traps. This model considers all four traps (n_1, n_2, p_1 and p_2) in combination with the two electrodes as individual capacities. In the interval of negative potential on the electrode, within this model the amount of trapped negative charges increases exponentially in a saturation profile with time. At the beginning of the interval $|dQ_i/dt|$ is always highest. $|dQ_i/dt|$ decreases continuously with time as it is typical for charging and discharging of capacities, showing profiles $Q_i(t)$ with saturation character. Within this model and for the interval of positive potential on the electrodes, the amount of trapped positive charges also increases exponentially with time. At the same time for the interval of negative potential on the electrodes, the amount of trapped positive charges decreases exponentially with time within a satu-

ration profile; in the subsequent interval of positive potential on the electrodes considered before, the amount of trapped negative charges also decreases again exponentially with time. In conclusion, after a full period of a single positive and a single negative potential interval the total amount of trapped charges is changing compared to the situation before that period. This holds for all four traps (n_1, n_2, p_1 and p_2). In this model the AC voltage amplitude required for desired constant wavelength tuning would depend on the actuation voltage. For higher frequencies, the time interval of a constant polarity is shorter, thus the parts of the transient $Q_i(t)$ profile with much higher $|dQ_i/dt|$ occur than for lower frequencies, where in the transient $Q_i(t)$ profiles also smaller $|dQ_i/dt|$ occur. This nonlinear character in the $Q_i(t)$ profiles allows a continuous increase of the total amount of trapped charges until a saturation value is reached. This value where the trapped charge is saturating depends on the frequency. For higher actuation frequencies a smaller amount of trapped saturated charges results. This saturation value is acting like a "parasitic DC voltage". Note that no DC voltage is applied; the parasitic DC voltage is a result of charging according to the model shown in Fig. 5.17. Thus, the effect of charging of the dielectric materials is smaller for higher actuation frequencies.

3. In the following a **sinusoidal profile of the AC voltage variation** with time is considered. Here, alternatively positive and negative half-periods of identical time interval are involved. The lengths of these time intervals depend on the frequency. The shape of the transient $Q_i(t)$ profiles is quantitatively changing. However, all the scientific statements of section 2.2 remain valid. Also in this model the AC voltage amplitude required for desired constant wavelength tuning would depend on the actuation voltage. For higher frequencies, the time interval of a constant polarity is shorter, thus the parts of the transient $Q_i(t)$ profile with much higher $|dQ_i/dt|$ occur than for lower frequencies, where in the transient $Q_i(t)$ profiles also smaller $|dQ_i/dt|$ occur. This nonlinear character in the $Q_i(t)$ profiles allows a continuous increase of the total amount of trapped charges until a saturation value is reached. This value where the trapped charge is saturating depends on the frequency. For higher actuation frequencies a smaller amount of trapped saturated charges results. This saturation value is acting also here like a "parasitic DC voltage". Note that also here no DC voltage is applied; the parasitic DC voltage is a result of charging according to the model shown in Fig. 5.17. Thus, the effect of charging of the dielectric materials is smaller for higher actuation frequencies. This is in agreement with the experimental observations. For 2 MHz much smaller AC voltage amplitude is required for a desired constant wavelength tuning compared to 1 MHz, since for 2 MHz a

much smaller parasitic DC voltage has to be overcompensated than for an actuation frequency of 1 MHz. Thus, the assumption of the rate equation model "**dynamics of trapping and reemission of charges in dielectrics**" shown in Fig. 5.17 would explain the experimental data. However, further experimental studies are studied for AC actuation accompanied with line shape fittings of the theoretical data to the experimental results.

4. Capacities strongly decrease with growing frequency (in contrast to inductivities which strongly increase with growing frequency). The capacitive character with its basic frequency behavior in addition is most probably involved. The saturation effects due to the nonlinear profiles as mentioned before would not be able to explain such a large difference between 1 MHz and 2 MHz. Note that the experimentally observed difference by much more than a factor of 2 is most probably explainable by the combination of both effects, comparing the AC voltage amplitude which is required for a desired wavelength tuning. In summary the carrier dynamics of the model "**dynamics of trapping and reemission of charges in dielectrics**" shown in Fig. 5.17 together with the frequency dependence, both, qualitatively and in a satisfactory quantitatively would support the obtained experimental data.

The experimental observations can already be explained using the explanations under the sections 3 and 4 within our simple model. However, additional statements are possible and some further alternative scenarios will be introduced:

1. The tunneling times $\tau_{n\ tun}$ and $\tau_{p\ tun}$ are comparable and faster than approximately 100ns. The thermal emission times over the interface energy barriers $\tau_{n\ bar}$ and $\tau_{p\ bar}$ are comparable and faster than approximately 100 ns.
2. Scenario 1 (limit 1): The capture times for negative charges are smaller than those for positive charges and the reemission times are comparable for both charges. This limit is characterized by $\tau_{1n\ cap}$ and $\tau_{2n\ cap} < \tau_{1p\ cap}$ and $\tau_{2p\ cap}$ **.** Furthermore $\tau_{1n\ re\text{-}em}$ and $\tau_{2n\ re\text{-}em} < \tau_{1p\ re\text{-}em}$ and $\tau_{2p\ re\text{-}em}$. We describe this limit as the **"bottle neck effect in hole capture".**
3. Scenario 2 (limit 2): The capture times for positive charges are similar to those for negative charges and the reemission times are comparable for both charges where $\tau_{1n\ cap}$ and $\tau_{2n\ cap} \approx \tau_{1p\ cap}$ and $\tau_{2p\ cap}$ but the reemission times for negative charges are much short than those for positive charges: $\tau_{1n\ re\text{-}em}$ and $\tau_{2n\ re\text{-}em} << \tau_{1p\ re\text{-}em}$ and $\tau_{2p\ re\text{-}em}$. We describe this as the **"bottle neck effect in electron trap population".**

Based on the assumptions that the actuation frequencies of 1 MHz and 2 MHz are above the resonance frequency of the mechanical oscillator (filter structure), there should be nearly no movement of the membranes. Based on our model scenario 1 and 2 the para-

sitic effective net DC bias originating from charging effects depends on the applied AC voltage amplitude and frequency.

In summary: A spectral tuning which increases with increasing applied AC voltage amplitude has been observed (Fig. 5.14 and Fig. 5.15) and can be explained by our preliminary model (sections 3 and 4). Also the difference between Fig. 5.14 and Fig. 5.15 that the required net biasing depends on the actuation frequency can be understood qualitatively. This is also in agreement with the experimental observation at an actuation frequency of 1.4 MHz in which the tuning efficiency is just in between that of the 1 MHz and 2 MHz experiments.

This paragraph describes a brief sketch [109] of our new model “**dynamics of trapping and reemission of charges in dielectrics”** showing many limits among those are the limit of **“bottle neck effect in hole capture”** and the limit of **“bottle neck effect in electron trap population”.** Detailed quantitative investigations are planed and will be performed in the future.

6 Design, implementation and applications of the free beam broad band confocal setup

The compact microscope spectrometer setup (chapter 3.4) as well as the free beam broad band confocal setup (this chapter, 6) have been planed, designed, installed, calibrated and verified within this thesis. The other setups mentioned in chapter 3 were state of the art when this thesis was started.

In the previous chapters, different setups to characterize optical properties and tuning behaviors of FP filter arrays which have been available before this thesis was started were introduced. Each setup itself has some specific advantages and disadvantages. The compact microscope spectrometer setup by far overcomes the drawbacks of the previous ones. However, the microscope[26] is designed to work in the visible range, thus, the functionalities of its internal optical elements in the NIR range is strongly limited. Furthermore, for further requirements of characterization of the FP filter arrays, the microscope spectrometer setup presents a limitation in modifying and implementing new optical elements in the setup. Therefore, it is mandatory to replace the setup by a new one which allows to measure also in the NIR wavelength range, and also provides the high flexibility to modify and add new optical elements in the setup to adapt with future researches.

In this chapter, a new design of a characterization setup called the free beam broad band confocal setup has been developed. The setup not only works effectively in the visible range, but also in the NIR range, thus, it can overcome some of the current drawbacks of the compact microscope spectrometer setup. In the following sections, the setup's construction detail and the acquired experimental results in the visible and NIR range are presented. A complete description of alignment, calibration and verification procedures which are crucial for obtaining reliable results is also included. Finally, in order to validate the setup's accuracy, a comparison of experimental spectra achieved from two setups, the compact microscope spectrometer and the free beam broad band confocal setup, is carried out.

[26] Image Z1m, Carl Zeiss

6.1 Construction details of the free beam broad band confocal setup

Similar to the compact microscope spectrometer setup, the free beam broad band confocal setup consists of four main parts: (i) an illumination system, (ii) a collimation and magnification system, (iii) a sample stage and (iv) a data recording and analysis system. For capturing the top view image of the sample, in addition, the setup is equipped with an imaging system. The construction detail of those main parts is discussed in detail below.

6.1.1 The illumination system of the setup

In spectroscopic studies, HAL lamps are the most common incandescent continuous sources which are generally used in illumination systems. Even though they provide a broad spectra range, their coupling efficiency into an optical fiber is low which often results in a low power at the detectors. In this new approach, a SuperK Extreme Supercontinuum white light laser[27] (SCWLL) is utilized as the illumination system which is described in detail in chapter 2.2.1.2. The laser delivers a very wide spectral output covering from 460 to 2400 nm while still providing a high average power of about 4.3W. The laser output is a single mode Gaussian beam with the beam quality M^2 less than 1.1, and the beam divergence is less than 5 mrad.

6.1.2 The collimation and magnification system of the setup

In order to perform in-situ observations of the optical properties and tuning behaviors of individual FP filters and to combine it with easy handling, it is advantageous to lay the samples (FP filter arrays) on a horizontal plane. (If the sample would be positioned in a vertical plane very complicated fixing elements are required to guarantee a perfect vertical incidence of the beam. This would be time consuming and optically less precise and, thus, of disadvantage). Therefore, it is required to implement the optical axis close to the sample in vertical direction. In this setup, the collimation and magnification system including a mirror and an objective lens is illustrated in Fig. 6.1. The mirror[28] is coated with Aluminum which allows a good compromise in reflecting all the wavelengths in the working range of the SCWLL. The objective lens is a critical part of the characterization setup which is assigned to project a focused beam on the filter membrane. At the beam waist, the wavefront is almost parallel (approx. a plane wave); therefore, the incident beam hits the membrane perpendicularly. Thus, the effect of shifting

---

[27] SuperK Extreme Supercontinuum laser, Koheras

[28] MRA20-G01,Thorlab

into shorter wavelength of the spectrum (mentioned in Fig. 2.22) can be avoided by placing the filter membrane at the focal point of the objective lens.

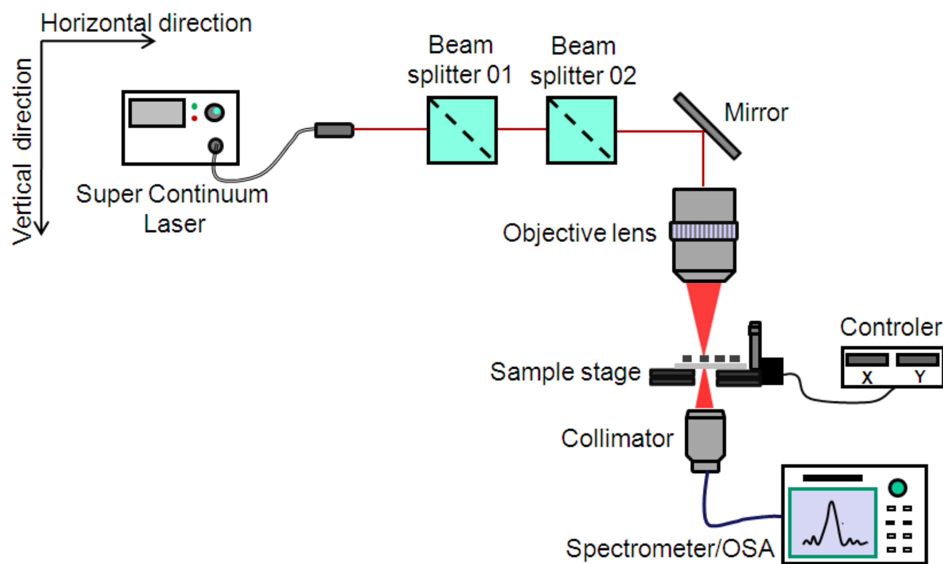

Fig. 6.1. Schematic diagram of the free beam broad band confocal setup for transmission and reflection measurements.

As described before, the membrane's lateral dimension of a FP filter is just ten up to hundred micrometers. The size of the focused light spot which defines the inspected area in an array is required to be less than the membrane dimension. In this setup, a 10 x objective lens from Mitutoyo[29] is implemented due to the adequate features it offers. The objective lens can work efficiently in the visible range as well as in the NIR range, specifically from 480 to 1800 nm, with high transmission efficiency of 80 % in the visible range and 60 % in the NIR range. The working distance of 30.5 mm provides enough space for installing and moving the probing electrodes during the actuation of the tunable filter arrays. The numerical aperture (NA) of the objective lens is 0.26 and it provides a good resolving power. Based on the Rayleigh criterion in chapter 2, the size of the focused light spot is approximately 10 µm. Therefore, theoretically the objective lens allows us to measure the membrane with the smallest diameter of about 10 µm.

In this part, a precise alignment between the mirror and the objective lens is a critical issue. A good alignment is achieved when the reflected light from the mirror strikes the centre of the objective lens. This condition can be solved by using a mechanical prism stage[30] which enables the rotation of the mirror along three axes, and the rotation is rela-

[29] NT46-403 Mitutoyo Objective lens, Edmund Optics

[30] Prism stage 40S, Linos

tive to the optical part of the setup. The objective lens is securely fixed to avoid any mechanical vibration which might occur during the setup in operation.

6.1.3 The data recording and analysis system of the setup

The data recording and analysis system is a combination of a collimator, a grating spectrometer[31] or an OSA (see Fig. 6.1). A collimator is designed to collimate the transmitted or reflected light and coupled into an optical fiber. In this setup, with the use of the SCWLL which can cover nearly a 2000 nm spectral range; there is nearly no optical component that can fully work in such a wide range. Therefore, the whole wavelength range is divided into several narrower ranges which particularly match with different working ranges of FP filter arrays. Based on that, different optical elements which can effectively operate in different wavelength ranges are chosen.

In this case, three different adjustable collimators[32] [33] [34] that can work in a satisfactory way in the visible, NIR range are chosen, respectively. Due to the adjustable function, the central lenses of the collimator can be moved along the optical axis that makes it possible to adjust the distance between the inspected filter and the lenses, between the lens and the tip of the fiber. The maximum translation distance of these collimators is 1.5 mm. This adjustable manipulation leads to an option to find the most appropriate position of the lenses in the collimator where the best coupling efficiency is achieved. Besides the adjustment in vertical direction (z direction), adjusting the collimator in the horizontal direction (xy directions) is also mandatory to control its lateral position with respect to the optical axis. The center of the collimator should be located on the optical axis. This condition helps to eliminate losses during the propagation of light and, thus, increases the coupling efficiency. In order to fulfill this requirement, a collimator positioner[35] which can precisely translate the collimator in x and y direction is required.

The optical fiber in this part can be either a single mode or a multi mode fiber. The multi mode fiber has the advantage of less sensitivity to misalignment during the operation of the setup, however, it also gives rise to undesirable mode jumps between adjacent modes which leads to losses of the power during propagation. Therefore, to overcome this disadvantage of the multimode fibers, a single mode fiber is implemented.

In the development of the free beam broad band confocal setup, an OSA is utilized. The advanced construction of the OSA allows performing a sweep during the measurement.

---

[31] HR2000, Ocean Optics

[32] NIR CFC 11X-B 650-1050 nm, Thorlabs

[33] IR CFC 11X-C 1050-1620 nm, Thorlabs

[34] MB02, Edmund

[35] ST1XY-D-XY Translator, Thorlabs

Here, two OSAs[36] [37] from Yokogawa which cover the range of 350 - 1200 nm and of 1200 - 2400 nm respectively are used to analyze the entire wavelength range that the laser provides. Due to their ability of offering high speed, accurate analysis and variable wavelength resolutions from 0.02 nm to 10 nm, the OSAs can efficiently be organized and adapted to many different characterization situations. Furthermore, they can operate in a very short inspected time which then provides a very fast feedback to the technological fabrication processes.

6.1.4 The sample stage and the imaging system of the setup

The sample stage is an important part of the setup for carrying the filter arrays to be characterized. The purposes of the sample stage can be classified into three main tasks. Firstly, the sample stage is assigned to move the characterized filter arrays on the horizontal directions (xy directions). This movement, together with the imaging system which is described later, helps to scan thoroughly the whole filter arrays, and to select the inspected area. Secondly, the stage is assigned to place the characterized filter arrays at the focal area of the objective lens. The focusing procedure is done by the translation of the stage in the vertical direction (z direction). In addition to horizontal and vertical controlling, it is necessary to control the rotation of the sample stage. This function will ensure that the incident beam always hits the membrane perpendicularly. Therefore, the third task of the sample stage is to adjust yaw and tilt for aligning the filter vertically to the optical axis.

The scheme of the sample stage is illustrated in Fig. 6.2 below. For highly accurate positioning of the filter array, the sample stage is implemented with a xyz translation stage with sub-micron resolution. The stage plane is located vertically with respect to the optical axis. It is laterally motorized and digitally controlled by a controller[38]. The value of one motor step is 0.125 µm which is sufficiently precise enough for all possible movement. For adjusting yaw and tilt, the stage which is in charge for vertical movement is assembled together with a rotation stage[39] which can slightly rotate of a few degrees. A flat platform for laying the sample is then securely mounted to the rotation stage.

---

[36] AQ 6373, Yokogawa

[37] AQ 6375, Yokogawa

[38] 8MT167-125, Standa

[39] R150, Standa

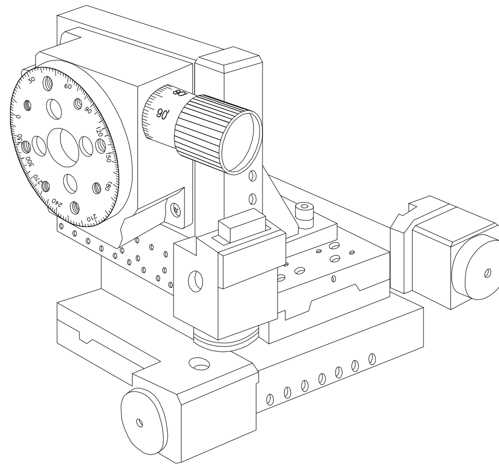

Fig. 6.2. Scheme of the sample stage consisting of a xyz translation stage with sub-micron resolution and a rotation stage.

As compared to the case of the compact microscope spectrometer setup, the sample stage in this case is mounted to the optical setup in a more decoupled way compared to the compact microscope spectrometer setup. For the optical measurement, this configuration reduces the influence from weak vibrations that are produced by the stage during the translation in vertical and horizontal directions. Furthermore, the possibility of rotating is another beneficial factor compared to the compact microscope spectrometer setup. This will help to fulfill the condition that the incident beam always hits the sample surface perpendicularly.

In order to provide the top view image of the filter arrays during the measurement, as well as to position the arrays in the desired location, the setup is equipped with an imaging system. When the setup is in operation, the imaging system together with the collimation and magnifying system help to capture the top view image of the filter arrays. The schematic diagram of the imaging system is depicted in Fig. 6.3.

The imaging system consists of an LED, beam splitters, a tube lens, and a camera. The LED is used as an extra light source to illuminate the sample being measured. Beam splitter 03[40] which typically works in the visible range together with beam splitter 01 or a cold light mirror are assigned to guide the LED light beam to the collimation and magnification system, then finally to project on the sample. Beam splitter 01 or cold light mirror has to fulfill two critical conditions. They must allow the laser beam to transmit through it with high efficiency, and at the same time reflecting the LED light beam to illuminate the filter arrays. In order to operate the system in the visible range,

[40] BS 016, Edmund Optics

beam splitter 01[41] which works efficiently in the range from 400 to 800 nm is utilized. In case of measurements in the NIR range, a cold light mirror[42] is assembled. The cold light mirror is highly reflective in the visible range and highly transmisstive in the NIR range (approx. 90 % of transmittance in the range of 750 nm to 2500 nm). This feature ensures that the cold light mirror transmits the NIR light from the laser while still guiding the visible light from the LED to the collimation and magnification system.

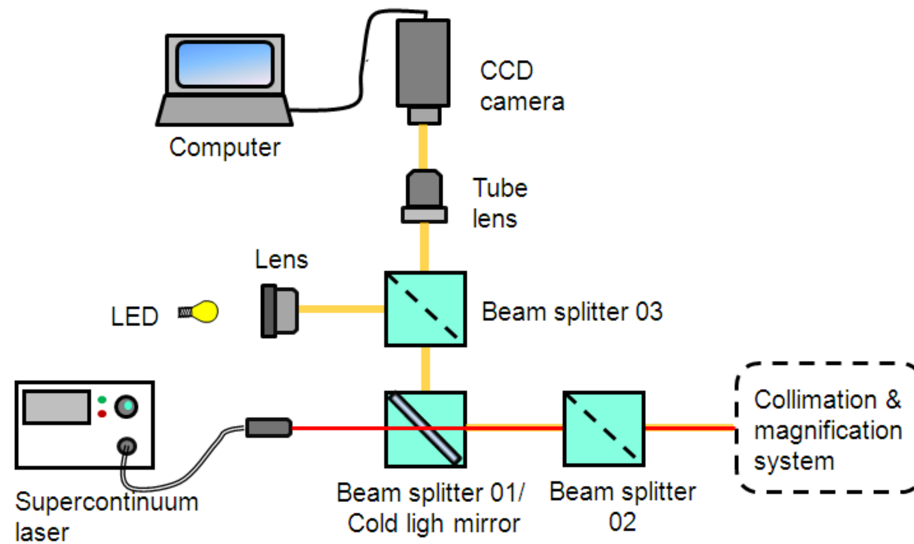

Fig. 6.3. Schematic diagram of the imaging system for visualizing the filter structure being measured.

The tube lens[43] primarily working in the designed range of 430 nm to 650 nm is utilized to create and project an intermediate image of the filter arrays surface on a CCD camera[44]. In any imaging system, providing a real and precise image of a subject is required. Therefore, the orientation of the optical elements is a critical issue that needs to be treated with some cautions. To avoid the distortion of the image generated by misalignment while installing the optical elements, all the beam splitters and cold light mirror are fixed on tilt/rotation stages[45] [46]. These tilt/rotation stages can provide two independent tilt adjustments within ± 5° range and ± 5° in plane rotation adjustment. The

[41] BS 016, Edmund Optics
[42] Cold light mirror KS 93/45, Qioptiq
[43] MT-1, Edmund Optics
[44] RJM JenaCam11
[45] 6PT110 - Tilt / Rotation Stage, Standa
[46] Plattenhalter 0-15mm, Qioptiq

tube lens is hold by an yz positioner[47] to precisely position it in the plane orthogonal to the optical axis.

6.2 Working principle of the free beam broad band confocal setup

In this section, the working principle of the free beam broad band confocal setup in transmission and reflection measurement is described. Additionally, the procedures of calibrating and aligning the setup which are key factors to achieve highly accurate measurements are mentioned in detail.

6.2.1 Working principle of the setup in transmission and reflection measurement

The schematic diagram of the free beam broad band confocal setup which can be operated in both transmission and reflection measurement conditions is illustrated in Fig. 6.4. Due to the broad range of wavelengths, typically from the visible to the NIR range, that the SCWLL provides, different optical elements are utilized to adapt with different working ranges of the FP filter arrays. The light beam from the SCWLL is guided firstly to *beam splitter 01* in case of a measurement in the visible range, or through the cold light mirror in case of a measurement in the NIR range. The light then strikes the mirror of the collimation and magnification system. The mirror reflects the beam downward to the objective lens. After passing through the objective lens, the beam is focused and projected on the filter arrays. In this case, the inspected area is roughly 10 µm which is the size of the focused light area.

[47] 5ZYP - Y-Z Positioner Standa

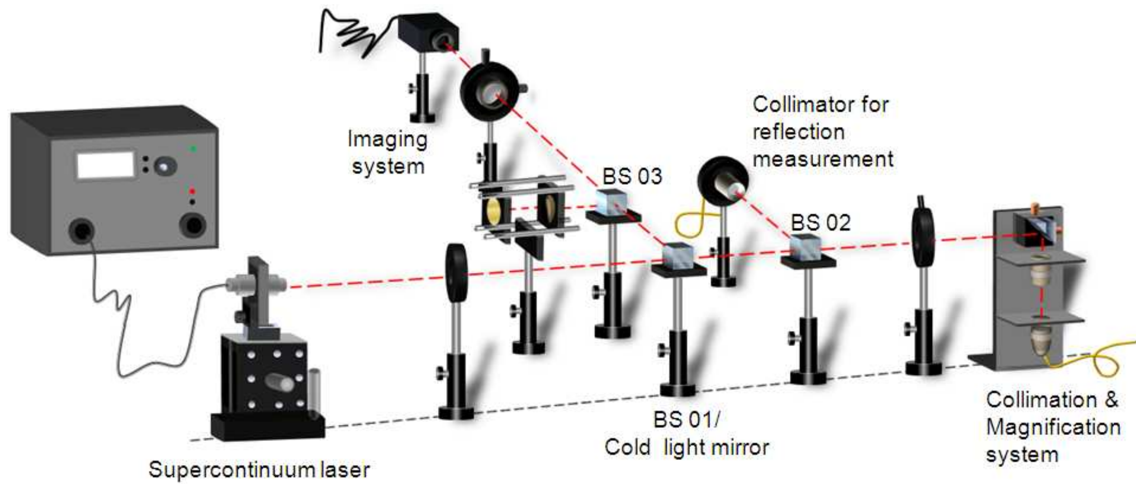

Fig. 6.4. The final assembly of the free beam broad band confocal setup. The setup includes four main parts: the SCWLL as an illumination system, the collimation and magnification system, the imaging system and the sample stage.

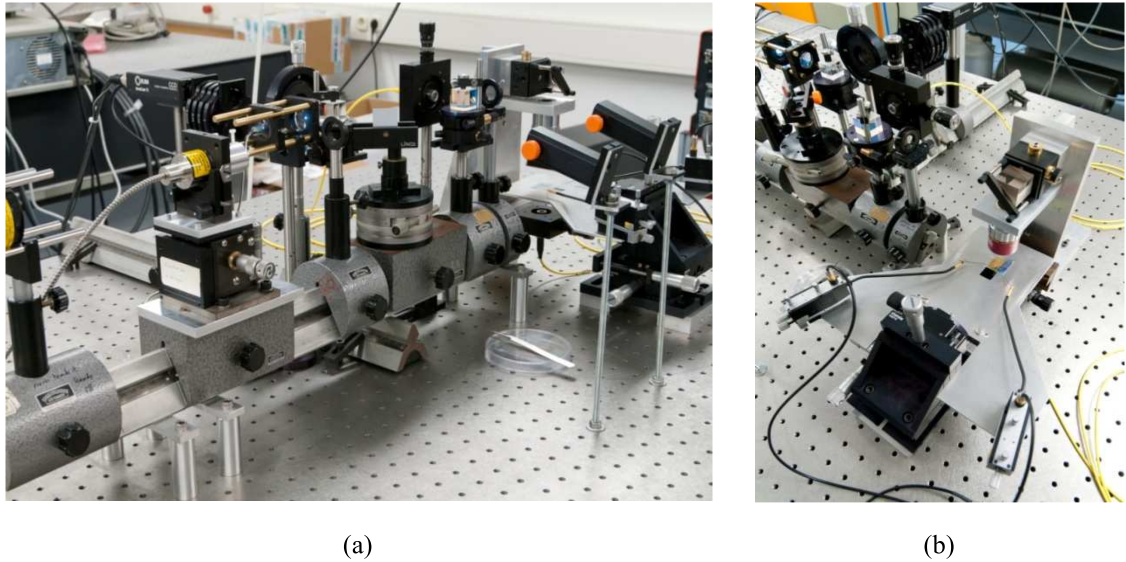

(a) (b)

Fig. 6.5. Side view (a) and top view (b) of the free beam broad band confocal setup.

In case of transmission measurement, the light transmitted through the filter is guided to the condenser and coupled into a single mode optical fiber. The transmission spectrum can be analyzed by a spectrometer or an OSA. In case of reflection measurements, the reflected light travels backward to the objective lens, the mirror, *beam splitter 02,* and finally is coupled into a single mode fiber. In order to scan many different spatial positions, the sample is slightly moved by the motorized translation stage. Thus, different lateral positions that address another individual filter for characterization are quickly reached. This function significantly reduces the total measurement time. For character-

izing micromachined tunable filter arrays, in addition two contact needles[48] are positioned and connected to the top and bottom electrodes of the FP filters. The needle supports are tightly fixed to the sample translation stage. An electrical voltage supply delivers variable voltages for the electrostatic actuation of the tunable filters.

6.2.2 The calibration and alignment procedure of the setup

For every characterization setup, aligning and calibrating the setup are critical issues. In this part, a detailed alignment and characterization procedure will be discussed. Good alignment is reached when a well collimated light beam illuminating the filter arrays is generated. In this setup, the procedure of aligning consists of several steps.

First a position has to be found at which the laser beam strikes the centre of the objective lens. In order to find that position, a wafer whose surface roughness is considered nearly homogeneous is laid on the translation stage. During the calibration process, the prism stage is adjusted for yaw and tilt angles until the reflected light from the wafer returned backward by the objective lens coincides with the incident beam. This configuration ensures that the laser beam strikes the centre of the objective lens.

For reflection calibration, *beam splitter 02* is inserted into the free beam space between the laser source and the collimation and magnification system as illustrated in Fig. 6.4. The position of *beam splitter 02* is slightly adjusted by the tilt/rotation stage so that the incident beam hits the beam splitter’s surface perpendicularly. After a rough geometrical alignment a rather weak light intensity reaches the detector, which we call “first signal”. The “first signal” is be collected by the collimator, and detected by the detector. Afterwards, the position of the collimator for reflection measurement has to be adjusted in lateral and vertical directions until a maximum signal is detected. For the calibration of transmission measurement, the wafer is removed. Then the procedure is repeated similarly to the reflection calibration until the transmission signal is maximum by adjusting the collimator which is in charge for transmission measurement.

The spectrum shown in Fig. 2.21 corresponds to a laser pumping at its maximum. Reducing the pump power strongly modifies the spectral extension of the emission profile as already mentioned. Figure 6.6 shows in black the spectrum of the SCWLL measured with a minimum of optical components. That spectrum is now compared to other spectra measured under different conditions. Here is an overview on all the different situations measured:

(a) Black line: SCWLL + collimator + fiber + OSA
(a) Violet line: SCWLL + cold light mirror + collimator + fiber + OSA

[48] MicroTech

(a) Green line: SCWLL + beam splitter + collimator + fiber + OSA
(b) Petrol line: SCWLL + deflecting mirror + objective + collimator + fiber + OSA

As seen in the figure, the implementations of optical elements in the measurement setup do not have much influence on the shape of the intensity profile. The only impact of the setup on the laser signal is the attenuation of the optical power over the whole measured range. The significant reduction of the optical power obtained at the end is referred to the spectral losses during light propagating through the optical elements and coupling into the single mode fiber.

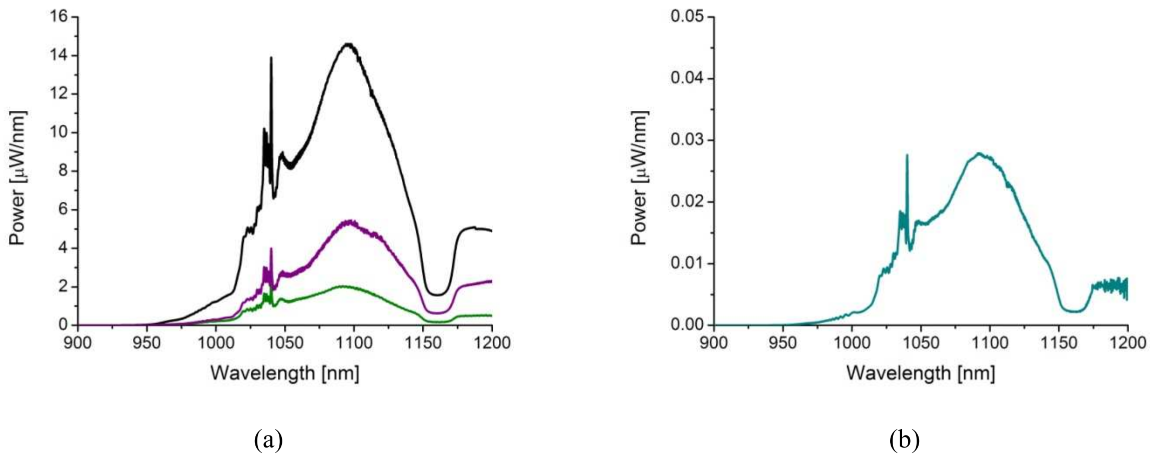

(a) (b)

Fig. 6.6. Spectra of the supercontinuum laser and corresponding spectra under different situations listed in the text.

After the alignment and calibration processes of the setup, the imaging system is treated next. For the imaging system *beam splitter 01* or the cold light mirror and further optical elements of the imaging system are inserted into the optical path. As already discussed before, in order to observe a reliable image of the inspected filter arrays without any distortion, *beam splitter 01* or the cold light mirror needs to be tilted under 45° with respect to the optical axis. Other optical elements of the imaging system are also required to adjust properly until an image of filter arrays is obtained.

The measurement procedure requires several steps. For transmission experiments, the spectral characteristic of the SCWLL is firstly measured using a substrate without filters, identical in material and thickness to those used for FP filter arrays. The obtained spectral intensity profile is used as a *reference spectrum (calibration profile)* of the laser $L_T(\lambda)$. Afterwards, the filter arrays are inserted into the optical path and the spectrum is recorded. Finally, the spectrum measured with the sample is *corrected* using the reference spectrum: the transmission spectrum $T(\lambda)$ is obtained by dividing the spectrum

measured with the sample by the reference spectrum $L_T(\lambda)$. With other words the measured data are subtracted logarithmically from the reference spectrum $L_T(\lambda)$.

6.2.1 Optimum location of the filter sample relative to the optical main path of the setup

After the calibration procedure, the filter arrays are inserted in the optical path of the setup. The optimum location of the filter is indicated as the position where the illuminated beam hits the sample surface perpendicularly. Due to the differences in geometry of the static and tunable filter arrays, the optimum position of the filter in each case is slightly different.

In case of a static filter, the filter membrane is supposed to be flat. Therefore, the optimum position for laying the static filter arrays is the location of the laser beam waist. Because at the beam waist, the wavefront is considered as planar, it has an infinite radius of curvature and this matches best with a flat filter membrane at that point.

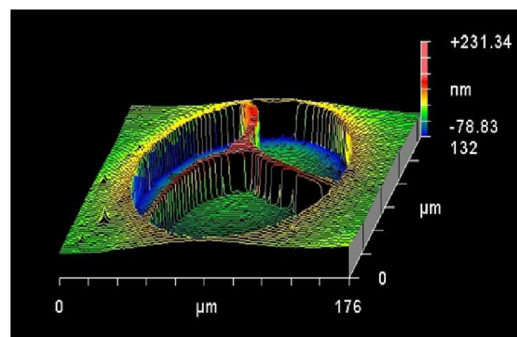

Fig. 6.7. Topographies of a tunable FP filter.

In the case of tunable filters, the residual stress within the membrane causes buckling in the vertical direction, as already mentioned above. The membrane curvature can be considered to be spherical in Fig. 6.7. In order to match the wavefront of the light beam and the curvature of the membrane the filter has to be positioned in a different vertical position compared to the static filter. This is done by placing the membrane at a position where the radii of curvature of the Gaussian beam and the membrane are identical. In order to find the optimum position for the filter membrane, the sample stage is slightly translated in the vertical direction. The optimum position is obtained where the curvature of the filter membrane matches to the radius of the wave front as demonstrated in Fig. 6.8. Experimentally this corresponds to the situation where highest intensities are obtained.

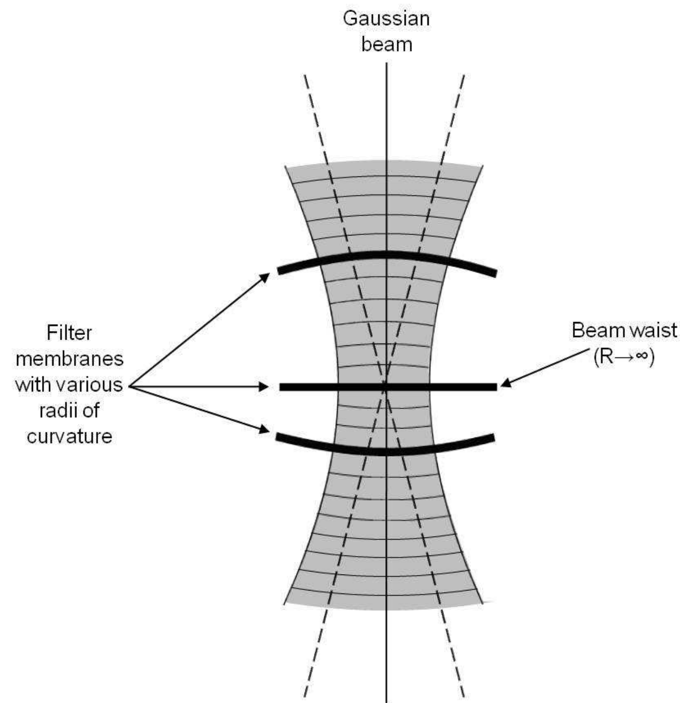

Fig. 6.8. Matching the curvature of the filter membrane to the radius of the wavefront within the Gaussian beam assures that the light hits the filter perpendicularly. A curved filter has to be placed to the top or bottom of the beam waist.

6.3 Experimental results using the free beam broad band confocal setup

Optical characterization of the FP filter arrays obtaining from the free beam confocal setup are the focus of this part. A comparison of spectra between two optical setups: the free beam broad band confocal setup and the compact microscope spectrometer are also included to address the validation of the setups.

6.3.1 Optical characterization of unstructured Fabry Pérot filters

Spectral characterization of an unstructrured FP filter UF2 investigated by the free beam broad band confocal setup is demonstrated in Fig. 6.9. The DBRs are 9.5 periods (19 layers) of Si_3N_4 and SiO_2 deposited by PECVD. In order to achieve optical resonance at a wavelength of 650 nm, the optical height of the cavity can be chosen as $\lambda/2$. The cavity material is mr-UVcur21 and the cavity layers are defined by spin coating (see table 1, chapter 4).

The spectrum shows a stopband of 110 nm in which the filter transmission line occurs at wavelength of 647 nm and shows a transmittance of 50 %. The shift to shorter wavelength of about 5 nm with respect to the design wavelength is probably due to a devia-

tion in cavity height from the design value occurring during the deposition processes. The $FWHM$ of the filter transmission line is 3 nm. As seen from the spectrum, the filter transmission line and the stopband are clearly resolved, thus, the setup can be used for spectral characterization of essential spectral details of the FP filter. In the following parts, the verification of the setup is investigated further by comparing the results with those obtained from other setups.

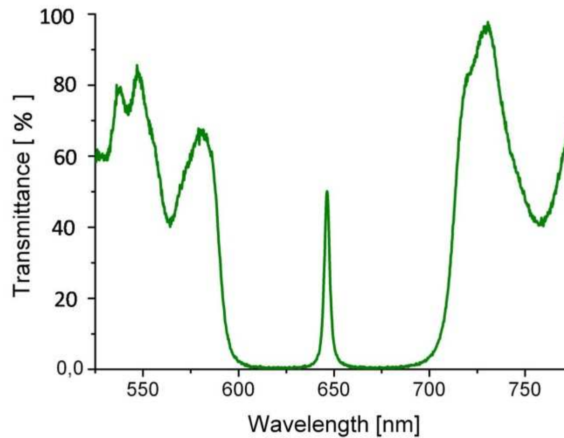

Fig. 6.9. Transmission spectrum of an unstructured FP filter obtained from the free beam broad band confocal setup.

6.3.2 Optical characterization of static Fabry Pérot filter arrays

The configuration of the free beam broad band confocal setup enables the characterization of FP filters with a lateral size of several µm. In this section, different lateral sizes of FP filter are characterized, respectively. The validation of the setup is taken into account by comparing (i) the spectrum obtained from the free beam confocal setup with (ii) the spectrum of the compact microscope spectrometer setup.

Static filter arrays SF3, having 5.5 periods of TiO_2/SiO_2 for top and bottom DBRs and were already characterized by the compact microscope spectrometer, are utilized for a spectral investigation. The filter cavities are defined by 3D NanoImprint technology. The cavity material is the mr-UVcur06 polymer. The lateral size of each FP filter is 100 µm x 100 µm (see table 2, chapter 4). Figure 6.10 (a) illustrates the top view of the characterized filter array. The spectra of four different filters in the array characterized by the free beam confocal setup are shown in Fig. 6.10 (b) (the solid line). Due to the variations in cavity height, the inspected filters present four different filter transmission lines located separated at different spectral positions. The average filter transmittance is about 60 %. The $FWHM$ of the filter transmission lines vary in between 4 and 8 nm.

The broadening of the filter transmission lines at longer wavelengths can be explained when considering the position of the filter lines within the stopband. If the filter transmission line locates close to the edge of the stopband where the reflectivity of the mirror is decreased, the filter linewidth will be broadened according to Eq. 2.11 in chapter 2.1.1.3.

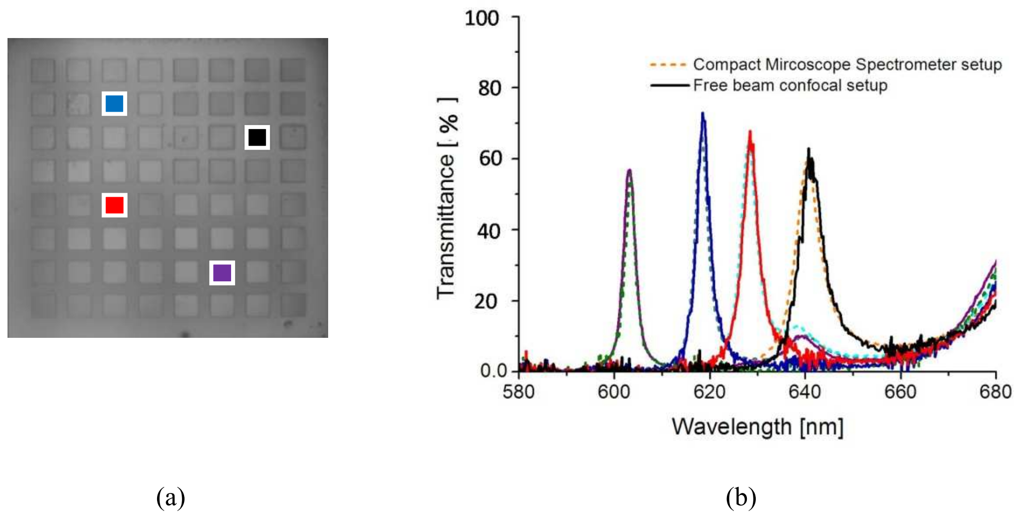

(a) (b)

Fig. 6.10. (a) Top view of the static filter array SF3 indicating the four filters in the arrays characterized, (b) the corresponding spectra of the four characterized filters obtained from the free beam broad band confocal setup (full line) and the microscope spectrometer setup (dashed line).

The measured spectra of the four FP filters obtained by the microscope spectrometer setup (the dashed line) are also included in Fig. 6.10 (b). When comparing the measurement spectra of the two setups, a very good agreement in spectral positions is observed. The small differences in filter transmittance and $FWHM$ are probably due to differences in the inspected positions and inspected area. Note that, the surface is not perfectly homogeneous over the whole membrane [39]. Therefore, if different locations and inspected area within the membrane are chosen to perform spectral characterization, they will result in minor spectral variations. Here, the inspected area of the free beam broad band confocal setup is actually the focused light spot area illuminating the membrane. Theoretically, it is about 10 µm. The compact microscope spectrometer, in contrast, configures the inspected area as the whole membrane which is in this case 100 µm x 100 µm.

Besides the possibility of working in the visible range, the configuration of the free beam confocal setup enables to operate in the NIR range. In order to testify the working function of the setup in longer wavelength range, static filter arrays SF4 that are optimized to work in the NIR range are characterized in the following. The filter arrays in-

clude 6.5 periods of SiO_2/Nb_2O_5 DBRs. So-gel is chosen as a cavity material, and the cavities are also structured by 3D NanoImprint technology. The lateral dimension of each filter is 100 µm x 100 µm. The transmission spectra from four different filters in an array characterized by the setup are illustrated in Fig. 6.11. As seen from the figure, four separated filter transmission lines are observed that prove the capability to operate the setup in the NIR range. The filter transmission lines are spectrally distributed in the range of 900 nm to 1000 nm. The $FWHMs$ vary in between 4.5 nm and 6.8 nm. The filter transmittance is roughly around 60 %. As expected, the differences in filter transmission lines' distributions are derived from the variation in cavity heights in an array. Similarly to the previous cases, the variances in transmittance of the filter transmission lines are partly related to (i) the difference in material absorption at different wavelengths of the DBRs and cavity material, to (ii) non homogeneous DBRs concerning individual layer thicknesses and composition inhomogeneities known as undesired chirping effects and (iii) different spectral position with respect to the design center wavelength.

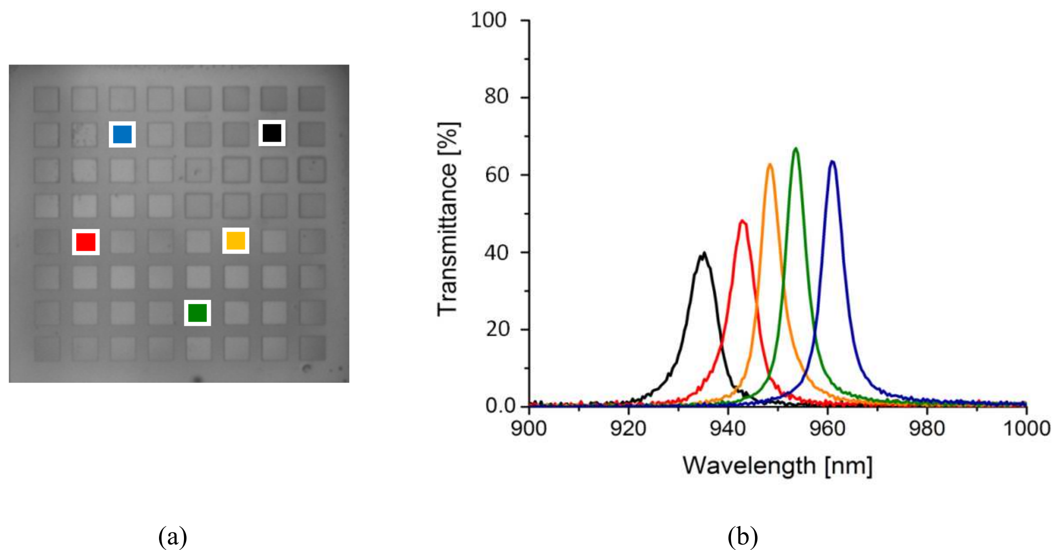

(a) (b)

Fig. 6.11. (a) Top view of the static filter array SF4 and four characterized filters in the arrays, (b) the corresponding spectra of four characterized filters obtained from the free beam broad band confocal setup.

6.3.3 Optical characterization of micromachined tunable Fabry Pérot filter arrays

Besides the spectral investigations of static structures, further investigations of micromachined tunable structures are now taken into account. The tunable FP filter TF4 consist of 9.5 period DBRs of Si_3N_4/SiO_2 and an air gap cavity. The top DBR is mount-

ed by three suspensions. The membrane radius is of 30 µm, the inner radius of 25 µm (see table 3, chapter 4). The desired central wavelength is 650 nm. The laser spot is the inspected area which can be seen as the bright spot in Fig. 6.12 (a). The transmission spectrum of the filter TF4 is presented in Fig. 6.12 (b) (solid line). The spectrum reveals a stopband of about 140 nm (from 575 to 715 nm) and a filter transmission line at 665 nm. The $FWHM$ of the filter achieves a value of 3.1 nm; the transmittance is about 70 %. As already discussed previously, the residual stress causes buckling of the top DBR. This leads to the generation of a spherical geometry of the filter membrane. Hence, for optimum spectral characterization the filter is located in a way that the radii of curvature of the membrane and the wavefront bending of the Gaussian beam are nearly identical.

Again, the validation of the free beam confocal setup is done by comparing this result with the transmission spectra achieved from the microscope spectrometer setup. Obviously, the noticeable resemblances of the stopband, and the position of the filter transmission line demonstrate the reliability of the free beam confocal setup. Similarly, variations in transmittance and $FWHM$ are observed. This can be explained as a consequence of different inspected area, and of different inspected positions being taken on a spherical membrane during the measurement.

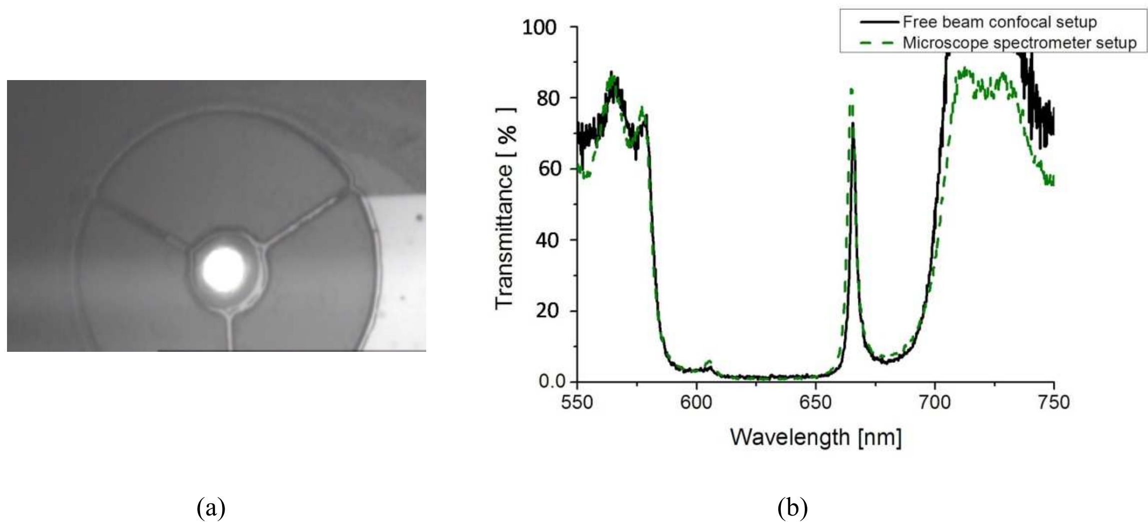

(a) (b)

Fig. 6.12. (a) Top view of the characterized tunable filter TF4, (b) the corresponding spectra of the filter obtained from the free beam broad band confocal setup (full line) and the compact microscope spectrometer setup (dashed line).

7 Conclusion

In this work a new *microscope spectrometer setup* has been started up and a new *free beam broad band confocal setup* has been designed and implemented. Both new setups have been extensively used for various experimental characterizations. Especially optical properties and the tuning behavior of both static and tunable FP filter arrays in the visible and NIR range have been investigated. The setups provide the possibility to measure transmission and reflection spectra of the FP filter arrays in the spectral region of 400 nm to 2400 nm. For some visible and NIR spectral ranges it has been experimentally demonstrated that a reliable accuracy can be obtained.

In the visible range, the compact microscope spectrometer is preferable due to its compact size and simple operation. However, in the case of a characterization in the longer wavelength range, the use of the free beam broad band confocal setup is necessary due to the longer wavelength spectral region it supports.

First the two new setups have been calibrated. The accuracy of the setups is validated by comparing experimental and theoretical spectra while investigating the same FP filters. To evaluate the accuracy of the two new setups in comparison with two existing old setups (Lambda 900 spectrophotometer, Optical bench setup) spectra obtained from the setups are compared. Further validations by comparing the experimental spectra between the setups have been performed. A very good agreement has been obtained in the spectra compared with respect to several spectral parameters such as the stopband width, the spectral position and the $FWHM$ of the filter transmission line, and the transmittance of the filter line. This validation and verification made the users confident that the setups are reliable tools for characterization of optical devices such as: static and micromachined tunable FP filter arrays. The setups allow to measure different dimensions of inspected areas in the micrometer scale with high spatial and spectral resolution. The setup accuracy described above has also been demonstrated and has been used under conditions of high measurement speed. The setups allow for real image monitoring and accurate position addressing of the individual filters to be measured. These features enable a fast quality feedback for the technological fabrication process, identifying weak points in design and technology. Finally this strongly supports to optimize the spectral and mechanical properties of the FP filter arrays so that they can be inserted in the nanospectrometers. Another attractive feature of one of these setups is the opportunity and possibility to replace individual optical components such as objective lenses, collimators, beam splitters, mirrors, etc. to quickly adapt to future requirements of characterization.

The optical and mechanical properties of the static and tunable FP filter arrays have been monitored by the setups, strongly supporting the proof of concept of the FP filter array based nanospectrometer which has been carried out in the last three years. The transmission spectra reveal filter stopband widths of 100 nm up to 200 nm which are defined by the DBR design. Spectrally within the stopband, a filter transmission line which is predefined by the filter cavity height is detected. The transmittances of the static and tunable filters mostly lie in the range of 40 % and 80 %. The $FWHMs$ vary in the range of 3 nm and 12 nm. In case of static filter arrays different cavity heights have been implemented by high vertical resolution 3D NanoImprint technology. The measured spectra reveal numerous filter transmission lines which are clearly visible and distributed in the designed and desired spectral positions within the stopband. The rather high filter transmittances (mostly in the range of 40 % to 80 %), the small filter linewidths (the best $FWHM$ is about 3 nm) and the broad stopband widths (up to 200 nm) denote the remarkable high resolution of the developed 3D NanoImprint technology for the nanospectrometer.

In case of tunable filter arrays, the optical properties and tuning behaviors are investigated, both. By applying a voltage for electrostatic actuation, the achieved spectra demonstrate a spectral tuning of the filter transmission lines. The shift to shorter wavelengths of the filter transmission line is a result of the micromachined actuation, i.e. the decrease of cavity height when the applied voltage is increased. Due to the buckling of the membranes and the change of the membrane geometry during the actuation, the variation in the $FWHM$, filter line transmittance and filter resolution $\mathfrak{R}$ are also observed and discussed. During actuation, a better filter resolution $\mathfrak{R}$ is obtained if the radius of the membrane sphere and that of the beam wavefront are identical. Under this condition, the tunable filters behave as stable resonators indicating the high confinement of light within the cavity. In addition, the electrostatic tuning properties are investigated by the implementation of two kinds of experimental conditions concerning constant or temporally oscillating bias voltages: DC or AC actuation. In case of AC actuation and electrostatic actuation frequencies well above the resonance frequency, the experimental results reveal a better efficiency of electrostatic actuation (lower voltages required) and a better mechanical temporal stability of the tunable filter. The best results are obtained with only 0.6 V when an electrostatic actuation frequency of 2 MHz is applied.

In summary, this work presents two optical characterization setups for characterizing the optical properties and tuning behaviors of static and tunable FP filter arrays in the visible and the NIR range with high spectral quality. Finally a future perspective is given. The setups will allow in the future interesting studies on an advanced AC electrostatic tuning, on thermal as well as acoustic noise and on resonance frequency engineer-

ing. Another point of future interest might be the spectral behavior with respect to thermal properties of both static and tunable FP filter arrays. As a continuance of this work, the setups are accurate enough to study in detail the thermal sensitivity of the FP filter arrays. For an application in naospectrometers it is crucial to know precisely the amount of spectral shift of the filter transmission lines with increasing ambient temperature. Another main goal of the future work is to upgrade the characterization setups enabling an operation in the UV spectral range. This would allow addressing interesting applications of the FP filter arrays and of the corresponding nanospectrometers in the UV range with high spectral quality. Regarding the medical field and other applications, smart sensors thus would be able to detect biomarkers, trace gases or process markers in the UV, visible and IR range. Hopefully this helps to diagnose diseases and detect characteristic biomarkers in a transcutaneous, a non-invasive and a user-friendly way. Most important for the social and economic success of the networked sensing systems is a strong miniaturization of the optical sensors, a cheap production and a long sensor lifetime. The sensor arrays presented would allow redundancy and in future perspective hopefully also self-learning features.

Bibliography

[1]. C.Y.Chong, S.P.Kumar, *Evolution, opportunities, and challenges*, in *Proceeding of the IEEE* 2003. p. 1247.

[2]. R.Narayanaswamy, O.S.Wolfbeis, *Optical Sensors: Industrial, Environmental and Diagnostic Applications* 2004: Springer.

[3]. C.Y.Chong, S.P.Kumar, *Sensor networks: Evolution, opportunities, and challenges*, in *Proceedings of the IEEE* 2003. p. 1247.

[4]. T.V.Dinh, B.M.Cullum, D.L.Stokes, *Nanosensors and biochips: frontiers in biomolecular diagnostics.* Sensors and Actuators B, 2001. **74**: p. 2.

[5]. G.W.Hunter, *Smart sensor systems for human health breath monitoring applications.* J. Breath Res. , 2011. **5**: p. 037111.

[6]. G.V.G Baranoski, A Krishnaswamy, *An Introduction to Light Interaction with Human Skin.* RITA, 2004. **11**: p. 1.

[7]. E.Angelopoulou, *The Reflectance Spectrum of Human Skin.* Technical Report 1999. **MS-CIS-99-29**.

[8]. M.Friebel, M.Meinke, *Determination of the complex refractive index of higly concentrated haemoglobin solutions using transmittance and reflectance measurements.* J. Biomedical Optics, 2005. **10**: p. 064019.

[9]. R.Crocombe. *Miniature optical spectrometers: The art of the possible, part iv: New near-infrared technologies and spectrometers*. 2009; Available from: http://spectroscopyonline.f ndanalytichem.com/spectroscopy/.

[10]. J.Correia, M.Bartek, R.F.Woffenbuttel, *High-Selectivity Single-Chip Spectrometer for Operation at Visible Wavelengths*, in *International Electron Devices Meeting* 1998. p. 467.

[11]. S.W.Wang, M.Li, C.S. Xia, H.Q.Wang, X.S.Chen, W.Lu, *128 channels of integrated filter array rapidly fabricated by using combinatorial deposition technique.* Appl. Phys. B, 2007. **88**: p. 281.

[12]. R.F.Wolffenbuttel, *State-of-the-art in integrated optical microspectrometers, Instrumentation and Measurement.* IEEE Trans, 2004. **53**: p. 197.

[13]. R.F.Wolffenbuttel, *MEMS-based optical mini- and microspectrometers for the visible and infrared spectral range.* J. Micromechanics and Microengineering, 2005. **15**: p. 145.

[14]. S.Wang, C.Xia, X.Chen, W.Lu, M.Li, H.Wang, W.Zheng, T.Zhang, *Concept of a high resolution miniature spectrometer using an integrated filter array.* Optics Letter 2007. **32**: p. 632.

[15]. J.H.Correia, G.De Graaf, S.H.Kong, M.Bartek, R.F.Wolffenbuttel, *Single chip CMOS optical microspectrometer.* Sensors and Actuators A: Physical, 2000. **82**: p. 191.

[16]. G.Lammel, S.Schweizer, S.Schiesser, P.Renaud, *Tunable Optical Filter of Porous Silicon as Key Component for a MEMS Spectrometer.* Journal of microelectromechanical systems, 2002. **11**(6): p. 815.

[17]. H.Hillmer, *Optisches Filter und Verfahren zu seiner Herstellung*, in *Patent application 2006, Offenlegung 2008 DE 10 2006 039 071 A1, Germany, WO 2008/017490 A2*: International. *Granted 19.04.2012*.

[18]. M.Bartels, S.Wittzack, X.Wang, H.Hillmer, *Ultra-precise Nano Imprint template.* Nanos, 2008. **03.08**: p. 18.

[19]. M.Bartels, S.Wittzack, F.Köhler, X.Wang, A.Albrecht, S.Schudy, M.Engenhorst, H.H.Mai, O.Setyawati, T.Woit, C.Woidt, H.Hillmer, *High Vertical Resolution 3D Nanoimprint Technology for Nanophotonic Applications*, in *IEEE/LEOS International Conference on Optical MEMS and Nanophotonics* 2009. p. 87.

[20]. X.Wang, A.Albrecht, S.Schudy, T.Woit, V.Daneker, K.Schultz, H.H.Mai, F.Köhler, S.Wittzack, M.Bartels, H.Hillmer, *High-resolution, Low-cost Microsensors for Networked Sensing Systems: Optical Nanospectrometers with Nanoimprinted Cavities of Filter Arrays*, in *IEEE Technical Digest INSS* 2010. p. 171.

[21]. A.Albrecht, X.Wang, H.H.Mai, T.Schotzko, I.Memon, M.Bartels, M.Hornung, H.Hillmer, *High vertical resolution 3D NanoImprint Technology and its application in optical nanosensors.* J. Nonlinear Optics and Quantum Optics, 2012. **43**: p. 339.

[22]. H.H.Mai, A.Albrecht, C. Woidt, X.Wang, V.Daneker, O.Setyawati, T.Woit, K.Schultz, M.Bartels, H.Hillmer, *3D NanoImprinted Fabry-Pérot filter arrays and methodologies for optical characterization.* Appl. Phys.B, 2012. **107**(3): p. 755.

[23]. A.Albrecht, H.H.Mai, V.Daneker, X.Wang, S.Schudy, T.Woit, K.Schultz, C.Woidt, O.Setyawati, F.Köhler, S.Wittzack, M.Engenhorst, M.Bartels, H.Hillmer. *Optical Characterization of High-Resolution Optical Nanospectrometers for Networked Sensing Systems*. in *IEEE Technical Digest INSS*. 2010.

[24]. C.Woidt, O.Setyawati, A.Albrecht, M.Engenhorst, V.Daneker, T.Woit, S.Wittzack, F.Köhler, H.H.Mai, M.Bartels, H.Hillmer, *Nanotechnological Basis for Advanced Sensors* 2011: Springer.

[25]. L.J.Guo, *Nanoimprint Lithography: Methods and Material Requirements.* Adv. mater. , 2007. **19**: p. 495.

[26]. M.Colburn, *Step and Flash Imprint Lithography: A New Approach to High-Resolution Patterning*, in *Proc. SPIE* 1999. p. 379.

[27]. Y.Xia, G.M.Whitesides, *Soft lithography.* Annu. Rev. Mater. Sci, 1998. **28**: p. 153.

[28]. R.F.Pease, S.Y.Chou, *Lithography and Other Patterning Techniques for Future Electronics*, in *Proceedings of the IEEE* 2008. p. 248.

[29]. H.Schift, *Nanoimprint lithography: An old story in modern times? A review.* J. Vac. Sci. Technol. B., 2008. **26**: p. 458.

[30]. H.A.Macleod, *Thin-Film Optical Filters* 2001: Taylor & Francis.

[31]. M.Born, E.Wolf, *Principles of optics: electromagnetic theory of propagation, interference and diffraction of light* 1964: Oxford, Pergamon Press.

[32]. Y.Wang, *Model Calculations and Implementation of Filters and Hybrid Green VCSELs based on Optical Thin Film Stacks*, in *Department of Electrical Engineering/ Informatics*, PhD thesis 2010: Uni Kassel Press.

[33]. Kusserow, T., *Periodic InP-Air Structures in Optical Devices*, in *Department of Electrical Engineering/ Informatics*, PhD thesis 2010: Uni Kassel Press.

[34]. S.O.Kasap, *Optoelectronics and Photonics* 2011: Englewood Cliffs, NJ: Prentice- Hall 27-29.

[35]. T.A.Kwa, R.F.Wolffenbuttel, *Integrated grating/detector array fabricated in silicon using micromachining techniques.* Sensors and Actuators A, 1992. **31**: p. 259.

[36]. S.H.Kong, D.D.L.Wijngaards, R.F.Wolffenbuttel, *Infrared micro-spectrometer based on a diffraction grating.* Sensors and Actuators A, 2001. **92**: p. 88-95.

[37]. X.Wang, A.Albrecht, T.Woit, M.Bartels, H.H.Mai, S.Schudy, V.Daneker, K.Schultz, F.Köhler, S.Wittzack, C.Sandhagen, W.Köcher, H.Hillmer, *High Resolution 3D Nanoimprint Technology and its Application in Optical Sensors and Photonic Devices.* Technical Digest of NNT '10, 2010.

[38]. S.Y.Chou, P.R.Krauss, P.J.Renstrom, *Imprint of sub-25 nm vias and trenches in polymers.* Appl. Phys. Lett, 1995. **67**: p. 3134.

[39]. X.Wang, *High Resolution 3D Nanoimprint Technology: Template Fabrication, Application in Fabry-Pérot-filter-based Nanospectrometers* in *Department of Electrical Engineering/ Informatics* 2010, Uni Kassel Press.

[40]. X. Wang, M. Bartels, F.Köhler, S.Wittzack, A.Albrecht, H.H.Mai, T.Woit, S.Schudy, M.Engenhorst, C.Woidt, K.Schulz, H.Hillmer, *High Vertical Resolution 3D Nanoimprint Templates.* Technical Digest of NNT09, 2009.

[41]. A.Tarraf, *Low-Cost Micromechanically Tunable Optical Devices: Strained Resonator Engineering, Technological Implementation and Characterization*, in *Department of Electrical Engineering/ Informatics*, PhD Thesis 2005: Uni Kassel Press.

[42]. S.Irmer, J.Daleiden, V.Rangelov, C.Prott, F.Römer, M.Strassner, A.Tarraf, H.Hillmer, *Ultralow Biased Widely Continuously Tunable Fabry–Pérot Filter.* IEEE Photonics Technology Letters, 2003. **15**(3): p. 434.

[43]. S.Irmer, *Air gap Based Vertical Cavity Micro Opto Electro Mechanical Fabry Perot Filters*, in *Department of Electrical Engineering/ Informatics* 2005: Uni Kassel Press.

[44]. O.Setyawati, *MEMS-based Tunable Optical Filter Arrays for Nano-Spectrometer in the Visible Spectral Range*, in *Department of Electrical Engineering/ Informatics*, PhD thesis 2012, Uni Kassel.

[45]. O.Setyawati, H.H.Mai, C.Woidt, S.Schudy, M.Engenhorst, S.Wittzack, F.Köhler, M.Bartels, H.Hillmer, *Low-Cost Micromachined Tunable Fabry-Pérot*

Filters for Optical Nano Sensor Arrays, in *Microoptics Conference (MOC)* 2010. p. 64.

[46]. F.Römer, *Charakterisierung und Simulation optischer Eigenschaften von mikromechanisch abstimmbaren Filterbauelementen* in *Department of Electrical Engineering/ Informatics*, PhD Thesis 2005, Kassel: Uni Kassel Press.

[47]. E.O.Ataro, *Micro-electromechanical Structural Design and Optimization of Vertical Cavity Photonic Devices with Wide Continuous Tuning*, in *Department of Electrical Engineering/ Informatics*, PhD thesis 2005: Uni Kassel Press.

[48]. F.Römer, C.Prott, S.Irmer, J.Daleiden, A.Tarraf, H.Hillmer, M.Strassner, *Tuning efficiency and linewidth of electrostatically actuated multiple air-gap filters.* Appl. Phys. Lett., 2003. **82**: p. 176.

[49]. S.Afrang, *Design and Simulation of Simple and Varying Section Cantilever and Fixed-Fixed End Types MEMS Switches.* ICSE 2004 Proc. IEEE, 2004: p. 593.

[50]. T.A.Bui, *Simulation of Tunable Fabry-Pérot Filters using the Finite Element Method*, in *Department of Electrical Engineering/ Informatics*, Master thesis 2011: Uni Kassel Press.

[51]. M.F.M.Marquez, *Characterization of Filter Design for Nanospectrometer*, in *Department of Electrical Engineering/ Informatics*, Master thesis 2011: Uni Kassel Press.

[52]. L.P.Schuler, J.S.Milne, J.M.Dell, L.Faraone, *MEMS-based microspectrometer technologies for NIR and MIR wavelengths.* Journal of Physics D: Applied Physics, 2009. **42**: p. 133001.

[53]. H.H.Mai, O.Setyawati, V.Daneker, C.Woidt, T.Woit, K.Schultz, S.Schudy, M. Engenhorst, X. Wang, S. Wittzack, F. Köhler, A. Albrecht, M. Bartels, H.Hillmer, *Verification and calibration of spectral properties of high-resolution nano sensor arrays using microscope spectrometers*, in *Microoptics Conference (MOC)* 2010: Taiwan. p. 22.

[54]. J.E.Huber, Z.A.Fleck, M.F.Ashby, *The selection of mechanical actuators based on performance indices*, in *Proc R Soc London Ser A* 1997. p. 2185.

[55]. S.A.Zhou, *On forces in microelectromechanical systems.* International Journal of Engineering Science 2003. **41**: p. 313.

[56]. H.Hillmer, J.Daleiden, C.Prott, F.Römer, S.Irmer, V.Rangelov, A.Tarraf, S.Schüler, M.Strassner, *Potential for micromachined actuation of ultra-wide continuously tunable optoelectronic devices.* Applied Physics B: Lasers and Optics, 2002. **75**: p. 3.

[57]. L.A.Rocha, E.Cretu, R.F.Wolffenbuttel, *Full characterization of pull-in single-sided clamped beams.* Sensors and Actuators A 2004. **110**: p. 301.

[58]. W.M.Zhang, G.Meng, D.Chen, *Nonlinearity and Reliability of Electrostatically Actuated MEMS Devices.* Sensors, 2007. **7**: p. 760.

[59]. A.M.Kärkkäinen, *MEMS based voltage references*, PhD Thesis 2006: University of Technology Helsinki

[60]. A.Karkkainen, *MEMS-based AC voltage reference.* IEEE Transactions on Instrumentation and Measurement, 2005. **54**: p. 595.

[61]. W.C.Tang, M.G.Lim, R.T.Howe, *Electrostatic comb drive levitation and control method.* J. Microelectromech. Syst. , 1992. **1**: p. 170.

[62]. A.Kärkkäinen, A.Oja, J.Kyynäräinen, H.Kuisma, H. Seppä, *Stability of Electrostatic Actuation of MEMS.* Physica Scripta. , 2004. **T114**: p. 193.

[63]. M.Blomberg, H.Kattelus, A.Miranto, *Electrically tunable surface micromachined Fabry–Perot interferometer for visible light.* Sensors and Actuators A 2010. **162**: p. 184.

[64]. L.Castaner, J.Pons, R.Nadal-Guardia, A.Rodriguez, *Analysis of the extended operation range of electrostatic actuators by current pulse drive.* Sensors and Actuators A, 2001. **90**: p. 181.

[65]. J.Zhang, J.Y.Sun, Z.H.Zhang, Y.Zhu, *Effects of dielectric charging on MEMS-based grating light modulator.* Microsystem Technologies, 2009. **15**: p. 745.

[66]. J.Wibbeler, G.Pfeifer, M.Hietschold *Parasitic charging of dielectric surfaces in capacitive microelectromechanical systems (MEMS).* Sensors and Actuators A, 1998. **71**: p. 74.

[67]. R.Kane, H.Sell *Revolution in Lamps: A Chronicle of 50 Years of Progress* 2002: Fairmont Press.

[68]. *Carl Zeiss Online Campus site.* [cited 2011 27.Nov]; Available from: http://zeiss-campus.magnet.fsu.edu/articles/lightsources/tungstenhalogen.html.

[69]. M.J.Weber, *Handbook of laser Laser Science & Technology.* CRC, New York, 2001.

[70]. *Handbook of Laser and Optics*, ed. Träger. Vol. 72. 2007: Springer.

[71]. *Tunable laser handbook*, ed. S.J.Duarte 1995: Academic Press.

[72]. R.R.Alfano, *The Supercontinuum Laser Source Fundamentals with Updated References* 2006: Springer.

[73]. *Koheras Super K EXW.* [cited 2012 30. March]; Available from: http://www.nktphotonics.com/superk_extreme_specifications?cid=7856.

[74]. K.P.Hansen, R.E.Kristiansen. *Supercontinuum Generation in Photonics Crystal Fibers*. 2007; Available from: http://cvitae.org/images/stories64/Supercontinuum%20-%20General.pdf.

[75]. R.R.Alfano, S.L.Shapiro, *Emission in the region 4000 to 7000 a via four photon coupling in glass.* Phys. Rev. Lett, 1970. **24**: p. 584.

[76]. W.Yu, *Spectral broadening of picosecond 1.06 μm pulse in KBr.* Opt. Commun., 1975. **14**: p. 344.

[77]. R.L.Fork, *Femtosecond white-light continuum pulses.* Opt. Lett., 1983. **8**: p. 1.

[78]. P.B.Corkum, C.Rolland, T.R.Srinivasan, *Supercontinuum Generation in Gases.* Phys. Rev. Lett. , 1986. **57**: p. 2268.

[79]. A.M.Zheltikov, *Let there be white light: supercontinuum generation by ultrashort laser pulses.* Phys.-Usp, 2006 **49**: p. 605.

[80]. R.H.Stolen, C.Lin, *New nanosecond continuum for excited-state spectroscopy.* Appl. Phys. Lett. , 1976. **28**: p. 216.

[81]. J.K.Ranka, R.S.Windeler, A.J.Stentz, *Visible continuum generation in air-silica microstructure optical fibers with anomalous dispersion at 800 nm.* Optics Letters, 2000. **25**: p. 25.

[82]. J.Herrmann, U.Griebner, N.Zhavoronkov, A.Husakou, D.Nickel, J.C.Knight, W.J.Wadsworth, P.St.J.Russell, G.Korn, *Experimental Evidence for Supercontinuum Generation by Fission of Higher-Order Solitons in Photonic Fibers.* Phys. Rev. Lett., 2002. **88**(17): p. 173901-1.

[83]. S.M.Kobtsev, S.V.Kukarin, N.V.Fateev, S.V.Smirnov, *Generation of Self-Frequency-Shifted Solitons in Tapered Fibers in the Presence of Femtosecond Pumping.* Laser Physics, 2004. **14**(5): p. 748.

[84]. M.Tiwari, V.Janyani, *Supercontinuum Generation and Optimisation in Nonlinear Photonic Crystal Fibres*, in *2nd International Conference on Computer and Network Technology* 2010. p. 606.

[85]. K.Sakamaki, M.Nakao, *Soliton Induced Supercontinuum Generation in Photonic Crystal Fiber.* IEEE Journal of selected toptics in Quantum Electronics, 2004. **10**(5): p. 876.

[86]. A.V.Husakou, J.Herrmann, *Supercontinuum Generation of Higher-Order Solitons by Fission in Photonic Crystal Fibers.* Phys. Rev. Lett., 2001. **87**(20): p. 203901-1.

[87]. J.Herrmann, U.Griebner, N.Zhavoronkov, *Experimental Evidence for Supercontinuum Generation by Fission of Higher-Order Solitons in Photonic Fibers.* Phys. Rev. Lett., 2002. **88**(17): p. 3901.

[88]. D.Hohlfeld, *Silicon-based Tunable Optical Filters*, PhD thesis 2005, Albert-Ludwigs Universität Freiburg.

[89]. W.Singer, M.Totzek, H.Gross, *Handbook of Optical Systems*, ed. H.Gross. Vol. 2. 2005: Wiley.VCH.

[90]. J.F.James, *Spectrograph design fundamentals* 2007: Cambridge University Press.

[91]. M.W.Davidson, M.Abramowitz. *Optical Microscopy*. Available from: http://www.olympusmicro.com/primer/microscopy.pdf.

[92]. M.Bass, E.W.V.Stryland, D.R.Williams, W.L.Wolfe, *Handbook of Optics: Devices, Measurements, and Properties* 2ed 1994: Optical Society of America.

[93]. D.Halliday, R.Resnick, J.Walker, *Fundamental of Physics*. Vol. 8. 2008: John Wiley & Sons.

[94]. P.Martin. SPECTROMETERS: Microspectrophotometers take a closer look Available from: http://www.laserfocusworld.com/articles/print/volume-47/issue-8/features/spectrometers-microspectrophotometers-take-a-closer-look.html.

[95]. A.Köhler, *New Method of Illimination for Phomicrographical Purposes.* Journal of the Royal Microscopical Society 1894. **14**: p. 261.

[96]. M.Young, *Optics and Laser* 5ed 2000: Springer.

[97]. C.Palmer, *Diffraction grating* 2005: Newport Corporation.

[98]. D.A.Skoog, D.M.West, *Principle of instrumental analysis* 2ed 1980: Brooks/Cole Pub Co.

[99]. T.Mori, T.Kaneko, M.Kojima, *Double pass monochromator*, 1999: United States Patent.

[100]. E.Brinkmeyer, W.Brennecke, R.J.W.Otto, *Polarization scrambler*, 1990: United States Patent.

[101]. K.R.Wildnauer, J.R.Stimple, J.D.Knight, J.N.West, B.G.Broome, *Optical spectrum analyzer having double pass monochromator*, 1991: United States Patent.

[102]. T. Mori, G.Ishihara, T. Kaneko, A.Horiguchi, *AQ6375 Optical spectrum analyzer for long wavelength band.* Yokogawa Technical Report, 2008. **45**.

[103]. R.T.Blunt, *White Light Interferometer - A production worthy technique for measuring surface roughness on semiconductor wafers*, in *CS Mantech Conference* 2006. p. 59.

[104]. C.O'mahony, M.Hill, M.Brunet, R.Duane, A.Mathewson, *Characterization of micromechanical structures using white-light interferometry.* Meas. Sci. Technol., 2003. **14**: p. 1807.

[105]. S.C.H.Thian, W.Feng, Y.S.Wong, J.Y.H.Fuh, H.T.Loh, K.H.Tee, Y.Tang, L.Lu, *Dimensional measurement of 3D microstruture based on white light interferometer.* J. Phys.: Conf. Ser. , 2006. **48**: p. 1435.

[106]. *LAMBDA 800 UV/VIS and 900 UV/VIS/NIR Spectrophotometer System*. 2012; Available from: http://www.surplusserver.com/PDF/Lambda800_900_Brochure.pdf.

[107]. J.Sonksen, *"Sensor Process and Device for Determining a Physical Value" A Proof of Concept*, in *Department of Electrical Engineering/ Informatics*, PhD thesis 2010: Uni Kassel Press.

[108]. B.E.A.Saleh, M.C.Teich, *Fundamentals of Photonics*1991: John Wiley & Sons, Inc.

[109]. H.Hillmer, private communication, July 2012.

[110]. H.Hillmer, *Ambipolar carrier transport in semiconductor heterostructures*, PhD thesis 1989, University of Stuttgart.

[111]. H.Hillmer, S.Marcinkevicius, *Optically detected carrier transport in III/V semiconductor QW structures: experiments, model calculations and applications in fast 1.55 µm laser devices* Applied Physics B: Lasers and Optics, 1998. **66**: p. 1.

[112]. A.Khubodenko, V.Y.Panchenko, V.N.Seminogov, *Fabrication of submicron relief gratings in p-GaAs in the process of maskless holographic wet etching by laser-induced etch rate reduction method.* SPIE proceedings, 1995. **2403**: p. 409.

[113]. H.R.Shea, A.Gasparyan, H.B.Chan, S.Arney, R.E.Frahm, D.López, S.Jin, R.P.Mcconnell, *Effects of Electrical Leakage Currents on MEMS Reliability and Performance.* IEEE Transactions on device and materials reliability, 2004. **4**: p. 198.

List of tables

Table 1. Geometrical parameters of the characterized unstructured FP filters……..…65

Table 2. Geometrical parameters of the characterized static FP filters and arrays……66

Table 3. Geometrical parameters of the characterized micomachined tunable FP filters…………………………………………………….…………………………..68

Table 4. Comparision of resolving power of five filter transmissions lines corresponding to five applied voltages……………………………………………………..….77

List of figures

Fig. 2.1. Reflection and transmission of incident light on many alternating high and low refractive index layers. 6

Fig. 2.2. Reflection spectrum (a) and transmission spectrum (b) of a DBR consisting of 9.5 periods of Si_4N_4 and SiO_2. 8

Fig. 2.3. (a) Schematic view of a FP filter with two cavity modes, and (b) scheme of reflected and transmitted light in a FP filter. The figure is not in scale since the cavity is enlarged at the expense of the $\lambda/4$ layers [32]. 9

Fig. 2.4. Electric f eld of the fundamental mode in a FP f lter and the related refractive index prof le [33]. 10

Fig. 2.5. Transmittance of a FP filter with variable DBR mirror reflectivity. 11

Fig. 2.6. White Light Interferometer (WLI) measurements of a 3D NanoImprint template. A selection of filters is framed and magnified below together with the designed sink depths and the measured depths in brackets [22, 39]. 14

Fig. 2.7. Schematic fabrication process for FP filter / detector arrays: (a) defining bottom DBR on a detector array, (b) 3D NanoImprint template above soft cavity layer, (c) NanoImprint and curing of the polymer, (d) removal of template and deposition of the top DBR [22]. 15

Fig. 2.8. Schematic cross section of an 3D NanoImprinted FP filter array on top of a detector array and corresponding calculated transmission spectra [22, 39]. ... 16

Fig. 2.9. WLI characterization of an imprinted filter array with 64 different heights. The colors in the 3D diagram indicate the different heights. The surface roughness on each individual cavity (mesa) is approx. 0.6 nm rms [22, 39]. 17

Fig. 2.10. Tuning of an electrostatically actuated FP filter device: transmission line wavelength as a function of applied DC voltage. 19

Fig. 2.11. Tuning of FP filters: Wavelength of filter transmission line as a function of cavity height [32]. 20

Fig. 2.12. Scheme of an tunable FP filter array design: (a) top view of a single tunable filter, (b) top view of a filter array, (c) cross sectional view without (top) and with electrostatic tuning (bottom) [22]. 21

Fig. 2.13. SEM micrograph of a micromachined tunable FP filter [22]. 22

Fig. 2.14. Scheme of a one dimensional capacitor model. The initial cavity height when the applied voltage is zero is depicted as L [57]. 22

Fig. 2.15. Voltage of a movable plate capacitor as a function of displacement. The applied voltage reaches a maximum $\boldsymbol{Vpi}$ if the displacement is approximately $\boldsymbol{L3}$ one third of the initial air gap [58]. 24
Fig. 2.16. Simplified model of charge distribution after a DC voltage has been applied for a long time. The charging effect is studied in this specially designed FP filter geometry which is superior to study charging since the dielectrics are located in the center. This geometry will provide a situation where charging is revealed extremely. 26
Fig. 2.17. Scheme of a characterization setup. 29
Fig. 2.18. Spectral distribution of a Tungsten Halogen lamp [68]. 31
Fig. 2.19. Spectrum of the HAL lamps propagating through the compact microscope spectrometer setup. 31
Fig. 2.20. A comparison of spectra of a supercontinuum white light laser based on a Ti-Sapphire pump laser and different broad band sources [74]. 32
Fig. 2.21. Spectra of the supercontinuum laser based on a Nd-YAG laser as a pump laser which is used in chapter 6 [73].. 34
Fig. 2.22. Transmission spectra of a multiple thin film FP filter illuminated by different incident angles. 35
Fig. 2.23. (a) Individual diffraction patterns of two Airy disks (solid curves) and the resultant patterns (dashed curves). The Airy disks are far apart, and the patterns are well resolved. (b) The Airy disks are on the limit of resolution according to Rayleigh's criterion, the patterns are just resolved. (c) The Airy disks are so close together that their central spots overlap, thus the patterns are not resolved [93]. 37
Fig. 2.24. Optical ray traces of a microscope system corrected to infinity. 38
Fig. 2.25. Light part in Köhler illumination. The condenser creates a parallel beam. By adjusting the condenser diaphragm properly a well collimated beam which is perpendicular with respect to the filter layers is performed. 40
Fig. 2.26. Scheme of a grating monochromator consisting of a light source, an entrance slit, two concave mirrors, a diffraction grating and finally an exit slit. By rotating the diffraction grating relatively to the incident beam, the whole spectrum is scanned. 41
Fig. 2.27. Optical configuration of Double Path Monochromator which is equipped with a polarization scrambler, and a return reflection component. The return reflection component consists of two planar mirrors, two reflectors and an intermediate slit [99]. The direction of light propagation is illustrated as 1a – 1h. 44

Fig. 2.28. Experimental setup of the white light interferometry for measuring surface roughness and mechanical displacement of the static and tunable filter arrays, respectively. To investigate the tuning behavior of the tunable filter during actuation, two kinds of voltage supply, DC and AC, are implemented with the WLI. Two needles are connected to the top and bottom electrodes of the filter. 46
Fig. 3.1. Schematic setup of the Lambda 900 spectrophotometer [107]. 49
Fig. 3.2. Schematic diagram of the optical bench setup. 50
Fig. 3.3. Schematic diagram of the fiber based setup for reflection measurement [46]. 52
Fig. 3.4. Scheme of the experimental setup of the compact microscope spectrometer for the measurement of transmission and reflection spectra. 54
Fig. 3.5. Scheme of the setup for reflection measurement. 56
Fig. 3.6. Two needles for electrostatic actuation in the microscope spectrometer setup. 58
Fig. 3.7. Scheme of the sytem for transmission measurement. 60
Fig. 3.8. Ray paths in the compact microscope grating spectrometer setup. By properly adjusting the adjustable aperture diaphragm, only the light coming out from one filter located at position AB can be coupled into the fiber. The others are neglected. 61
Fig. 3.9. (a) Ray paths of the setup for calibration process, (b) defining the lateral dimension of the characterized filter, (c) localizing and framing the outgoing light in to that white square........ 63
Fig. 4.1. 3D side view of a tunable FP filter with ITO as bottom and top electrodes. ... 67
Fig. 4.2. Top view of several tunable FP filters with ITO as the top and bottom electrodes. 67
Fig. 4.3. 3D side view of a tunable FP filter with ITO as bottom electrode and Al as top electrodes. 67
Fig. 5.1. Experimental and simulated spectrum of a nonstructured FP filter: 9.5 periods of Si_3N_4/SiO_2 DBR, mr-UVcur 06 for $\boldsymbol{\lambda 2}$ cavity, central fabricated wavelength of 650 nm. 70
Fig. 5.2. Spectrum achieved from the compact microscope spectrometer and the Lambda 900 spectrophotometer when measuring the nonstructured FP filter. 71
Fig. 5.3. (a) Static filter structure from the side view, (b) topview, and (c) its corresponding spectra. The side view structure is taken from the WLI, the top view structure is taken from the compact microscope spectrometer setup...... 72
Fig. 5.4. Experimental and simulated spectra of a single FP filter in an array. 73
Fig. 5.5. Spectra from the compact microscope spectrometer and the optical bench setup. 74

Fig. 5.6. (a) 3D image of the characterized tunable filter TF1 and (b) its measured cavity height captured by WLI, (c) top view of a tunable FP filter with 4 straight suspensions and membrane radius of 12.5 µm, inspected area is 20 µm^2 (white square), (d) corresponding electrostatic actuation results of the tunable FP filter where the applied voltage is increased from 0 V to 25 V. 76
Fig. 5.7. Schematic diagram of the tunable FP filter TF1 and the Gaussian beam wavefront propagation. The filter is considered as a plano-concave resonator. When the confinement condition is satisfied, the radius of the membrane sphere is the same as the radius curvature of the beam wavefront. The air gap cavity length $\boldsymbol{L}$ must be equal or less than the radius of the curvature of the top membrane sphere $\boldsymbol{R2}$. 77
Fig. 5.8. (a) Top view of the tunable FP filter TF2 with 3 bent suspensions and membrane radius of 10 µm (diameter of 20 µm). (b) The inspected area is 15 µm x 15 µm (white square). (c) Corresponding electrostatic actuation results of tunable filters since the applied voltage is increased from 0 V to 21.8 V. 78
Fig. 5.9. (a) Schematic diagram of a tunable filter actuated by a DC voltage and (b) top view of the characterized tunable filter TF3 consisting of three bent suspensions, the radius of the membrane is of 15 µm, the inner diameter is of 10 µm. The filter has Al as top electrode and ITO as bottom electrode. 80
Fig. 5.10. Transmission spectra of the characterized tunable filter TF3 using DC actuation, the applied voltage is varying between 0 V to 12 V. 81
Fig. 5.11. Displacement of the membrane of the filter TF3 as a function of applied voltage using DC actuation. 81
Fig. 5.12. Block diagram of the electrical set-up for AC actuation. 84
Fig. 5.13. Transmission spectra of the tunable filter TF3 for an AC voltage frequency of 100 KHz is applied. This corresponds to an electrostatic force frequency of 200 kHz. 84
Fig. 5.14. (a) Transmission spectra and (b) mechanical displacement of the membrane using AC actuation for an AC voltage frequency of 500 KHz. This corresponds to an electrostatic force frequency of 1 MHz. 85
Fig. 5.15. (a) Transmission spectra and (b) mechanical displacement of the membrane using an AC voltage frequency of 1MHz. This corresponds to an electrostatic force frequency of 2 MHz. 86
Fig. 5.16. (left row: a,c,e) Comparison between AC actuation and (right row: b,d,f) DC actuation, (a) transmission spectrum for AC actuation, (b) transmission spectrum for DC actuation. (c) The enlarged images of transmission spectra for AC and (d) DC actuation at 0.15 V and 6 V, respectively. In each figure, the same colors denote the same applied voltage. This also holds for the red

color between (a) and (c) as well as for (b) and (d), respectively. (e) Mechanical displacement profiles and (f) for AC and DC actuation, respectively. 88
Fig. 5.17. A new model of dynamics of trapping and reemission of charges in dielectric layers of tunable FP filters in a metal/dielectric design. 92
Fig. 6.1. Schematic diagram of the free beam broad band confocal setup for transmission and reflection measurements. 99
Fig. 6.2. Scheme of the sample stage consisting of a xyz translation stage with sub-micron resolution and a rotation stage. 102
Fig. 6.3. Schematic diagram of the imaging system for visualizing the filter structure being measured. 103
Fig. 6.4. The final assembly of the free beam broad band confocal setup. The setup includes four main parts: the SCWLL as an illumination system, the collimation and magnification system, the imaging system and the sample stage. 105
Fig. 6.5. Side view (a) and top view (b) of the free beam broad band confocal setup. 105
Fig. 6.6. Spectra of the supercontinuum laser and corresponding spectra under different situations listed in the text. 107
Fig. 6.7. Topographies of a tunable FP filter. 108
Fig. 6.8. Matching the curvature of the filter membrane to the radius of the wavefront within the Gaussian beam assures that the light hits the filter perpendicularly. A curved filter has to be placed to the top or bottom of the beam waist. 109
Fig. 6.9. Transmission spectrum of an unstructured FP filter obtained from the free beam broad band confocal setup. 110
Fig. 6.10. (a) Top view of the static filter array SF3 indicating the four filters in the arrays characterized, (b) the corresponding spectra of the four characterized filters obtained from the free beam broad band confocal setup (full line) and the microscope spectrometer setup (dashed line). 111
Fig. 6.11. (a) Top view of the static filter array SF4 and four characterized filters in the arrays, (b) the corresponding spectra of four characterized filters obtained from the free beam broad band confocal setup. 112
Fig. 6.12. (a) Top view of the characterized tunable filter TF4, (b) the corresponding spectra of the filter obtained from the free beam broad band confocal setup (full line) and the compact microscope spectrometer setup (dashed line). 113

Table of abbreviations and chemical formula

1D	One dimension
3D	Three dimension
AC	Alternating current
Al	Aluminum
CCD	Charge coupled device
CMOS	Complementary metal oxide semiconductor
DC	Direct current
DBR	Distributed Bragg reflectors
$D_i(\lambda)$	Dark spectrum
$\mathcal{F}$	Finesse
FP	Fabry Pérot
FSR	Free spectral range
$FWHM$	Full width at half maximum
HAL	Halogen
ITO	Indium tin oxide
IR	Infrared
IBSD	Ion beam sputter deposition
INA	Institute of Nanostructure Technologies and Analytics
LED	Light emitting diode
$L(\lambda)$	Reference spectrum (spectrum of the lamp or the laser)
MEMS	Microelectromechanical system
NA	Numerical aperture
NIR	Near infrared
Nb_2O_5	Niobium oxide

OSA	Optical spectrum analyzer
PECVD	Plasma enhanced chemical vapor deposition
R	Reflectance
RIE	Reactive ion etching
$R(\lambda)$	Reflection spectrum
SCWLL	Supercontiuum white light laser
Si_3N_4	Silicon nitride
SiO_2	Silicon dioxide
$S_R(\lambda)$	Reflection spectrum from the sample
$S_T(\lambda)$	Transmission spectrum from the sample
TiO_2	Titanium oxide
TMM	Transfer matrix method
T	Transmittance
$T(\lambda)$	Transmission spectrum
UV	Ultraviolet
WLI	White light interferometry

Table of used symbols and physical parameters

λ	Wavelength
λ_0	Centre wavelength of a Distributed Bragg Reflector
$\Delta\lambda_0$	Bandwidth of a Distributed Bragg Reflector
$\Delta\varphi$	Phase shift
δ	Phase of a beam
d_i	Physical thickness of a layer of a Distributed Bragg Reflector
n	Reflective index
n_H	Refractive index of the high index layer
n_L	Refractive index of the low index layer
n_i	Refractive index of a corresponding material
n_s	Refractive index of the substrate
n_t	Refractive indices of the medium surrounding a Distributed Bragg Reflector
p	Number of layers in of a Distributed Bragg Reflector
$\Delta\lambda$	Width of a stopband
M	Number of different cavity heights
ζ	Damping coefficient
k	Spring constant
h	Displacement of the membrane
L	Initial cavity height of the air gap cavity
F_e	Electrostatic force
F_m	External forces
Q	Charge
C	Capacitance
V	Voltage

V_{DC}	DC Voltage
V_{pi}	Pull in voltage
z_{pi}	The maximum plate displacement at the pull in voltage
ω	AC frequency
ε	Permittivity
∂	Ratio defined the change of cavity height
w	Width of the suspension
t	Thickness of the suspension
ℓ	Length of the suspension
E	Young modulus
η	Optical tuning efficiency
α	Maximum angle under which the objective lens can gather the light
d	The smallest detectable distance between two adjacent points on a specimen
$\delta\lambda$	Wavelength resolution
$\Re$	Resolving power of a filter transmission line
N	Number of grating lines
x, y, z	Spatial coordinates
r	Radius of the membrane
q	Radius of the inner circle within a membrane
%	Percentage

List of Publications

1. **H.H. Mai**, A. Albrecht, C. Woidt, X. Wang, V. Daneker, O. Setyawati, T. Woit, K. Schultz, M. Bartels, H. Hillmer, 3D nanoimprinted Fabry–Pérot f lter arrays and methodologies for optical characterization, Applied Physics B, Volume 107, Issue 3, 2012, p. 755-764.
2. **H. H. Mai**, O. Setyawati, V. Daneker, C. Woidt, T. Woit, K. Schultz, S. Schudy, M. Engenhorst, X. Wang, S. Wittzack, F. Köhler, A. Albrecht, M. Bartels and H. Hillmer, "Verif cation and Calibration of Spectral Properties of High-resolution Nano Sensor Arrays Using Microscope Spectrometers", Technical Digest MOC´10, 16th Microoptics Conference 2010, Oct-Nov 2010, National Chiao Tung University and Microoptics Group, 2010, p. MC3(22-23).
3. C. Woidt, O. Setyawati, A. Albrecht, M. Engenhorst, V. Daneker, T. Woit, S. Wittzack, F. Köhler, **H.H. Mai**, M. Bartels, and H. Hillmer, "Micromachined Tunable Fabry–Pérot Filter Integrated into a Miniaturized Spectrometer for Low-Cost Applications", Inbook "Nanotechnological Basis for Advanced Sensors", Publisher: Springer-Dordrecht, Editor: J. P. Reithmaier, P. Paunovic, W. Kulisch, C. Popov and Plamen Petkov (Hrsg.), 2011, p. 537-541.
4. A. Albrecht, X. Wang, **H.H. Mai**, T. Schotzko, I. Memon, M. Bartels, M. Hornung, H. Hillmer, High vertical resolution 3D NanoImprint Technology and its application in optical nanosensors, Nonlinear Optics and Quantum Optics: Concepts in Modern Optics, Volume 43, 2012, p. 339-353.
5. A. Albrecht, **H.H. Mai**, V. Daneker, X. Wang, S. Schudy, T. Woit, K. Schultz, C. Woidt, O. Setyawati, F. Köhler, S. Wittzack, M. Engenhorst, M. Bartels and H. Hillmer, "Optical Characterization of High-Resolution Optical Nanospectrometers for Networked Sensing Systems", INSS Conference 2010, IEEE Technical Digest INSS, ISBN 978-1-4244-7910-8, 2010, p.175-178.
6. X. Wang, A. Albrecht, S. Schudy, T. Woit, V. Daneker, K. Schultz, **H.H. Mai**, F. Köhler, S. Wittzack, M. Bartels, H. Hillmer. High-resolution, Low-cost Microsensors for Networked Sensing Systems: Optical Nanospectrometers with

Nanoimprinted Cavities of Filter Arrays. IEEE Technical Digest INSS, ISBN 978-1-4244-7910-8., 2010, p. 171-174.

7. O. Setyawati, **H. H. Mai**, C. Woidt, S. Schudy, M. Engenhorst, S. Wittzack, F. Köhler, M. Bartels and H. Hillmer, “Low-Cost Micromachined Tunable Fabry-P´erot Filters for Optical Nano Sensor Arrays”, Technical Digest MOC´10, 16th Microoptics Conference 2010, Oct-Nov 2010, National Chiao Tung University and Microoptics Group, 2010, p. TB4(64-65).
8. X. Wang, A. Albrecht, T. Woit, M. Bartels, **H.H. Mai**, S. Schudy, V. Daneker, K. Schultz, F. Köhler, S. Wittzack, C. Sandhagen, W. Köcher, H. Hillmer. High Resolution 3D Nanoimprint Technology and its Application in Optical Sensors and Photonic Devices. Technical Digest of NNT '10, 2010.
9. X. Wang, M. Bartels, F. Köhler, S. Wittzack, A. Albrecht, **H.H. Mai**, T. Woit, S. Schudy, M. Engenhorst, C. Woidt, K. Schulz, H. Hillmer, High Vertical Resolution 3D Nanoimprint Templates, Technical Digest of NNT09, 2009.
10. M. Bartels, S. Wittzack, F. Köhler, X. Wang, A. Albrecht, S. Schudy, M. Engenhorst, H. H. Mai, O. Setyawati, T. Woit, C. Woidt and H. Hillmer, “High Vertical Resolution 3D Nanoimprint Technology for Nanophotonic Applications”, IEEE/LEOS International Conference on Optical MEMS and Nanophotonics 2009, 2009, p. 87-88.